UNIVERSITY OF CALIFORNIA
RIVERSIDE

The Relationship Between Lyman-Alpha Opacity of the Intergalactic Medium and Galaxy Density Near the End of Reionization

A Dissertation submitted in partial satisfaction
of the requirements for the degree of

Doctor of Philosophy

in

Physics

by

Holly Marie Christenson

June 2023

Dissertation Committee:

Dr. George Becker, Chairperson
Dr. Anson D'Aloisio
Dr. Gabriela Canalizo

The Dissertation of Holly Marie Christenson is approved:

Committee Chairperson

University of California, Riverside

Acknowledgments

I am grateful to my advisor, George Becker, for his support and guidance with this project. I would also like to thank the members of my committee, Anson D'Aloisio and Gabriela Canalizo. This project was supported by the National Science Foundation through grants DGE-1326120, AST-1615814, AST-1751404

The text of this dissertation, in part, is a reprint of the material as it appears in the Astrophysical Journal (December 2021). The text also contains a draft of an article that is currently being reviewed for publication in the Astrophysical Journal; the results of Chapter 3 are preliminary and the published version should take precedence over the work as presented and described here. The coauthors listed in those works contributed to it in the following manner: George Becker supervised and directed the research that forms the basis for both publications. Steve Furlanetto, Fred Davies, Anson D'Aloisio, and Fahad Nasir provided theoretical expertise and the model predictions to which I compare my observations. Yongda Zhu reduced and analyzed the quasar spectra used in this work. Elisa Boera assisted with the observations. Adam Trapp contributed analysis concerning the variance in LAE density between fields.

The research presented in this dissertation is based in part on data collected at Subaru Telescope, which is operated by the National Astronomical Observatory of Japan, and in part on data collected at the W.M. Keck Observatory. I would like to thank the staff at Keck and Subaru, who made the observations for this project possible. I also wish to recognize and acknowledge the very significant cultural role and reverence that the summit of Mauna Kea has always had within the indigenous Hawaiian community.

On a more personal note, I would like to thank Elisa Boera, Yongda Zhu, Azeem Bari, and Seyedazim Hashemi for their camaraderie and support with this project.

I would like to acknowledge my undergraduate research supervisors, Kristen Larson, Eric Gawiser, and Regina Jorgenson, without whose encouragement I would likely not have continued to pursue research. I am also grateful for the teachers and professors who supported me over the years, including Sr. Hance, Kevin Covey, and Regina Barber.

I am thankful to my DnD parties for all of the joy, the laughter, and the occasional exciting diversion from more serious pursuits. I am indebted to Kristy, Mary, and Karen for their love and care for Elsie.

I am deeply thankful to Graham for his patience and support. Special thanks go to Elise, who has chosen to be my friend for nearly two decades, through several degrees and over long distances. I would also like to thank my family, who have always steadfastly supported me in all of my endeavors. In particular I must thank my mother, who has fueled this dissertation with many of her excellent cookies.

And lastly, I thank my cats, Zoe and Mina, for their companionship, and for the many hours Mina has spent carefully supervising this project.

ABSTRACT OF THE DISSERTATION

The Relationship Between Lyman-Alpha Opacity of the Intergalactic Medium and Galaxy Density Near the End of Reionization

by

Holly Marie Christenson

Doctor of Philosophy, Graduate Program in Physics
University of California, Riverside, June 2023
Dr. George Becker, Chairperson

Cosmic reionization, the transition of the intergalactic medium (IGM) from neutral to ionized, was long believed to have concluded by $z = 6$. Recent quasar studies, however, have revealed a large scatter in the IGM Lyα opacity measured at $z < 6$ that cannot be explained by density fluctuations alone. There are several proposed explanations, including large-scale fluctuations in the ionizing ultraviolet background (UVB) or temperature of the IGM, or that reionization is still ongoing at $z < 6$. We note that while fluctuations in the temperature and UVB are expected as reionization ends, temperature fluctuations enhance the opacity of dense regions and reduce the opacity of underdense regions, while UVB fluctuations have the opposite effect. Models that predict this scatter therefore make strong predictions for how Lyα opacity is correlated to density. This work begins to characterize the relationship between IGM Lyα opacity and density, using Lyα emitting galaxies (LAEs) to probe density. We survey LAEs in the fields surrounding four quasar sightlines with extreme Lyα opacity: two highly opaque sightlines, which display long Lyα troughs, and two highly transmissive sightlines. We find that all four fields are underdense in LAEs within 10 h^{-1} Mpc of the

quasar sightline, and that the opaque fields are underdense to a larger lateral extent ($\gtrsim$ 20 h^{-1} Mpc). The high-opacity sightlines strongly disfavor temperature models, but are consistent with the other models. There is tension between the UVB and late reionization models and the low-opacity sightlines, however, as the models associate low opacity with high density. We further consider three recently observed fields from the literature, and find that there is scatter in the density associated with moderate opacities that is not well-predicted by the models. Altogether, these observations are not clearly consistent with any of the models we consider. The observed association between low opacity and low density regions may suggest that the ionizing background in low density regions increases rapidly after they have been reionized. If these results are supported by future observations, it would suggest that current reionization models do not fully capture the physical conditions leading to extreme opacity.

Contents

List of Figures

List of Tables

Chapter 1

Introduction

1.1 Background

Most of the matter in the universe is hydrogen gas, and most of that hydrogen gas makes up a diffuse gaseous medium found between galaxies, known as the intergalactic medium (IGM). In the modern day universe, the intergalactic medium is maintained in a highly ionized state by a steady output of ultraviolet photons from stars and accreting black holes, and it is therefore highly transparent to ionizing photons. The IGM wasn't always transparent, however. The early universe was made up of a hot, dense plasma. As the universe expanded and cooled adiabatically, the free protons, neutrons, and electrons combined to make the first atoms, most of which were hydrogen. These newly formed atoms were electrically neutral, and the universe became opaque.

As the first stars and galaxies began to form, they released ionizing radiation into their surroundings, reionizing the intergalactic medium. This transition of the IGM from neutral to ionized, referred to as reionization, was the last major phase transition in

the universe's history. Reionization is believed to have proceeded in a patchy manner, as ionizing sources were able to ionize only small bubbles around themselves. As more ionizing sources formed and more ionizing photons were released into the IGM, these bubbles began to expand and overlap until the IGM was fully ionized.

Reionization is of interest for several reasons. The first is that it is a major phase of the universe's history that is not yet well understood. Further, our observations of high-redshift objects rely on light that passes through the high-redshift IGM, and understanding how this medium interacts with the light passing through it is an important context for those observations. Lastly, reionization serves as a test for our models of galaxy formation. These models must produce a galaxy population that is capable of producing the reionization history that we observe.

There are two main open questions concerning reionization that current research is attempting to address. The first is what type of source is the largest contributor of ionizing photons. Quasars are luminous and therefore have a large ionizing photon output, but are relatively rare. Faint galaxies produce fewer ionizing photons, but are much more numerous. The general consensus is that faint galaxies are most likely to be the main contributors, although because they are difficult if not impossible to observe at high redshifts, direct evidence for this conclusion is limited to studying nearby faint galaxies as analogues.

The second open question concerns when reionization took place. Reionization has long been believed to have ended by $z = 6$ based on observed transmission in quasar spectra, and current studies - including the presence of damping wings in $z > 7$ quasar spectra, estimates of the IGM neutral fraction from galaxy surveys, and measurements of the cosmic

microwave background - suggest that much of reionization took place over $6 < z < 8$. A midpoint of reionization at $z \sim 7 - 8$ is difficult to reconcile with an endpoint at $z = 6$, however, as ionizing sources would have to be extremely efficient to complete reionization so rapidly. Recent work has suggested that the epoch of reionization may extend to redshifts as low as $z = 5.3$, and exploring that possibility is a main focus of this work.

1.2 The Lyα Line

Most probes of reionization rely on the Lyman alpha (Lyα) line, the $n = 2$ to $n = 1$ electronic transition in hydrogen. In the IGM, Lyα is absorbed when a photon with energy matching the energy difference between these two states encounters a neutral hydrogen atom in the ground state. It is typically emitted when a hydrogen ion collides with a free electron, which may land in any of the excited states or in the ground state. If the electron is in the ground state, the hydrogen atom emits a highly energetic photon, but if it ends up in a higher excited state, it may cascade through intermediate excited states and eventually produce a Lyα photon as it transitions from the first excited state to the ground state. This process of ionized hydrogen colliding with a free electron is called recombination. The rate at which recombinations occur is set by the gas density and temperature, which determine the probability that an ionized hydrogen atom will collide with a free electron; the gas density sets the population of free electrons available to combine with, and the temperature determines their speed. Particles that are moving more quickly are less likely to collide.

1.2.1 Lyα in Emission

Lyman alpha emission is often associated with star formation. Young galaxies that are forming typically go through a "starburst" phase, during which they have extremely high rates of star formation. Neutral hydrogen gas, a key ingredient for star formation, can be ionized by O and B type stars, which live short lives but emit strongly in the ultraviolet. The gas surrounding these stars then re-emits Lyα photons via recombination radiation. As these Lyα photons travel through the galaxy's interstellar medium (ISM), they are repeatedly absorbed as they encounter neutral hydrogen atoms and then re-emitted in random directions, which is called resonant scattering. Photons "random walk" by scattering around the ISM until they may eventually escape the galaxy. Some galaxies are very bright in Lyα and these are called Lyman alpha emitters (LAEs).

Observing Lyα in emission during the epoch of reionization is uniquely challenging because the cross section for a Lyα photon being absorbed by neutral hydrogen is very high. That also means that observations made using Lyα are a rich source of information about the epoch of reionization, because the properties of Lyα at these redshifts are affected by the intervening IGM.

The profile of a Lyα emission line measured from a galaxy is a useful source of information about the surrounding medium. An emission line coming from gas with a random velocity distribution will generally have a Gaussian profile. When a Lyα line is emitted from a galaxy and encounters neutral gas - for example, within the galaxy's star-forming regions - it is absorbed and then re-emitted at resonance. The resulting random walk in frequency creates a double-peaked line profile. This absorption occurs in the interstellar

medium; the double-peaked profile is considered the intrinsic line profile emitted by the galaxy. The blue side peak of this profile is typically then absorbed by intervening neutral gas in the IGM and CGM. A galaxy that shows a detectable blue peak in the Lyα spectrum must sit in an ionized region that is large enough for the blue peak to redshift out of resonance before it is absorbed.

LAE populations are also a useful probe of reionization, in part because they can be selected robustly and relatively inexpensively using photometric surveys. There are two approaches to using LAEs to study reionization. The first takes advantage of the fact that the Lyα line tends to be absorbed in a neutral medium to characterize the fraction of hydrogen in the IGM that is neutral, which cannot be measured directly. It can be measured indirectly, however, because the fraction of galaxies selected on their UV continuum emission that display a measurable Lyα line will tend to be lower at redshifts where there is more neutral hydrogen, all other properties of the Lyα emission lines being equal.

The second approach takes advantage of the fact that a Lyα emission line can place galaxies in redshift space relatively precisely. LAEs are normally selected photometrically, making use of at least two filters: a broadband filter, and a narrowband filter that sits within the broadband filter range. Other bands may also be used to rule out lower-redshift objects, but the main identifying feature of LAEs is that they have a measurable excess of flux in the narrowband filter relative to the broadband filter. This excess indicates the presence of an emission line, which is washed out in the broadband filter but dominates in the narrowband filter. The wavelength coverage of the narrowband filter therefore constrains the LAE to a fairly small redshift window. Further, the presence of an emission line largely alleviate

the need for traditional methods of estimating photometric redshifts, which are challenging. While spectroscopic followup yields more precise redshifts, photometric redshifts are adequate for correlating LAEs in redshift space. Therefore, LAEs are useful for searching for signs of structure, such as overdensities that may indicate protoclusters, for measuring Lyα luminosity functions, and for characterizing LAE clustering.

This work makes use of the Lyα line to correlate observed LAE populations spatially to interesting features observed in quasar spectra, which brings us to the study of Lyα in absorption.

1.2.2 Lyα in Absorption

Neutral atoms in the IGM produce what's known as the Lyman alpha forest, a series of absorption features along the spectrum of a background ionizing source where Lyα has been absorbed. The Lyα forest and other features associated with the spectra of background quasars can be used to measure the properties of the IGM. For example, the onset of transmission in quasar sightlines at $z \sim 6$ suggests that the IGM is largely ionized at those redshifts because even a tiny neutral fraction ($\sim 10^{-3}$) is enough to produce nearly complete absorption in the Lyα forest. For this reason, reionization was long assumed to have ended by $z = 6$.

The width of absorption features in the Lyα forest is sensitive to the properties of the absorbing IGM. There are two main broadening mechanisms: thermal broadening and Hubble broadening. Thermal broadening is caused by the random motions of individual absorbing particles. Hubble broadening is caused by the bulk motion of the gas as the universe expands. The time that elapses while light from a quasar passes through an absorbing

structure is sufficiently large that the universe expands appreciably, which causes an amount of broadening that depends on the expansion rate and the size of the absorbing structure. This broadening can be enhanced by energy injected into the IGM by ionizing sources during and after reionization, which tends promote expansion of absorbing structures. This expansion is referred to as Jeans smoothing. The peculiar velocity of an absorbing structure can also contribute to line broadening. Characterizing the distribution of the scale of IGM Lyα absorption features features - or, measuring the Lyα forest flux power spectrum - can be used to constrain the thermal history of the IGM, which in turn can be used to constrain the reionization history. The most recent studies in this area suggest that the midpoint of reionization is $z \sim 8$.

Characteristics of individual absorption features are also informative. If there are large quantities of neutral gas, an absorption feature may show Lorentzian "wings" of extended absorption far from resonance because even though the Lyα cross section is small for wavelengths far from resonance, absorption will still happen at a measurable rate when there are large enough numbers of neutral hydrogen atoms present. Damping wings have been observed in the spectra of quasars at $z > 7$, which indicates that the IGM is still substantially neutral at those redshifts.

The Lyα line is highly sensitive to neutral hydrogen gas; even a tiny neutral fraction ($\sim 10^{-3}$) is sufficient to absorb Lyα photons. The presence of opaque regions may be quantified over significant segments of a spectrum, or down to every individual "dark" pixel. Quantifying dark gaps and pixels in a quasar spectrum is therefore another way to set limits on the neutral fraction of hydrogen in the IGM.

The measurement most relevant to this work is the effective opacity, which is given by $\tau_{\rm eff} = -\ln\langle \mathrm{F} \rangle$, where F is the continuum-normalized flux measured over a chosen segment of a spectrum. We make use of effective opacity measurements to identify quasars with particularly opaque and transmissive regions in their spectra on significantly large ($\gtrsim 50$ h^{-1} comoving Mpc) length scales.

The most notable absorption features observed on large length scales are called Lyα troughs. These large-scale absorption features correspond to complete absorption of Lyα photons on scales of tens of comoving Mpc. These features are produced in regions where reionization is incomplete and there is neutral hydrogen which completely absorbs Lyα photons. They are unexpected at $z < 6$ because the presence of Lyα transmission in most quasar spectra suggests that the IGM must generally be highly ionized at these redshifts. However, a key result of recent reionization studies is that such features do exist in $z < 6$ quasar spectra, if only rarely. The largest of these troughs is 110 h^{-1} Mpc in scale, and it is as yet unclear why such large troughs exist in the $z < 6$ IGM. It is possible that Lyα troughs may also arise from highly ionized regions that still harbor enough neutral atoms to produce complete absorption, as a neutral fraction of only $\sim 10^{-3}$ is sufficient.

1.3 This Work

Together, the observations previously discussed point to a late, fast reionization scenario that largely occurred between $z = 6 - 8$. Reionization was long assumed to end by $z = 6$, but recent models suggest that it may have ended as late as $z \sim 5.3$, a possibility that is consistent with observations. Reionization models are challenging to develop because

they need to match constraints on the neutral fraction and UVB; this is an area of ongoing modeling work. Constraining the plausibility of the models via observations is of great interest, and even data that disagree with the models are a useful source of insight into what the models do not capture well and how they can be improved.

In this work, we attempt to ascertain the nature of the large Lyα troughs produced by the $z < 6$ IGM and understand what physical conditions lead to the large observed scatter in Lyα opacity at these redshifts. We combine two types of observations of the Lyα line - $\tau_{\rm eff}$ measurements to select quasar sightlines of extremely high and low opacity, and Lyα in emission to survey galaxies in the surrounding fields. The correlation between galaxy density and opacity is predicted by different types of reionization models, and so surveying LAEs in these fields serves as a test of those models. More importantly, the relationship between opacity and density at these redshifts provides insight into the physical conditions of the IGM at the end of reionization.

1.3.1 Tools and Methods for LAE selection

The selection of LAEs in the fields surrounding quasar sightlines makes up the basis for this work. LAEs, as previously noted, are selected using photometric surveys. In this work, we make use of Subaru/Hyper Suprime Cam (HSC) to conduct these surveys. HSC has a very large field of view (1.5 degrees in diameter), which is key to the measurements we make in this work. We are interested in how galaxy density correlates to IGM Lyα opacity. To measure the density, we make a differential measurement by self-consistently comparing the innermost region of the field, in the vicinity of the quasar sightline, to the remainder of the field. This differential measurement is robust to systematic effects, such as incompleteness in

the galaxy catalog and contamination of lower-redshift sources. Contaminants are uniformly distributed across the field, and therefore don't introduce significant bias to a differential measurement.

The imaging data are processed using the data reduction pipeline that is in development for the Vera Rubin Observatory Legacy Survey of Space and Time (LSST). The pipeline is publicly available, has packages developed specifically to handle HSC data, and is designed to handle large volumes of data efficiently. We use the LSST pipeline for most of the major steps of the data reduction process, including processing calibration images (bias, flat, and dark frames), processing individual image frames, and combining the single frames into a stacked mosaic. The pipeline is also capable of different modes of photometry using these stacked images, but in this work we have opted to use a custom Python pipeline to make photometric measurements.

Before making photometric measurements, we use Source Extractor to identify source positions in the final images. Source Extractor is a versatile software tool designed to quickly and efficiently produce highly customizable catalogs of sources with a variety of options for photometric measurements, primarily intended for galaxy surveys. In this work, we use Source Extractor to identify source positions only, and then make our own measurements at those source positions.

The photometric pipeline used in this work has, in various iterations, included different types of measurements (described in more detail in Section 2.4 and 3.4), but the basic procedure has always included reading in the list of source positions, reading in a small portion of the image surrounding each source from which to make measurements, and then

compiling a catalog of all the measurements for each object. We have in various stages of this work used two different types of photometry: aperture photometry and point spread function (PSF) photometry. Aperture photometry represents a simple sum of all the flux that lies within a circular aperture of a given size, usually $1.5 - 2''$. It yields a lower signal-to-noise than other flux measurements because the pixels are unweighted, but requires no assumptions about the profile of the source. PSF photometry, on the other hand, requires knowledge of the intrinsic profile of the source. Flux measurements are made by fitting that profile to the source. For ground-based imaging of high-redshift objects, that typically means assuming that the object is a point source and its extent in the imaging is determined by atmospheric seeing. There are other approaches to characterizing the morphology of resolved sources, but we did not make use of them in this work. PSF photometry effectively weights the pixels based on the assumed profile and therefore results in higher signal-to-noise than a comparable aperture flux, but is more easily biased if the assumed profile is incorrect. For both aperture and PSF measurements, we made "forced" measurements, which refers to using the narrowband filter as the image for identifying the position of the source, and then holding that position fixed for photometric measurements in all bands. This mode of photometry is sensible for selecting LAEs, as they may be detected only in the narrowband. We then use our photometric measurements to select LAEs based on their flux excess in the narrowband, as well as a few additional quality control criteria. We also visually inspect each candidate - a step that is necessary because spurious objects such as satellite trails could be falsely selected as LAEs based on their photometry alone.

1.4 Summary

In this work, we combine two types of observations of the Lyα line: we survey Lyα emitters in the vicinity of quasar sightlines with extremely high or low effective Lyα opacity over long length scales in their spectra, taking advantage of the emission line nature of LAEs to correlate the two in redshift space. The correlation between galaxy density and IGM Lyα opacity is determined by the physical conditions of the IGM, and characterizing this relationship provides insight into how and when reionization ended. Chapter 2 summarizes our first observations of two highly opaque sightlines. Chapter 3 adds two highly transmissive sightlines, alongside a re-analysis of the opaque sightlines using updated photometry. Chapter 4 summarizes the progress made in this work, the challenges it faces, and what implications our results have for future reionization studies.

Chapter 2

Constraints on the End of Reionization from the Density Fields Surrounding Two Highly Opaque Quasar Sightlines

2.1 Abstract

The observed large-scale scatter in Lyα opacity of the intergalactic medium at $z < 6$ implies large fluctuations in the neutral hydrogen fraction that are unexpected long after reionization has ended. A number of models have emerged to explain these fluctuations that make testable predictions for the relationship between Lyα opacity and density. We present selections of $z = 5.7$ Lyα-emitting galaxies (LAEs) in the fields surrounding two highly

opaque quasar sightlines with long Lyα troughs. The fields lie towards the $z = 6.0$ quasar ULAS J0148+0600, for which we re-analyze previously published results using improved photometric selection, and towards the $z = 6.15$ quasar SDSS J1250+3130, for which results are presented here for the first time. In both fields, we report a deficit of LAEs within 20 h^{-1} Mpc of the quasar. The association of highly opaque sightlines with galaxy underdensities in these two fields is consistent with models in which the scatter in Lyα opacity is driven by large-scale fluctuations in the ionizing UV background, or by an ultra-late reionization that has not yet concluded at $z = 5.7$.

2.2 Introduction

Cosmic reionization was the last major phase transition in the history of the universe, during which radiation from the first luminous sources ionized neutral hydrogen in the intergalactic medium (IGM) and transitioned the universe from a mostly neutral to a highly ionized state (see Wise 2019 for a review). The physical properties of the IGM at reionization redshifts can be used to constrain the timing, duration, and sources of reionization, which have major implications on our understanding of the first luminous sources in the universe and their environments.

A number of observations now suggest that much of the IGM was reionized from $z \sim 6 - 8$. Measurements of the cosmic microwave background (CMB) are consistent with an instantaneous reionization occurring at $z \sim 7.7 \pm 0.7$ (Planck Collaboration et al., 2020). Evolution in the fraction of UV-selected galaxies that show Lyα in emission suggests that significant portions of the universe remain neutral at $z \sim 7 - 8$ (Mason et al., 2018; Jung

et al., 2020; Morales et al., 2021, and references therein). The presence of damping wings in $z \geq 7$ quasar spectra (Mortlock et al., 2011; Greig et al., 2017; Bañados et al., 2018; Davies et al., 2018b; Greig et al., 2019; Wang et al., 2020) also suggest a largely neutral IGM at those redshifts. Meanwhile, the onset of Lyα transmission in quasar spectra suggests that reionization was largely complete by $z \sim 6$ (Fan et al., 2006; McGreer et al., 2011, 2015).

Recent studies, however, have suggested that signs of reionization may persist in the IGM considerably later than $z = 6$. Measurements of the Lyα forest towards high-redshift QSOs show a large scatter in the opacity of the IGM to Lyα photons at redshifts ≤ 6.0 (Fan et al., 2006; Becker et al., 2015; Bosman et al., 2018; Eilers et al., 2018; Yang et al., 2020; Bosman et al., 2021), which is unexpected long after reionization has ended. The observed scatter on 50 comoving h^{-1} Mpc scales has been shown to be inconsistent with simple models of the IGM that use a uniform ultraviolet background (Becker et al., 2015; Bosman et al., 2018; Eilers et al., 2018; Yang et al., 2020; Bosman et al., 2021) . The most striking example of this scatter is the large Gunn-Peterson trough associated with the $z = 6.0$ quasar ULAS J0148+0600 (hereafter J0148), which spans 110 h^{-1} Mpc and is centered at $z = 5.7$ (Becker et al., 2015). While some scatter in Lyα opacity is expected due to variations in the density field (e.g., Lidz et al., 2006), the extreme opacity in the J0148 field cannot be explained by variations in the density field alone. Several types of models have therefore emerged to explain the observed scatter as due to variations in the IGM temperature and/or ionizing background, or potentially the presence of large neutral islands persisting below redshift six.

One type of model is based on a fluctuating ultraviolet background (UVB), in

which large-scale fluctuations in the photoionizing background drive the large-scale fluctuations in Lyα opacity. Galaxy-driven UVB models, in which the fluctuations in the ionizing background result from clustered sources and a short, spatially variable mean free path, have been considered by Davies & Furlanetto (2016), D'Aloisio et al. (2018), and Nasir & D'Aloisio (2020). In this scenario, highly opaque regions are associated with low-density voids that contain few sources and therefore have a suppressed ionizing background. Low-opacity regions, in contrast, would have a strong ionizing background from its association with an overdensity of galaxies. Alternatively, Chardin et al. (2015, 2017) proposed a model in which the ionizing background is dominated by rare, bright sources such as quasars, which naturally produces spatial fluctuations in the UVB. Because quasars are rare, bright sources, the resulting UVB is not tightly coupled to the density field. In this scenario, a trough is associated with a suppressed ionizing background due to a lack of nearby quasars. The quasar-driven model, however, is somewhat disfavored because the required number density of quasars is at the upper limit of observational constraints and may also be in conflict with observational constraints on helium reionization (D'Aloisio et al., 2017; McGreer et al., 2018; Garaldi et al., 2019).

D'Aloisio et al. (2015) proposed a model in which the opacity fluctuations are driven by large spatial variations in temperature, leftover from a patchy reionization process. In this scenario, overdense regions were among the first to reionize, and therefore have had more time to cool than less dense, more recently reionized regions. Absorption troughs such as the one towards J0148 are associated with overdense regions in this scenario; conversely, highly transmissive regions would be underdense.

More recently, a new type of model has emerged that suggests reionization may have ended later than $z \sim 6$, as widely assumed (Kulkarni et al., 2019a; Keating et al., 2020a,b; Nasir & D'Aloisio, 2020; Choudhury et al., 2021; Qin et al., 2021). In this scenario, the observed scatter in Lyα opacity is driven at least partly by islands of neutral hydrogen remaining in the IGM past $z = 6$. Troughs like the one associated with J0148 therefore trace regions of the IGM that have not yet been reionized. The last places to become ionized in this model are low density, but those same underdense regions may quickly become highly transmissive once they have been reionized (Keating et al., 2020b). These models predict that both high- and low-opacity sightlines may be underdense (although see Nasir & D'Aloisio (2020), who find a large range in densities for transmissive lines of sight). We note that ultra-late reionization models typically also include a fluctuating UVB, but their defining feature is the presence of neutral islands at $z < 6$.

A key result of the attempts to model large-scale fluctuations in Lyα opacity is that each type of model makes strong predictions for the relationship between opacity and density, particularly for extremely high and low opacities. Both of these quantities can readily be measured; the opacity of a sightline can be obtained from a background quasar's Lyα forest, and a galaxy survey can be used to trace the underlying density. Davies et al. (2018a) demonstrated that surveys of Lyman alpha emitters (LAEs) should be able to distinguish between these models for extremely high- and low-opacity sightlines. LAEs are a good choice for this type of observation because LAE surveys at $z \sim 6$ can be conducted with only three bands of photometry. Narrow-band filters tuned to the atmospheric window near 8200 Å, corresponding to Lyα at $z = 5.7$, are also well matched to a redshift where large opacity

fluctuations are present.

The results of a LAE survey in the J0148 field were published in Becker et al. (2018). These results were consistent with fluctuating UVB and late reionization models, and strongly disfavored the fluctuating temperature model. Kashino et al. (2020) followed up with a selection of Lyman break galaxies in the same field as a separate probe of density, and also reported a strong underdensity associated with the trough.

In this paper, we extend the study of the Lyα opacity-density relation to a second field surrounding a highly opaque quasar sightline. We provide an updated selection of LAEs towards ULAS J0148+0600, and present new results for SDSS J1250+3130, whose spectrum exhibits an 81 comoving h^{-1} Mpc Lyα trough. The LAE selections are based on updated LAE selection criteria, which we verify with spectroscopic followup of J0148 LAEs with Keck/DEIMOS. We summarize the observations in Section 2.3, and describe the photometry and LAE selection criteria in Section 2.4. The accompanying spectroscopy is presented in Appendix B. We present the results of LAE selections in both fields in Section 2.5, and compare the results to current reionization models in Section 2.6 before summarizing in Section 2.7. Throughout this work, we assume a ΛCDM cosmology with $\Omega_m = 0.3$, $\Omega_\Lambda = 0.7$, and $\Omega_b = 0.048$. All distances are given in comoving units, and all magnitudes are in the AB system.

2.3 Observations

Imaging data taken with Subaru Hyper Suprime Cam (HSC) were previously presented for the ULAS J0148+0600 field by Becker et al. (2018). The spectrum of ULAS

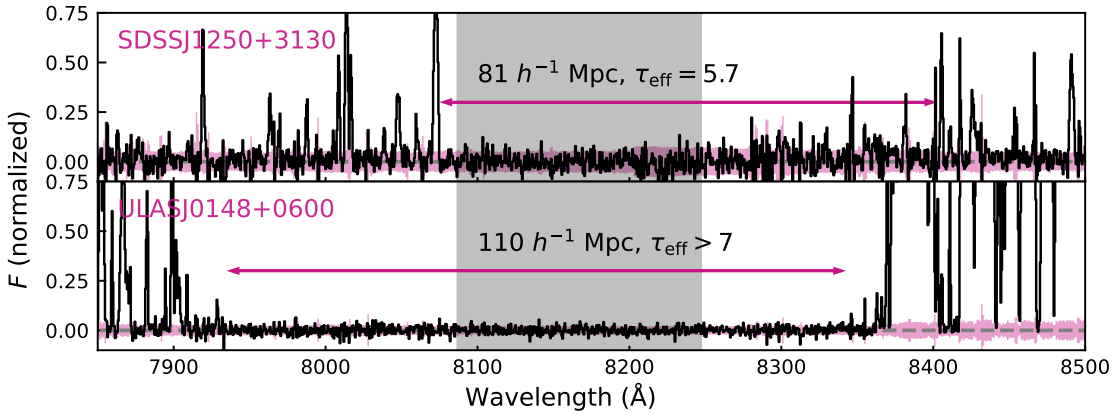

Figure 2.1 Partial spectra of the two quasars whose fields we observe with Subaru/HSC. The top panel shows a Keck/ESI spectrum of SDSS J1250+3130, which exhibits a Lyα trough that is 81 h^{-1} Mpc in length with $\tau_{\rm eff} = 5.7 \pm 0.4$ (Zhu et al., 2021). The bottom panel shows an X-Shooter spectrum of ULAS J0148+0600, which exhibits a 110 h^{-1} Mpc Lyα trough with $\tau_{\rm eff} \geq 7$ (Becker et al., 2015). The approximate extent of each trough is indicated by the pink arrows. These quasars represent some of the most extreme Lyα troughs known at $z < 6$. The shaded gray region shows wavelengths covered by the NB816 filter with at least 10% transmittance, which corresponds to Lyα at $z \simeq 5.7$. The shaded pink region indicates the $\pm 1\sigma$ uncertainty interval.

J0148+0600 contains a 110 h^{-1} Mpc trough that has effective optical depth of $\tau_{\rm eff} \geq 7$, where $\tau_{\rm eff} = -\ln\langle F \rangle$ and F is the mean continuum-normalized flux. For this work, we obtained HSC imaging of a second field, towards the $z = 6.15$ quasar SDSS J1250+3130 (hereafter J1250). The Lyα forest in the spectrum of J1250 contains a trough spanning 81 h^{-1} Mpc with $\tau_{\rm eff} = 5.7 \pm 0.4$ (Zhu et al., 2021). The J1250 and J0148 fields represent some of the most highly opaque sightlines known at these redshifts. Figure 2.1 shows subsets of the X-Shooter spectrum for ULAS J0148+0600 (Becker et al., 2015) and the Keck/ESI spectrum for SDSS J1250+3130, displaying their Lyα troughs.

The J1250 field was observed via the HSC queue in April and June 2019, with

Table 2.1 Summary of HSC imaging

	Filter	t_{exp} (hrs)	Seeing[b]	$m^c_{5\sigma,PSF}$	$m^c_{5\sigma,1.5''}$
J0148	$r2$	1.5	0.76	26.4	26.0
	$i2$	2.4	0.80	26.0	25.6
	$NB816$	4.5	0.73	25.2	25.0
J1250	$r2$	2.0[a]	0.83	26.4	26.2
	$i2$	2.5	0.81	26.1	25.8
	$NB816$	2.8	0.74	25.3	25.0

[a] Partially observed in gray time.
[b] Median seeing FWHM in combined mosaic.
[c] Magnitude at which 50% of detected sources have $S/N \geq 5$.

the majority of the data being taken during dark time in April. Additional observations were taken during dark time in May 2020 and January 2021. As for the J0148 field, we obtained imaging centered on the quasar position in the NB816 filter, which has a mean transmission-averaged wavelength $\lambda = 8177$ Å, corresponding to Lyα emission at $z = 5.728$, and two broadband filters, $i2$ and $r2$. The narrowband observations were completed as planned, but the initial $r2$ observations in the J1250 field were completed in gray time and supplemented by additional dark time observations in May 2020. We summarize the observations in both fields in Table 2.3.

We reduced the raw data with the LSST Science Pipeline, Versions 19 (J0148 field) and 22 (J1250 field) (Ivezić et al., 2008; Jurić et al., 2015). The pipeline combines individual CCDs into stacked mosaics, using PanStarrs DR1 imaging (Chambers et al., 2016) for astrometric and photometric calibrations. We use Source Extractor (Bertin & Arnouts, 1996) to identify the spatial coordinates of sources in the final stacked mosaics, and then make photometric measurements at those positions based on PSF fitting, which we describe in more detail in Section 2.4.

Table 2.3 shows the median 5σ limiting PSF and aperture magnitudes in each band

for both fields. These values represent the magnitudes at which at least 50% of the detected sources are measured at signal-to-noise ratios $S/N \geq 5$.

We also use the imaging data to independently measure the Lyα opacity over the $NB816$ wavelengths for each quasar line of sight. The results are presented in Appendix A.

2.4 Methods

In this section we describe in detail the methods used to make photometric measurements and select LAE candidates.

2.4.1 Photometry

Becker et al. (2018) used CModel fluxes generated by the LSST pipeline, which are a composite of the best-fit exponential and de Vaucouleurs profiles (Abazajian et al., 2004; Bosch et al., 2018). We verified the quality of the flux calibration by checking the fluxes of 25 objects in each field from the SDSS catalogs. While the flux measurements for the verification objects were accurate to within the photometric errors, fluxes for faint, typically seeing-limited objects were found to be less reliable. For some of these objects, the best-fit CModel profile resulted in conspicuously high fluxes that were not in agreement with the fixed-aperture and PSF fluxes. This systematic overestimation of CModel fluxes compromised the initial selection of LAEs in the J0148 field in two ways: objects that are not credible LAEs were selected as LAEs based on artificially high narrowband flux, and objects that could be credible LAEs were rejected based on artificially high broadband fluxes that resulted in failure of one or more color criteria. Examples of both types are shown in

Appendix C.

To address these problems with the CModel fluxes, we implemented PSF measurements to replace the CModel measurements as the primary flux used in the analysis. The PSF photometry is optimized to maximize the detection of faint, often unresolved sources for the purposes of constructing a density map. Sources whose profiles are not well-represented by a PSF profile, such as extended sources, are assigned an aperture flux as their primary flux measurement, which we describe in more detail below.

The photometry has the following steps:

1. At each source position identified and measured by Source Extractor in the combined mosaics, we measure the flux in a $1.5''$ aperture.

2. We then measure the median sky background measured in a $5''$ annulus around the aperture, excluding any pixels that are flagged by the data reduction pipeline as sources.

3. A 2-dimensional Gaussian profile is fit over a stamp of the combined mosaic $10 \times 10''$ in size centered on the source, using the measured sky background as the offset and holding the FWHM fixed to the median seeing. The only parameter allowed to vary is the amplitude.

4. Each pixel in the stamp is compared to the resulting fit. Pixels that differ from the model by more than five times the noise in the sky background are excluded from the next iteration of fitting. The primary purpose of this step is to reject cosmic rays and bad pixels.

5. The 2D Gaussian is fit again, excluding outlier pixels. After re-fitting, all pixels are again compared to the model and the exclusion and re-fitting process is repeated. Pixels that were previously rejected may be included in the next iteration of the fit. If the fitting exceeds ten iterations, more than 5% of pixels in the stamp are rejected, or more than 5% of the pixels within a 1.5″ aperture are rejected, the fit is considered a failure and the aperture flux is used as the primary flux measurement for that object. Typically, extended sources and other objects whose profiles are not well represented by the PSF profile will therefore be assigned aperture fluxes. If re-fitting fails to improve the fit (the same set of pixels are selected for exclusion in two subsequent iterations) but the maximum number of iterations and excluded pixels are not exceeded, the fit is considered a success and the resulting PSF flux is recorded. Approximately 20% of all sources fail, and 50% are refit at least once, most undergoing two iterations.

This PSF measurement is conducted for each band, independently of the others. We have allowed the fitting routine to default to aperture fluxes because for many credible LAEs, the $r2$ and $i2$ fluxes are formally undetected, and the results of fitting a Gaussian to a field dominated by noise may be unpredictable. In these cases, we default to the aperture flux rather than accept a potentially bad fit.

2.4.2 LAE Selection Procedure

In addition to improving our photometric measurements, we have adjusted the criteria we use for selecting LAE candidates. Our observations in the J1250 field were made over the course of three years, and the partially complete observations had large variations

in depth across the three bands. This disparity motivated an adjustment of the selection criteria to account for the depth in each band. Our completed observations are still slightly uneven in depth across the three filters, and there are variations in depth between fields - for example, the J1250 field is slightly deeper than the J0148 field in both broadband filters. The revised selection criteria described do not dramatically change the LAE selection in these two fields; however, they reduce the number of selected objects by $\sim 25\%$. We emphasize that all sources must still pass a visual inspection to be accepted as LAE candidates.

The criteria originally used to select LAEs in the J0148 field were based on those used in (Ouchi et al., 2008): $NB816 \leq 26.0$, $S/N_{NB816} \geq 5$, $i2 - NB816 \geq 1.2$, and $r2 \leq 2\sigma_{r2}$ or $r2 \geq 2\sigma_{r2}$ and $r2 - i2 \geq 1.0$. These requirements are designed to select line emitters and rule out low-redshift objects, but have no requirement for uncertainty or S/N in any band except the narrow band.

In order to account for the different depths of our photometric bands, we re-express the selection criteria in terms of probability densities. For each color cut, we require that at least 50% of the probability density for that color is above the minimum acceptable color. We also require that 95% of the probability density be greater than the 1σ lower limit for an object with $S/N_{NB} = 5$ and $i2 - NB816 = 1.2$. The second requirement is designed to exclude objects that meet the minimum $i2 - NB816$ requirement but with large uncertainties.

Calculating the probability density for the color of each object is complicated somewhat by fluxes that are formally undetected. To calculate a physically motivated uncertainty for a color that is based on a non-detected flux (which may be negative), we used a set of

artificial sources to generate probability density functions (PDF) for non-detected fluxes, with the prior that the true flux must be positive. We added artificial sources with known, positive fluxes (F_{true}) in random positions across the field and then measured the PSF fluxes (F_{meas}) of these artificial sources as previously described. The distribution of F_{true} values associated with objects that have a given F_{meas} represents a PDF that can be used for assessing the uncertainty in an object's color. The resulting PDF is a Gaussian centered on F_{meas} and FWHM$\sim \sigma_{meas}$, with negative values truncated. We therefore take the probability density function for measured flux values associated with real sources, positive and negative, to be a Gaussian with $\mu = F_x$ and $\sigma = \sigma_x$, with negative values truncated and re-normalized to unity.

For simplicity, we express the color criteria as flux ratios. To find the PDF of a flux ratio, we first generate a PDF for each flux value as described above. We then take the ratio of each possible combination of values from the one-dimensional PDFs to generate a two-dimensional PDF for the flux ratio. We then find the total probability that the flux ratio exceeds the minimum color threshold to evaluate the selection criteria.

In addition to the color cuts described above, we also require that $F_{NB816} \geq 7.6F_{r2}$ (or, $r2 - NB816 \geq 2.2$) with at least a 50% probability. This requirement follows from the $i2 - NB816$ and $r2 - i2$ colors above, and is expected due to the decreasing transmission of blue flux from high-redshift objects. This additional check helps to exclude objects with a significant probability of being low-redshift contaminants.

Finally, we adopted a narrow band limit of $NB \leq 25.5$. This is somewhat brighter than the limit of $NB816 \leq 26.0$ used by Becker et al. (2018). The brighter limit was

chosen because, after making completeness corrections (see Section 2.5), we found that our observations were only $\sim 10\%$ complete in the $25.5 \leq NB816 \leq 26.0$ bin. We selected an additional 143 objects in this bin, although they are excluded from the analysis because of the poor completeness.

To summarize, the final selection criteria applied to our LAEs are as follows:

- $NB \leq 25.5$
- $S/N_{NB816} \geq 5$
- $\frac{F_{NB816}}{F_{i2}} \geq 3.0$ (50% probability) and $\frac{F_{NB816}}{F_{i2}} \geq 1.7$ (95% probability)
- $F_{r2} \leq 2\sigma_{r2}$, or $F_{r2} \geq 2\sigma_{r2}$ and $F_{i2}/F_{r2} \geq 2.5$
- $\frac{F_{NB816}}{F_{r2}} \geq 7.6$ (50% probability) and $\frac{F_{NB816}}{F_{r2}} \geq 4.0$ (95% probability)

Finally, objects that pass these criteria are inspected visually to remove moving or spurious sources.

To summarize, our selection criteria are based on ones used in previous works to detect LAEs at $z = 5.7$ with Subaru (e.g., Ouchi et al. 2008; Konno et al. 2017; Shibuya et al. 2018a; Ouchi et al. 2018), but with some modifications. The main differences are that we impose additional probability requirements for the color criteria and add a $\frac{F_{NB816}}{F_{r2}}$ requirement. Following Díaz et al. (2014), we also do not make use of a bluer filter to exclude low-redshift contaminants. We do, however, use a more selective $r2$ criterion than Ouchi et al. (2018) and Shibuya et al. (2018a), who require that LAEs are undetected in $r2$ at 3σ (compared to 2σ in this work) unless they satisfy the $r2 - i2$ color cut.

Spectroscopic follow-up of a subset of LAEs in the J0148 field with Keck/DEIMOS suggests that our selection criteria should yield a high-quality sample of LAEs. We present details of the spectroscopy in Appendix B.

2.5 Results

We now turn to the results of the photometric selection. Using the procedure outlined in Section 2.4.2, we select 641 LAEs in the J0148 field and 428 LAEs in the J1250 field. The number of LAEs selected in the J0148 field is somewhat lower than found by Becker et al. (2018). We discuss the reasons for this difference in Appendix C, but note that the overall spatial distribution of sources is similar. Cutout images for example LAE candidates selected in the J0148 field (top three rows) and J1250 field (bottom three rows) are shown in Figure 2.2. The cutout images are $10''$ on each side and centered on the LAE candidate. Each row shows an example candidate of a different narrowband magnitude (shown at the left) in the $r2$, $i2$, and $NB816$ bands (left to right). The examples were chosen to have S/N_{NB816} near the median value for objects of similar magnitude.

The surface density of the LAE candidates within $45'$ of the quasar position in both fields as a function of their $NB816$ magnitude is shown in Figure 2.3. Raw values are shown with open markers, and completeness-corrected values are shown with filled markers. We calculate the completeness correction as a function of both distance from the quasar position and $NB816$ magnitude by injecting a catalog of artificial LAE candidates across the field, then putting them through the LAE selection procedure. The completeness correction

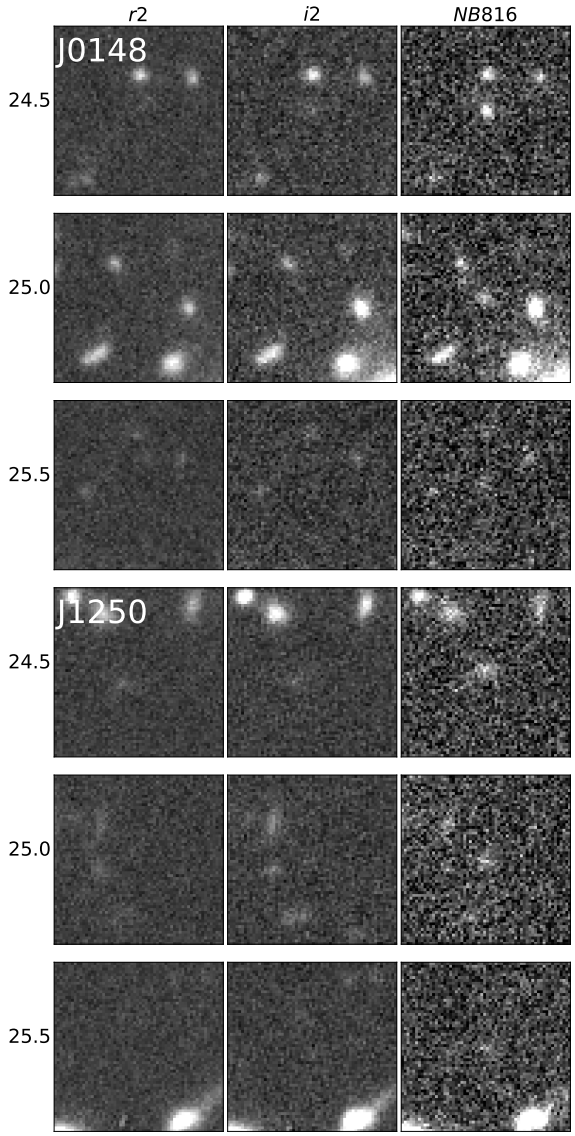

Figure 2.2 Example LAE candidates selected in the J0148 (top three rows) and J1250 (bottom three rows) fields with the criteria described in Section 2.4.2. The cutout images are $10''$ on each side and centered on the LAE position. Each row shows images of a sample candidate of a different narrowband magnitude (shown at the left) in the $r2$, $i2$, and $NB816$ bands (left to right). The sample candidates were chosen to have S/N_{NB816} values near the median for objects at similar $NB816$ magnitudes.

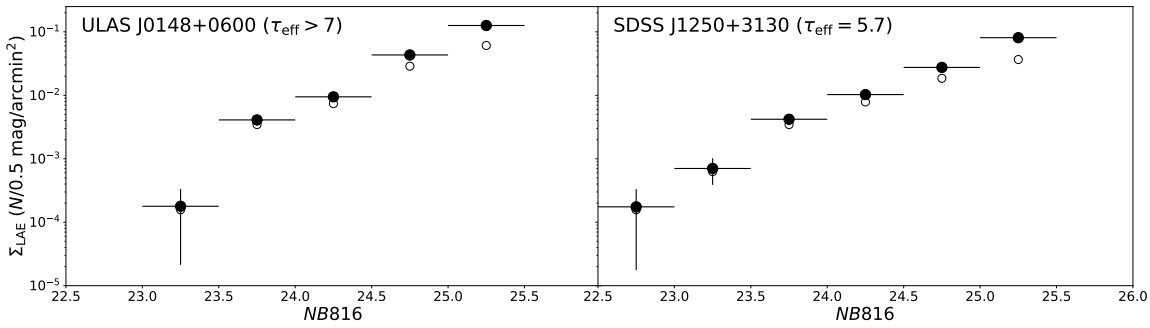

Figure 2.3 Surface density of LAE candidates in the J0148 (left) and J1250 (right) fields. The LAE candidates are binned in 0.5 mag increments. Raw surface densities are shown with open markers. Filled markers show the surface densities with a correction made for completeness (see Section 2.5 and Appendix D). The error bars on the corrected measurements are 68% Poisson intervals.

applied to the real LAE candidates is then given by the reciprocal of the fraction of artificial LAEs detected in each bin. The correction factor adjusts for variations in sensitivity across the field and for loss of area covered by bright foreground sources. The completeness as a function of $NB816$ magnitude and distance from the quasar for both fields is given in Appendix D.

The spatial distribution of selected LAEs in each field is shown in Figure 2.4. LAE candidates are shown with colors corresponding to their NB816 magnitudes. The quasar is centered in each field and denoted with a star. Dotted concentric circles are plotted in increments of 10 h^{-1} Mpc. The solid outer circle shows the edge of the field of view, $45'$ from the quasar.

LAE candidates are shown plotted over a surface density map. We create the surface density map for the LAE candidates in each field by superimposing a regular grid of $0.24'$ (0.4 h^{-1} Mpc) pixels onto the field. In each grid cell, we find the surface density by kernel density estimation using a Gaussian kernel of bandwidth $1.6'$. We then normalize

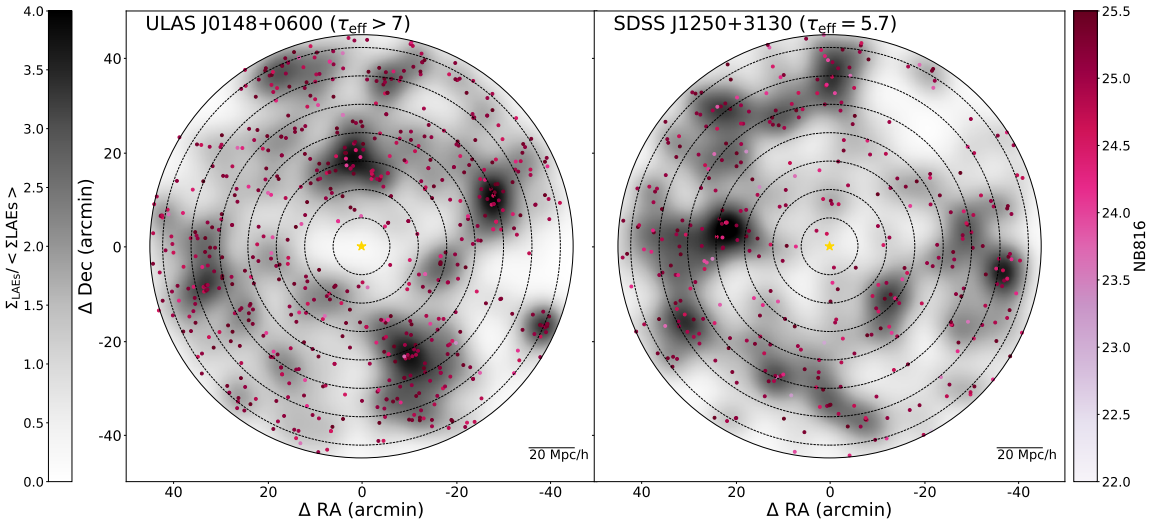

Figure 2.4 Distribution of LAE candidates in the J0148 (left) and the J1250 (right) fields. Each field is shown centered on the quasar (gold star). LAE candidates are shown with a color that indicates their narrowband magnitude. Shading indicates the surface density of LAE candidates at each position, which is is calculated by kernel density estimation using a Gaussian kernel and normalized by the mean surface density measured across the entire field. Concentric, dotted circles are shown in increments of 10 h^{-1} Mpc projected distance from the quasar. The solid circle marks the edge of the field of view, $45'$ from the quasar.

the grid by the average surface density of the field.

We calculate the surface density of the LAE candidates as a function of radius. The raw surface density is measured in 10 h^{-1} Mpc concentric annuli centered on the quasar position and then corrected for completeness. The corrected surface density is shown as a function of projected distance from the quasar for each field in Figure 2.5. The horizontal line represents the mean background surface density of LAE candidates, averaged over $15' \leq \Delta\theta \leq 40'$. The surface density measurements for the J0148 and J1250 fields are summarized in Tables 2.5 and 2.5, respectively.

The key result from Becker et al. (2018) is unchanged; Figure 2.4 shows a marked underdensity within 20 h^{-1} Mpc of the quasar in the J0148 field. The LAE catalog presented here and that presented in Becker et al. (2018) are largely consistent within the expected variations in LAE selection at the faintest magnitudes, where the sample is $\sim 50\%$ complete, and display the same large-scale structures. We estimate that 15% of the objects appearing in each catalog are affected by the flux issues discussed in Section 2.4.1. A more detailed comparison is given in Appendix C.

We also find a deficit of LAEs in the inner 20 h^{-1} Mpc of the J1250 field. This result is consistent with the J0148 field, and confirms the association between highly opaque sightlines and underdense regions in a second field.

We note that the two fields vary in the observed surface density of LAEs; we select 641 LAEs in the J0148 field and 428 in the J1250 field in the same survey volume. While our main result is based on a differential measurement of the LAE surface density within each field, one might also wonder about the variance in LAE density between the

two fields. We can gauge whether this variance is reasonable using a simple linear bias treatment, which is accurate for the large volume probed by our survey (see, e.g., Trapp & Furlanetto 2020). Using the Trac et al. (2015) halo mass function and its linear bias expansion with the standard scaling method (Tramonte et al., 2017; Trapp & Furlanetto, 2020), we expect $\sim 535 \pm 100$ halos of mass $\sim 1.7 \times 10^{11}$ $M_\odot$ dark matter halos in each of our fields, where the "error" is the 1σ sample variance. In this scenario, the two fields are within $\sim 1\sigma$ of the expected value. If, however, only one quarter of halos contain LAEs, the number density would correspond to 7×10^{10} $M_\odot$ halos, which have a fractional standard deviation due to sample variance of ~ 0.16, still consistent with the observed fields. Both of these scenarios are reasonable in light of independent measurements of LAE properties at $z \sim 6$. For example, Khostovan et al. (2019) estimate halo masses $\sim 10^{11}$ $M_\odot$ for LAEs via clustering, while Stark et al. (2010) find that $\sim$25–50% of galaxies have strong Lyman-α emission lines.

Gangolli et al. (2021) similarly find that large-scale structure is sufficient to explain the significant field-to-field variations of $z = 5.7$ LAEs in the SILVERRUSH survey (Ouchi et al., 2018). In contrast, they argue that patchy reionization is unlikely to drive these variations because, at the end of reionization, the neutral gas is largely confined to voids, where it should obscure fewer galaxies. We note that our fields are somewhat unusual in that they were selected to have high IGM Lyα opacities at the field center. Even so, the overall variation in number mean density between fields appears to be consistent with cosmic variance in the number density of LAE hosts at this redshift.

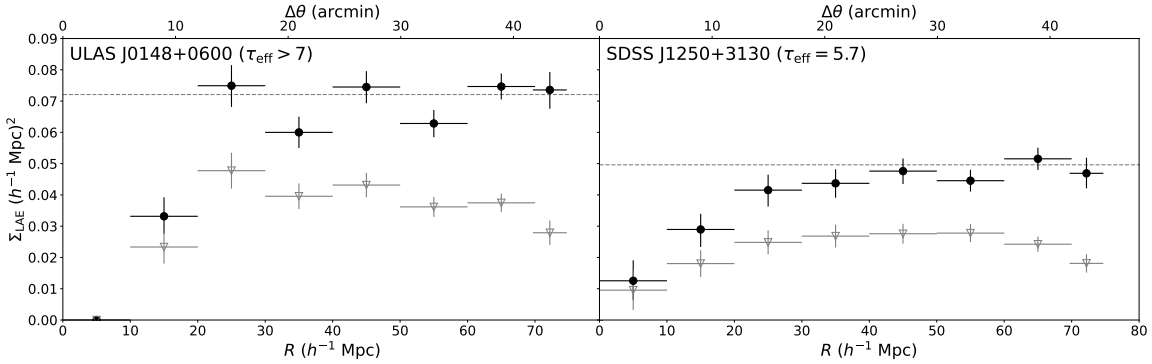

Figure 2.5 Surface density of LAEs in the J0148 (left) and J1250 (right) fields. The filled black circles show corrected surface density, and the unfilled gray triangles show the uncorrected measurements. The surface density is measured as a function of projected distance from the quasar in annual bins of 10 h^{-1} Mpc, except for the outermost bin which is 4.5 h^{-1} Mpc. The dotted line represents the mean surface density of LAE candidates that lie within $15' \leq \Delta\theta \leq 40'$of the quasar. Horizontal error bars show the width of the annuli, and vertical error bars are 68% Poisson intervals.

Table 2.2 LAE Number Density in the J0148 Field

R (Mpc)	N_{LAES}	N_{corr}	Σ_{LAE} (Mpc h^{-1})^2
$5(0-10)$	0	0	0.00
$15(15-25)$	22	31	$0.033\ (0.028-0.039)$
$25(20-30)$	75	118	$0.075\ (0.068-0.081)$
$35(30-40)$	87	132	$0.060\ (0.055-0.065)$
$45(40-50)$	122	211	$0.075\ (0.069-0.080)$
$55(50-60)$	125	217	$0.063\ (0.058-0.067)$
$65(60-70)$	153	305	$0.075\ (0.071-0.079)$
$72(70-74.5)$	57	150	$0.074\ (0.68-0.079)$

[a] Completeness corrected

Table 2.3 LAE Number Density in the J1250 Field

R (Mpc)	N_{LAES}	N_{corr}	Σ_{LAE} (Mpc h^{-1})^2
$5(0-10)$	3	4	$0.013\ (0.006-0.019)$
$15(15-25)$	17	27	$0.030\ (0.023-0.034)$
$25(20-30)$	39	65	$0.042\ (0.036-0.046)$
$35(30-40)$	59	96	$0.044\ (0.039-0.048)$
$45(40-50)$	78	135	$0.048\ (0.043-0.052)$
$55(50-60)$	96	154	$0.045\ (0.041-0.048)$
$65(60-70)$	99	210	$0.052\ (0.048-0.055)$
$72(70-74.5)$	37	196	$0.047\ (0.042-0.052)$

[a] Completeness corrected

2.6 Analysis

2.6.1 Comparison to Models for Opaque Sightlines

We now compare our observations to models that attempt to explain the large-scale fluctuations in IGM Lyα opacity at $z \lesssim 6$. We consider six variations on three main types of models: fluctuating UVB, fluctuating temperature, and ultra-late reionization. We refer the reader to the introduction for a more detailed description of these models.

The first type of model is defined by large-scale fluctuations in the UVB. We consider two galaxy-driven models, one from Davies & Furlanetto (2016) and one from Nasir & D'Aloisio (2020). In these models, UVB fluctuations are driven by the clustering of ionizing sources and a short and spatially variable mean free path. The Nasir & D'Aloisio (2020) model is based on an "early" (completed by $z \simeq 6$) reionization simulation and also includes temperature fluctuations. In these models, high-opacity lines of sight are typically associated with underdense regions, where the UVB is suppressed. We also consider a quasar-driven UVB model based on Chardin et al. (2015, 2017). In this model, high-opacity lines of sight may be associated with a wide range of densities provided that they are in regions far from quasars, where the UVB is low. We note that this model is disfavored by the fact that quasars may only provide a small fraction of the UVB at these redshifts (e.g., McGreer et al. 2018; Parsa et al. 2018; Kulkarni et al. 2019b), but consider it here for

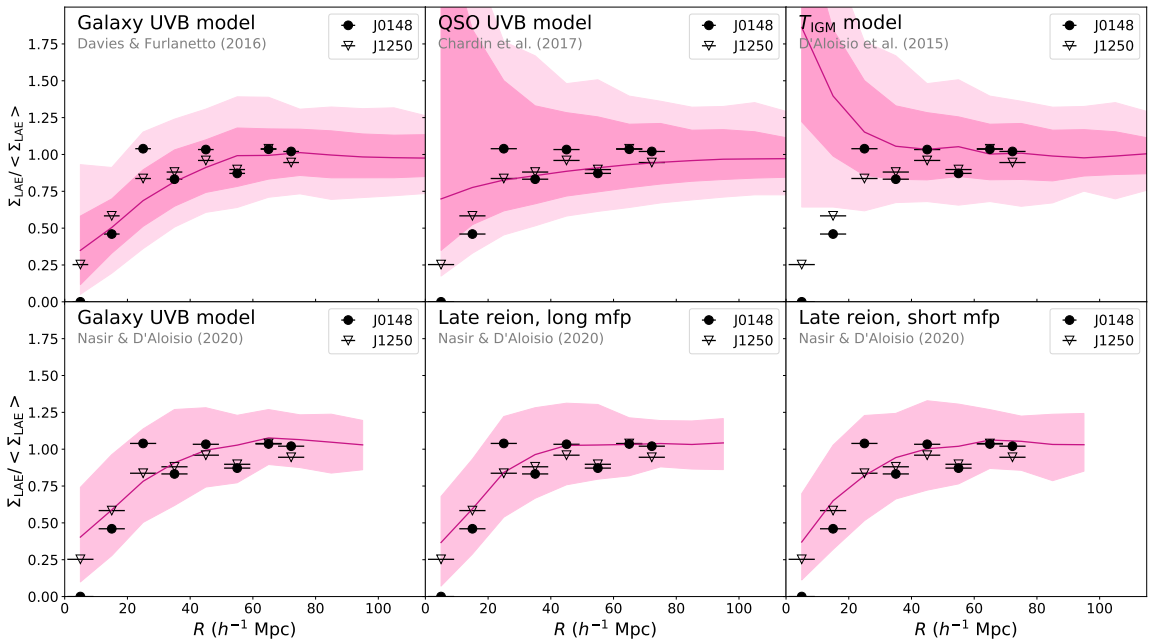

Figure 2.6 Comparison of the observed radial distribution of LAE candidates in the J0148 (filled circles) and J1250 (open triangles) fields to model predictions. The top row shows predictions from the galaxy UVB model based on Davies & Furlanetto (2016) (top left), the QSO UVB model based on Chardin et al. (2015, 2017) (top center), and the fluctuating temperature model from D'Aloisio et al. (2015) (top right). The bottom row shows predictions from Nasir & D'Aloisio (2020), including their galaxy UVB (early reionization) model (bottom left), late reionization model with a long mean free path (bottom center), and late reionization model with a short mean free path (bottom right)
. All model predictions are for highly opaque lines of sight ($\tau_{\rm eff} \geq 7$). The horizontal error bars on the measured data points indicate the width of the bins, which is 10 h^{-1} Mpc for all except the outermost bin, which is 4.5 h^{-1} Mpc. The solid lines show median model predictions, which are averaged over 10 h^{-1} Mpc bins throughout the simulation. In the top panels, the dark- and light-shaded regions show 68% and 95% ranges subtended by the mock samples drawn from the simulation. The shaded regions in the lower panels show the 90% range. All surface densities are given as a fraction of the mean surface density measured over $15' \leq \theta \leq 40'$.

completeness.

The second type of model is from D'Aloisio et al. (2015), and is defined by large-scale temperature fluctuations. In this model, highly opaque lines of sight are associated with overdensities that reionized early and have had sufficient time to cool.

The third type of model is defined by reionization being incomplete at $z = 6$. We consider two ultra-late reionization models from Nasir & D'Aloisio (2020). These models include both regions of neutral hydrogen and a fluctuating ionizing background driven by clustered ionizing sources and a finite mean free path. At $z = 5.8$, the "long mean free path" model has a hydrogen neutral fraction of $\langle \chi_{\rm H\,I} \rangle = 0.14$ and a mean free path of $\langle \lambda_{\rm mfp}^{912} \rangle = 27\ h^{-1}$ Mpc, while the "short mean free path" model has $\langle \chi_{\rm H\,I} \rangle = 0.10$ and $\langle \lambda_{\rm mfp}^{912} \rangle = 9\ h^{-1}$ Mpc.

Predictions for the late reionization models in Nasir & D'Aloisio (2020) are qualitatively consistent with those from Keating et al. (2020b) for opaque lines of sight. Predictions for the Nasir & D'Aloisio (2020) models are taken directly from that work. All others are as implemented in Becker et al. (2018). The LAE modelling is done using a similar approach in all cases. We refer the reader to these papers for details, but briefly summarize the method here. Galaxies are assigned to dark matter halos via abundance matching to the measured UV luminosity function of Bouwens et al. (2015). The spectra are modeled with a power-law continuum and a Lyα emission line, with rest-frame equivalent widths drawn from the empirically calibrated models of Dijkstra & Wyithe (2012).

The modelled LAE populations are then used to construct expected surface density profiles for highly opaque lines of sight. Becker et al. (2018) use sightlines with $\tau_{\rm eff} \geq 7$

measured on 50 h^{-1} Mpc scales. This scale is somewhat shorter than the lengths of the J0148 and J1250 troughs (110 h^{-1} Mpc and 81 h^{-1} Mpc respectively); however, Davies et al. (2018a) compared predictions for the surface density of LAEs as a function of $\tau_{\rm eff}$ on both 50 h^{-1} and 110 h^{-1} Mpc scales and found that the predictions were not highly sensitive to this choice. Nasir & D'Aloisio (2020) use the 100 longest troughs in each simulation to make their predictions, typically 80−100 h^{-1} Mpc in length, which is comparable to the lengths of the J0148 and J1250 troughs.

We compare these model predictions to the measured LAE surface density in the J0148 and J1250 fields in Figure 2.6. The top panel shows, from left to right, the galaxy UVB model based on (Davies & Furlanetto, 2016), the QSO UVB model based on (Chardin et al., 2017), and the fluctuating temperature model based on (D'Aloisio et al., 2015). The lower panel shows the three models from Nasir & D'Aloisio (2020): the first (left) is a galaxy UVB model, the second (center) is the ultra-late reionization scenario with a long mean free path, and the third (right) is the ultra-late reionization scenario with a short mean free path.

The predictions from each model are averaged over 10 h^{-1} Mpc bins. The solid lines show the median prediction. In the top panels, the dark- and light-shaded regions indicate the 68% and 95% ranges, respectively, subtended by the mock samples drawn from the simulation. In the lower panel, the shaded regions indicate the 10th and 90th percentiles. All surface densities are normalized by the mean surface density in the field measured over $15 \leq \theta \leq 40$. We note that these model predictions are made for sightlines with $\tau_{\rm eff} \geq 7$, while the J1250 sightline has $\tau_{\rm eff} \simeq 6$. Davies et al. (2018a), however, find

that the predictions for these opacities are very similar.

In both the J0148 and J1250 fields, we observe a decrease in LAE surface density within 20 h^{-1} Mpc of the quasar. As shown in Figure 2.6, this deficit of LAEs surrounding highly opaque lines of sight is consistent with galaxy UVB and late reionization models, but strongly disfavors the temperature model. We thus demonstrate that the association between high Lyα opacity and low galaxy density first reported by Becker et al. (2018) extends to at least two fields. While Becker et al. (2018) considered only fluctuating UVB and temperature models, moreover, here we show that the observed opacity-density relation is consistent with models where reionization extends to $z < 6$.

2.7 Summary

We present a selection of Lyman-alpha emitting galaxies (LAEs) using Subaru HSC narrow-band imaging in the fields surrounding two highly opaque quasar sightlines, towards ULAS J0148+0600 ($\tau_{\rm eff} \geq 7$) and SDSS J1250+3130 ($\tau_{\rm eff} = 5.7 \pm 0.4$). The observations establish the LAE density expected in the vicinity of two giant Lyα troughs, which we use to test IGM models that predict a relationship between opacity and density. The results for the J0148 field are an update to those previously reported by Becker et al. (2018), here using improved photometric measurements and more stringent LAE selection criteria. Observations of the J1250 field are presented here for the first time.

In both fields, we find a deficit of LAEs within 20 h^{-1} Mpc of the quasar sightline. This confirms the results of Becker et al. (2018) in the J0148 field, and demonstrates in a second field that long, highly opaque Lyα troughs are associated with underdense regions

as traced by LAEs.

These observations provide a direct test of three major types of model that attempt to reproduce the large-scale scatter in Lyα opacity at $z \simeq 5.5$–6: fluctuating ultraviolet background models, where the UVB is produced either by galaxies (Davies & Furlanetto, 2016; D'Aloisio et al., 2018; Nasir & D'Aloisio, 2020) or quasars (Chardin et al., 2015, 2017); the fluctuating temperature model (D'Aloisio et al., 2015); and ultra-late reionization models (Kulkarni et al., 2019a; Nasir & D'Aloisio, 2020; Keating et al., 2020a,b). Our results disfavor the temperature model but are consistent with predictions made by galaxy-driven UVB models, in which highly opaque troughs correspond to low-density regions with a suppressed ionizing background. The results are also consistent with ultra-late reionization models, in which long troughs arise from the last remaining islands of neutral hydrogen, which are also predicted to occur in low-density regions. There is some overlap between these two types of models, as the ultra-late reionization models also include strong UVB fluctuations. The ultra-late reionization model is distinguished by the presence of neutral islands at $z < 6$.

Our results are consistent with a number of recent observations that point towards a late and rapid reionization scenario that has its midpoint at $z \sim 7 - 8$ and ends at $z \leq 6$. A growing body of work is reconsidering the long-standing conclusion that reionization was complete by $z = 6$ (e.g., Kulkarni et al. 2019a; Keating et al. 2020a,b; Nasir & D'Aloisio 2020; Choudhury et al. 2021; Qin et al. 2021), and therefore discriminating between late reionization and fluctuating UVB models is of great interest.

This work has focused on fields surrounding highly opaque lines of sight, but further

insight may come from fields at the opposite extreme of Lyα opacity. UVB models predict that highly transmissive sightlines should be associated with galaxy overdensities producing a strong ionizing background (Davies et al., 2018a). In contrast, late reionization models predict that, in some cases, transmissive sightlines should be associated with low-density regions that have been recently reionized (Keating et al., 2020b), and may generally arise from a range of overdensities (Nasir & D'Aloisio, 2020). Establishing the density field surrounding highly transmissive sightlines may therefore prove to be a useful test of these competing models.

Chapter 3

The Relationship Between IGM Lyα Opacity and Galaxy Density Near the End of Reionization

3.1 Abstract

Observed scatter in the Lyα opacity of quasar sightlines at $z < 6$ has motivated measurements of the correlation between Lyα opacity and galaxy density, as models that predict this scatter make strong and sometimes opposite predictions for how they should be related. Our previous work associated two highly opaque Lyα troughs at $z \sim 5.7$ with a deficit of nearby Lyman-α emitting galaxies (LAEs). In this work, we extend our range of Lyα opacity to include two of the most highly transmissive lines of sight at this redshift, towards the $z = 6.02$ quasar SDSS J1306+0356 and the $z = 6.17$ quasar PSO J359-06.

We find that both low-opacity fields are underdense in LAEs within 10 h^{-1} Mpc of the quasar sightline. The Lyα troughs are also underdense, although to larger lateral extent (within $\gtrsim$ 20 h^{-1} Mpc of the quasar sightlines). We combine our observations with three additional recently observed fields from the literature to begin to characterize the opacity-density relationship at $z = 5.7$. The seven fields together suggest that while both extremely high- and low-opacity sightlines tend to be associated with low densities, moderate opacities span a wider density range. The results at high opacities are broadly consistent with models that invoke UV background fluctuations and/or late reionization to explain the observed scatter in IGM Lyα opacities at these redshifts. There is tension between some of these models and our results at low opacities, however, as the models tend to associate lower IGM Lyα opacities with higher densities. Although the number of fields surveyed is still small, the observed association of low opacity with low density at these redshifts may support a scenario in which the ionizing background in low-density regions increases more rapidly than some models suggest once they have been ionized. Elevated gas temperatures from recent reionization may also be making these regions more transparent.

3.2 Introduction

Understanding when and how hydrogen reionization proceeded is of great interest for several reasons. First, the timing and duration of reionization have implications for our understanding of the first luminous sources. Second, our understanding of the physical state of the IGM is important context for high-redshift observations that are affected by absorption by intervening material. Lastly, reionization functions as a test of our dark mat-

ter and galaxy formation models, which must produce sources consistent with reionization constraints. There are two primary open questions that current reionization studies are attempting to address: the timing of reionization, including when it ended, and what the main sources of ionizing photons are (see Wise (2019) for a review).

A number of observations suggest that much of reionization took place between z$\sim$ 6$-$8. Damping wings in quasar spectra at $z \geq 7$ suggest that the IGM is still substantially neutral at those redshifts (Mortlock et al., 2011; Greig et al., 2017; Bañados et al., 2018; Greig et al., 2019; Davies et al., 2018b; Wang et al., 2020). Galaxy surveys infer that a large portion of the universe remains neutral at $z \sim 7-8$ from the fraction of UV-selected galaxies that display Lyα emission (Mason et al., 2018; Jung et al., 2020; Morales et al., 2021). Measurements of the cosmic microwave background suggest a midpoint at $z \simeq 8$ (Planck Collaboration et al., 2020). The thermal history of the IGM down to $z \sim 5$ also suggests that much of reionization occurred at $z \sim 7$–8. (Boera et al., 2019; Gaikwad et al., 2020)

Until recently, reionization was thought to be essentially complete by $z \sim 6$ due to the observed onset of Lyα transmission in quasar spectra (Fan et al., 2006). On the other hand, a large scatter in Lyα opacity has been observed in quasar sightlines at $z \leq 6$ (Fan et al., 2006; Becker et al., 2015; Bosman et al., 2018; Eilers et al., 2018; Yang et al., 2020; Bosman et al., 2021; Zhu et al., 2021; Zhu et al., 2022). The Lyα forest at these redshifts exhibits highly opaque Lyα and Lyβ "troughs" down to $z \simeq 5.3$, the most extreme example of which is a 110 h^{-1} Mpc Lyα trough observed towards ULAS J0148+0600 (Becker et al., 2015). Both these troughs and the overall scatter in Lyα opacity have been shown

to be inconsistent with a fully reionized IGM in which the ultraviolet background (UVB) is homogeneous (Becker et al., 2015; Bosman et al., 2018; Eilers et al., 2018; Yang et al., 2020; Bosman et al., 2021; Zhu et al., 2021; Zhu et al., 2022; Lidz et al., 2006).

The scatter in Lyα opacity and the presence of highly opaque sightlines such as that towards ULAS J0148+0600 suggests that there are large-scale variations in the hydrogen neutral fraction at these redshifts. For an ionized IGM, the neutral hydrogen fraction is set by the photoionization rate, the gas temperature, and the total hydrogen density, which broadly suggests multiple scenarios. The first is that large-scale fluctuations in the UVB are the primary cause of the scatter in Lyα opacity (Davies & Furlanetto, 2016; Nasir & D'Aloisio, 2020). In this scenario, we would qualitatively expect a transmissive sightline to span a high-density region, in close proximity to ionizing sources. In contrast, opaque sightlines would more typically be associated with voids. The second is that the scatter in Lyα opacity is primarily driven by large-scale fluctuations in temperature (D'Aloisio et al., 2015) In this scenario, a transmissive region would be underdense, recently reionized, and hot, whereas an opaque region would have been reionized early due to its high density of ionizing sources and able to cool for longer, producing a higher recombination rate. Lastly, it is possible that reionization is still ongoing at $z < 6$ and highly opaque troughs like that towards ULAS J0148+0600 correspond to islands of neutral hydrogen that have not yet been reionized (Kulkarni et al., 2019b; Keating et al., 2020a; Nasir & D'Aloisio, 2020). This "ultra-late" reionization scenario is not mutually exclusive with the other factors; fluctuations in the UVB and temperature would still be expected.

There are a number of models that make use of these physical processes to explain

the observed scatter in Lyα opacity. Notably, the predictions they make for the relationship between opacity and density can be tested with observations. Fluctuating UVB models have been considered by numerous authors, and there are galaxy-driven variations (Davies & Furlanetto, 2016; Nasir & D'Aloisio, 2020) and quasar-driven variations (Chardin et al., 2015, 2017). We note that because quasars are rare, in quasar-driven UVB models the Lyα opacity is less tightly coupled to density than it is in galaxy-driven UVB models. The quasar-driven model is independently disfavored because the observed number density of quasars is not high enough to produce the required number of ionizing photons for quasars to be the main sources driving reionization (McGreer et al., 2018; Kulkarni et al., 2019b; Faisst et al., 2022). Additionally, a quasar-driven hydrogen reionization may be incompatible with current constraints on helium reionization (D'Aloisio et al., 2017; McGreer et al., 2018; Garaldi et al., 2019). Similarly, the temperature model (D'Aloisio et al., 2015) is disfavored, at least as an explanation for the full range of opacities, by the observations of Becker et al. (2018), Kashino et al. (2020), Christenson et al. (2021), and Ishimoto et al. (2022), who found that highly opaque quasar sightlines are associated with galaxy underdensities. The late reionization models commonly include UVB fluctuations, but are distinct from pure UVB models in that regions of the IGM are still significantly neutral below $z = 6$. In these models, some highly opaque quasar sightlines correspond to neutral islands (Keating et al., 2020b). On the other hand, Nasir & D'Aloisio (2020) find that transmissive sightlines span a range of galaxy densities, but tend towards higher values. However, $\sim 10 - 15\%$ of transmissive sightlines in those models correspond to galaxy underdensities. Keating et al. (2020b) argue that sightlines where high transmission is correlated with galaxy underdensity

should correspond to regions that are hot and recently reionized.

Observations spanning a range of Lyα opacity is necessary to robustly test the predictions from these reionization models and characterize the $z \sim 5.7$ opacity-density relationship. Previous studies have linked highly opaque quasar sightlines to galaxy underdensities towards the quasars ULAS J0148+0600 (Becker et al., 2018; Kashino et al., 2020; Christenson et al., 2021),SDSS J1250+3130 (Christenson et al., 2021), and SDSS J1630+4012 (Ishimoto et al., 2022). Ishimoto et al. (2022) also observe two sightlines of lower opacity, SDSS J1137+3549 and SDSS J1602+4228, and find that they correspond to galaxy overdensities.

In this paper, we extend our observations to some of the most highly transmissive sightlines known at these redshifts. We characterize the density of Lyman-α emitting galaxies (LAEs) towards the quasars SDSS J1306+0356, which has a Lyα effective opacity of $\tau_{\rm eff} = 2.6$, and PSO J359-06, which has a Lyα effective opacity of $\tau_{\rm eff} = 2.7$, both measured over 50 h^{-1} Mpc windows centered at $z = 5.7$, the redshift at which we select LAEs. We additionally include new selections of LAEs in the J0148 and J1250 fields, previously published in Becker et al. (2018); Christenson et al. (2021) to make comparisons between the four fields as self-consistent as possible. We summarize the observations in Section 3.3, and describe the photometry and LAE selection criteria in Section 3.4. We present the results of LAE selections in Section 3.5, and compare the results to predictions from current models in Section 3.6 before summarizing in Section 3.7. Throughout this work, we assume a ΛCDM cosmology with $\Omega_m = 0.3$, $\Omega_\Lambda = 0.7$, and $\Omega_b = 0.048$. All distances are given in comoving units, and all magnitudes are in the AB system.

Table 3.1 Effective opacity measurements for QSO sightlines referenced in this work

QSO	z_{QSO}	$\tau_{\rm eff}^{50,a}$	$\tau_{\rm eff,b}^{28}$
ULAS J0148+0600	5.998	7.573^{c}	7.329^{c}
SDSS J1250+3130	6.137	5.876^{c}	5.610^{c}
SDSS J1306+0356	6.0330	2.662 ± 0.009	2.475 ± 0.010
PSO J359-06	6.1718	2.680 ± 0.009	2.392 ± 0.009
SDSS J1602+4228[d]	6.079	3.063 ± 0.038	4.898 ± 0.308
SDSS J1137+3549[d]	6.007	2.904 ± 0.040	4.344 ± 0.227
SDSS J1630+4012[d]	6.055[e]	3.857 ± 0.184	4.550 ± 0.477

[a] Effective opacity measured over a 50 h^{-1} Mpc window centered at 8177 Å

[b] Effective opacity measured over the FWHM of the $NB816$ filter (a 28 h^{-1} Mpc window) centered at 8177 Å

[c] Lower limit

[d] From Ishimoto et al. (2022); see Section 3.6.3 for a detailed discussion of these sightlines

[e] Redshift measurement from Becker et al. (2019).

3.3 Observations

3.3.1 QSO Spectra

The four sightlines whose fields we survey in this work were drawn from the sample of Zhu et al. (2021). This sample includes spectra of 55 quasars over $5.5 \leq z \leq 6.5$ taken with the X-Shooter spectrograph on the Very Large Telescope and the Echellete Spectrograph and Imager on Keck, 23 of which are from the XQR-30 VLT Large Programme. Subsets of the four quasar spectra are shown in Figure 3.1, displaying the highly opaque troughs (J0148 and J1250) and the highly transmissive regions (J1306 and J359) near $z = 5.7$ found in these sightlines (Becker et al., 2015, 2019; Zhu et al., 2021). The J1306 sightline has an effective opacity of $\tau_{\rm eff}^{50} = 2.617 \pm 0.009$, where $\tau_{\rm eff} = -\ln\langle \mathrm{F} \rangle$ and F is the mean continuum-

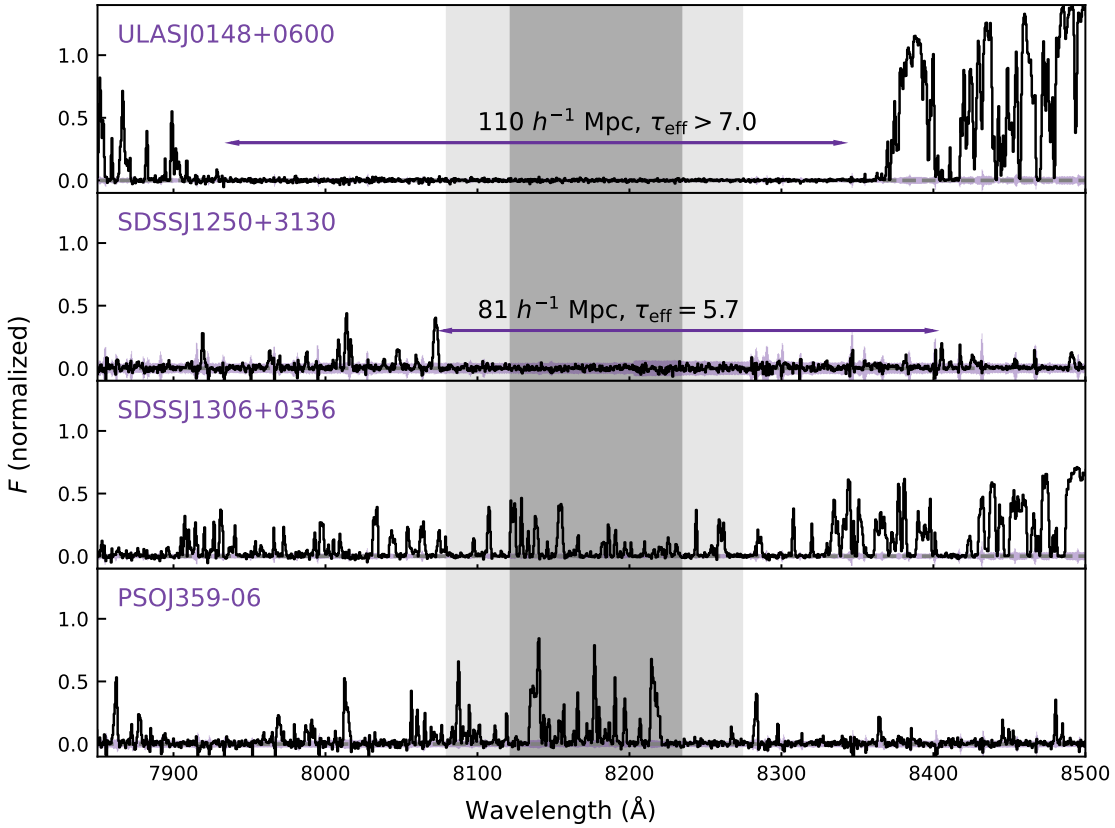

Figure 3.1 Partial spectra of the Lyα forest of quasars ULAS J0148+0600 (X-Shooter), SDSS J1250+3130 (Keck/ESI), SDSS J1306+0356 (X-Shooter), and PSO J359-06 (X-Shooter), whose fields we observe with Subaru/HSC. The J0148 and J1250 sightlines have $\tau_{\rm eff} \geq 7.0$ and $\tau_{\rm eff} = 5.7 \pm 0.4$ measured over 110 and 81 h^{-1} Mpc respectively (trough extent marked with purple arrows). The shaded purple regions indicate the $\pm 1\sigma$ uncertainty interval. The darker shaded gray rectangles indicates the FWHM of the NB816 filter, and the lighter shaded regions indicate a 50 h^{-1} Mpc interval, both centered at 8177 Å; these windows are used to calculate the effective opacity of the sightlines. The effective opacity measurements are summarized in Table 1. These spectra are normalized using PCA fits to their continuum. Note that for the J0148 spectrum, flux at $\lambda > 8350$ Å is part of the quasar proximity zone and not fully normalized.

normalized flux. The J359 sightline has an effective opacity of $\tau_{\rm eff}^{50} = 2.661 \pm 0.009$. For both sightlines, $\tau_{\rm eff}^{50}$ is measured over 50 h^{-1} Mpc windows centered at $z = 5.7$ (8177 Å), which cover $5.632 < z < 5.794$. These two sightlines are some of the most highly transmissive sightlines known at these redshifts (Zhu et al., 2021). Similarly, the J0148 and J1250 are two of the most highly opaque sightlines observed at these redshifts, with large troughs of $\tau_{\rm eff} \geq 7$ measured over 110 h^{-1} Mpc and $\tau_{\rm eff} \geq 5.7 \pm 0.4$ measured over 81 h^{-1} Mpc respectively. Over 50 h^{-1} Mpc windows centered at 8177Å, the sightlines have $\tau_{\rm eff}^{50} \geq 7.0$ and $\tau_{\rm eff}^{50} = 5.03 \pm 0.21$ respectively. We also calculate $\tau_{\rm eff}$ for these sightlines over a 28 h^{-1} Mpc window, which represents the full width at half maximum of the narrowband filter used for LAE selection, and find $\tau_{\rm eff}^{28} \geq 7.329$ for the J0148 sightline, $\tau_{\rm eff} \geq 5.610$ for the J1250 sightline, $\tau_{\rm eff} = 2.475 \pm 0.010$ for the J1306 sightline, and $\tau_{\rm eff} = 2.392 \pm 0.009$ for the J359 sightline. For all of the effective opacity measurements, we adopt a lower limit of $\tau_{\rm eff} \geq -\ln(2\sigma_{\langle F \rangle})$ if the mean flux is detected with less than 2σ significance, or if we measure a negative mean flux. This definition is consistent with previous works (e.g., Eilers et al. 2018). The opacity measurements for sightlines used in this work are summarized in Table 1. We additionally estimate Lyα opacity for these sightlines using our imaging data in Appendix A.

3.3.2 HSC Imaging

Presented here for the first time are imaging data in the J1306 and J359 fields, taken with Subaru Hyper Suprime Cam (HSC). This work also makes use of HSC imaging in the J0148 and J1250 fields, previously presented in Becker et al. (2018) and Christenson et al. (2021). Observations of the J1306 field were made via the HSC queue in April and

Table 3.2 Summary of HSC imaging

	Filter	t_{exp} (hrs)	Seeing[b]	$m^c_{5\sigma,PSF}$	$m^c_{5\sigma,1.5''}$
J0148	$r2$	1.5	0.61	26.3	26.2
	$i2$	2.4	0.71	25.9	25.8
	$NB816$	4.5	0.60	25.1	25.2
J1250	$r2$	2.0[d]	1.07	26.3	26.2
	$i2$	2.5	0.62	26.1	26.0
	$NB816$	2.8	0.73	25.1	25.2
J1306	$r2$	1.3	0.89	26.3	26.2
	$i2$	2.4	0.74	26.1	26.0
	$NB816$	2.8	0.80	25.0	25.1
J359	$r2$	1.5	1.08	26.2	26.3
	$i2$	1.9	0.73	25.8	25.9
	$NB816$	2.2	0.87	25.0	25.2

[a] Median seeing FWHM in combined mosaic.
[b] Magnitude at which 50% of detected sources have $S/N \geq 5$ in the corresponding filter.
[c] Limiting magnitude, given by five times the standard deviation of the flux measured in empty $1.5''$ apertures.
[d] Partially observed during gray time.

June 2019, May 2020, and January and June 2021. Observations of the J359 field were made via the HSC queue in October and November 2019, August 2020, and November 2021. All observations in these fields were made during dark time. As for previous fields surveyed in this program, images were centered at the quasar position. This program makes use of two HSC broadband filters, $r2$ and $i2$, and the narrowband $NB816$ filter, which has a transmission-averaged mean wavelength $\lambda = 8168$ Å and $\geq 50\%$ transmission over 8122 Å$\leq \lambda \leq 8239$ Å.

The observations in all four fields are summarized in Table 3.3.2, as well as the image depth measured in empty $1.5''$ apertures and the median 5σ limiting aperture magnitudes in each band. At the limiting magnitudes, at least 50% of the detected sources have

a signal-to-noise ratio $S/N_{NB816} \geq 5$.

We used version 21 of the LSST Science Pipeline (Ivezić et al., 2008; Jurić et al., 2015) to reduce individual CCDs and combine them into stacked mosaics. The pipeline uses PanStarrs DR1 imaging (Chambers et al., 2016) for photometric calibrations. We used Source Extractor (Bertin & Arnouts, 1996) to create a catalog of $NB816$-detected sources and their spatial coordinates in the stacked mosaics, and then make our own photometric measurements at these spatial coordinates, as described below.

3.4 Methods

3.4.1 Photometry

The LAE selection in this work makes use of aperture fluxes as the primary photometric measurement. This choice is a departure from our previous work, which was based on PSF photometry (Christenson et al., 2021) or CModel fluxes (Becker et al., 2018). As we discuss further in Section 3.6, a major focus of this paper is comparing the four fields to one another, which requires minimizing the effect of variations in depth, seeing, and completeness. While PSF fluxes can be optimized for the detection of faint and unresolved sources, aperture fluxes are less easily impacted by small changes in the seeing and more robust for resolved sources. For that reason, we have opted to accept a lower signal-to-noise ratio and the loss of some faint LAEs from our catalog in favor of a more robust selection.

The source detection and photometric measurements are carried out via the following steps. Source positions are identified in the NB816 stacked mosaic using Source Extractor. At each source position, we measure the flux in a 1.5″ aperture, and also mea-

sure the sky background in a $1.5 - 5''$ annulus around the aperture, excluding pixels labeled as sources by the LSST pipeline. The aperture fluxes are corrected by the measured sky background. These measurements are made independently, at the same position, in each band.

3.4.2 LAE Selection Procedure

Our selection criteria, following Christenson et al. (2021), are based on those of Ouchi et al. (2008). As noted in Christenson et al. (2021), our observations have some disparity in depth between different bands and fields. To ensure a high-quality selection of LAEs, we impose additional requirements that are designed to exclude objects with large uncertainties in their colors. The selection criteria are as follows:

- $NB \leq 25.5$
- $S/N_{NB816} \geq 5.0$
- $\frac{F_{NB816}}{F_{i2}} \geq 3.0$ (50% probability) and $\frac{F_{NB816}}{F_{i2}} \geq 1.7$ (95% probability)
- $F_{r2} \leq 2\sigma_{r2}$, or $F_{r2} \geq 2\sigma_{r2}$ and $F_{i2}/F_{r2} \geq 2.5$
- $\frac{F_{NB816}}{F_{r2}} \geq 7.6$ (50% probability) and $\frac{F_{NB816}}{F_{r2}} \geq 4.0$ (95% probability)

The 95% probability thresholds are the lower bound of the 1σ error of an object with $F_{NB816}/F_{i2} = 3.0$, $F_{i2}/F_{r2} = 2.5$, and $S/N_{NB816} = 5.0$. All objects that satisfy these requirements then undergo a visual inspection to remove spurious sources. Examples of LAEs selected in this manner are shown in Figure 3.2.

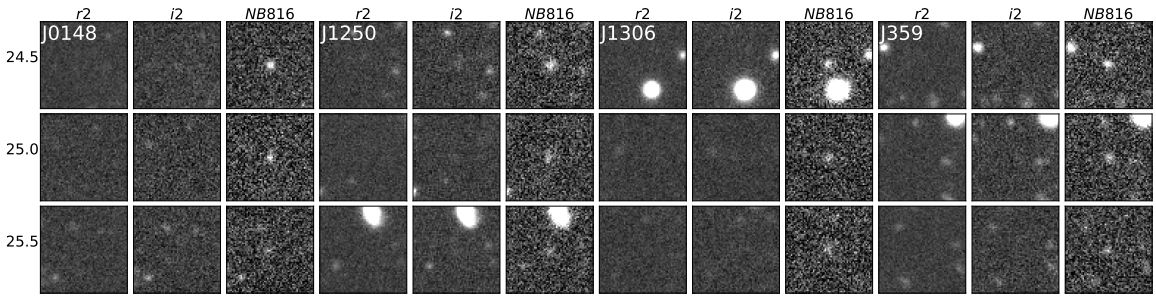

Figure 3.2 Example LAE candidates selected in all four fields with the criteria described in Section 3.4.2. The cutout images are 10 $''$ on each side and centered on the LAE position. For each field, we show an example candidate selected to have NB816 = 24.5, 25.0, and 25.5 (top to bottom) in the $r2, i2$, and NB816 bands (left to right).

3.4.3 Completeness Corrections

We make completeness corrections for the selected catalog of LAEs in two stages. The first stage is to calculate a completeness correction in each field as a function of $NB816$ magnitude and distance from the quasar sightline. This calculation is based on artificially injected LAE candidates, which are placed at randomly generated positions in the field, binned by radius and magnitude, put through the LAE selection procedures described in Section 3.4. The sample is generated such that the artificial LAEs are spread roughly evenly between the magnitude and radius bins, ensuring that there are enough objects in each bin to calculate a completeness correction. The completeness correction is the reciprocal of the fraction of artificial LAEs that were successfully detected in each bin. We show the completeness measured in each field as a function of distance from the quasar position and $NB816$ magnitude in Figure 3.3. The completeness calculations are made down to $NB816 \leq 26.0$, but we only select LAEs to $NB816 \leq 25.5$ in our final catalog because of the low completeness measured in the faintest magnitude bin. This completeness correction

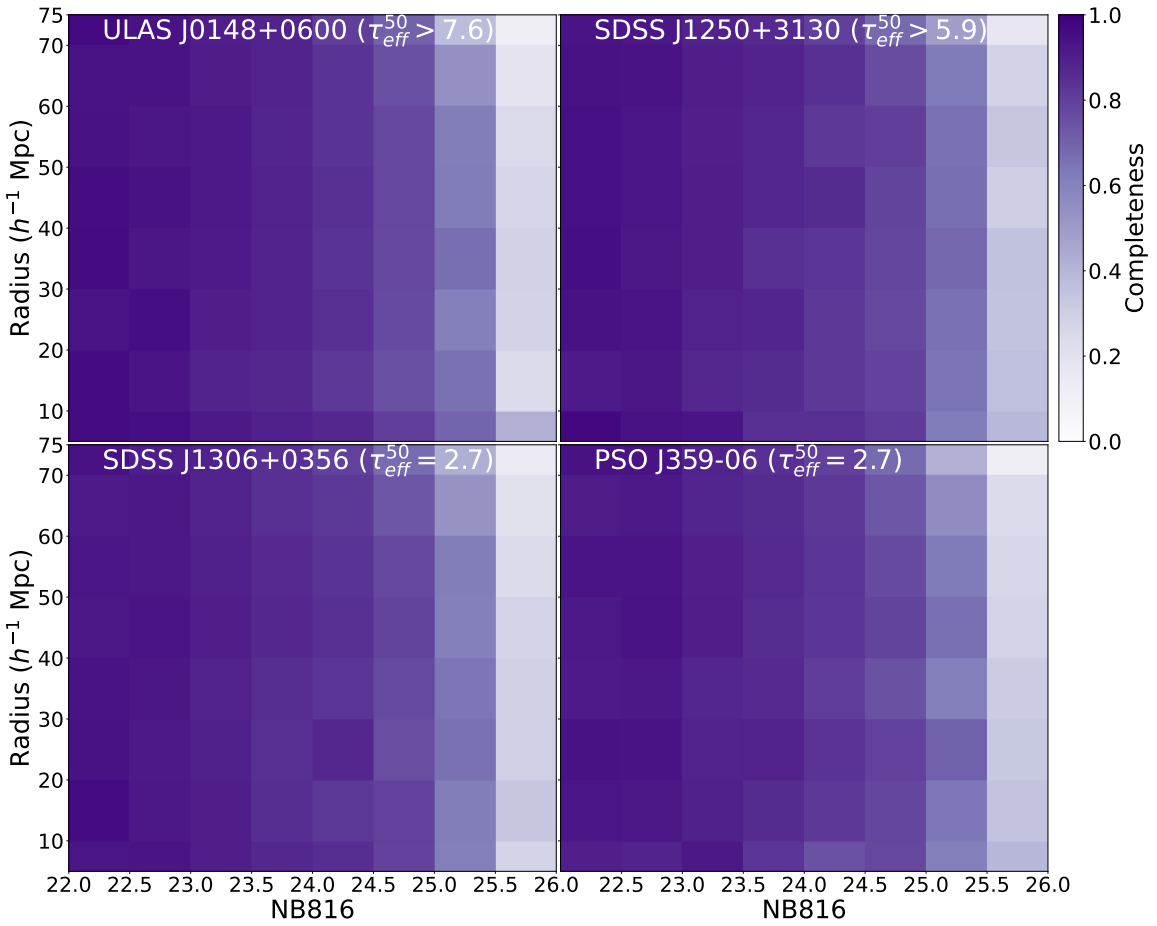

Figure 3.3 Completeness measured in the J0148 (top left), J1250 (top right), J1306 (bottom left) and J359 (bottom right) fields as a function of projected distance from the quasar position and $NB816$ magnitude. The completeness is given by the fraction of artificial LAEs injected into the imaging that were detected by our LAE selection procedure. Note that we have included narrowband magnitudes down to $NB816 = 26.0$; however, we only include sources down to $NB816 = 25.5$ due to the low completeness in the faintest magnitude bin.

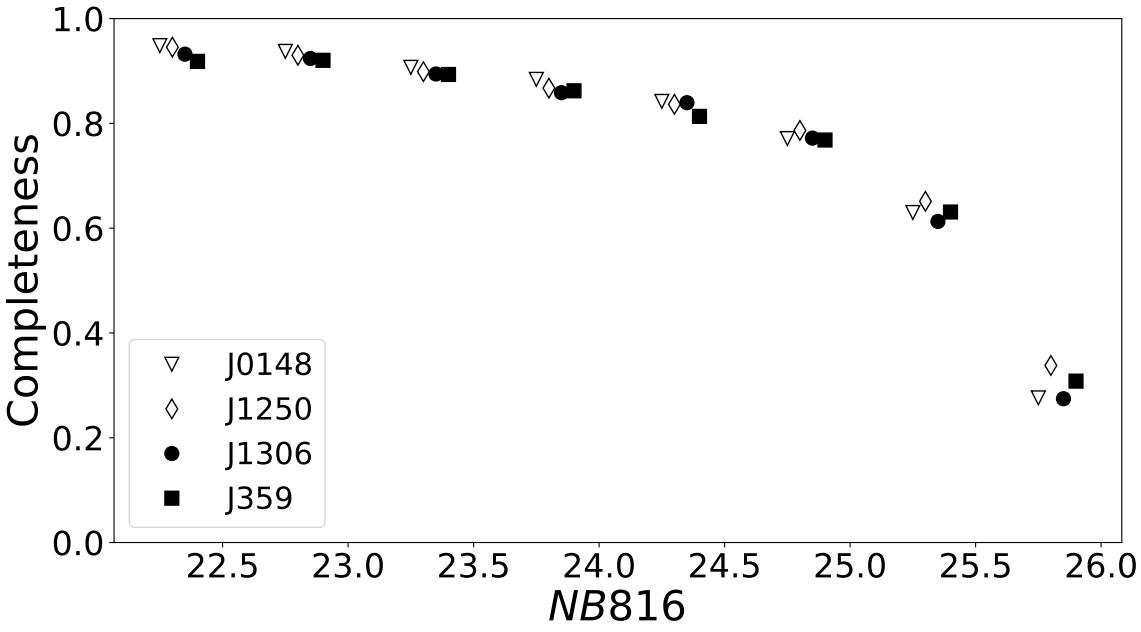

Figure 3.4 Radially averaged completeness measured in the J0148 (filled gray triangles), J1250 (open gray diamonds), J1306 (filled black circles), and J359 (open black squares) fields as a function of $NB816$ radius as a function of distance from the quasar position and $NB816$ magnitude. The fields are offset horizontally for clarity. While we have calculated the completeness for narrowband magnitudes down to $NB816 = 26.0$, our analysis only includes sources down to $NB816 = 25.5$.

is used to correct the measured surface density as a function of radius and magnitude shown in Section 3.5 in Figures 3.5, 3.7, 3.10, and 3.11. We additionally show the radially averaged completeness as a function of $NB816$ magnitude for all four fields surveyed as a part of this program in Figure 3.4.

The second stage is calculating total completeness as a function of position in each field. We use the completeness-corrected magnitude distribution of LAEs detected in all four fields to generate a second set of artificial LAEs in each field, this time with $NB816$ magnitudes drawn from the empirical magnitude distribution. Because these artificial LAEs are representative of the real LAE sample, we can use them to calculate a map of completeness as a function of position. We assign each artificial LAE a flag indicating whether or not it was successfully selected using our LAE selection procedure, and then calculate the surface density of both (i) the full artificial LAE catalog and (ii) the selected artificial LAEs in each field as a function of position. Surface densities are estimated using the kernel density estimation approach described below. The completeness as a function of position is then given by the surface density of the selected LAEs divided by the surface density of the injected LAEs. We calculate these completeness correction maps separately for each field, and apply them to the LAE maps shown in Figure 3.6.

3.5 Results

We select 298 LAEs in the J0148 field, 247 in the J1250 field, 192 in the J1306 field, and 228 in the J359 field using the procedures outlined in section 3.4. The number of LAEs selected in the J0148 and J1250 fields is somewhat lower than found in Christenson et al.

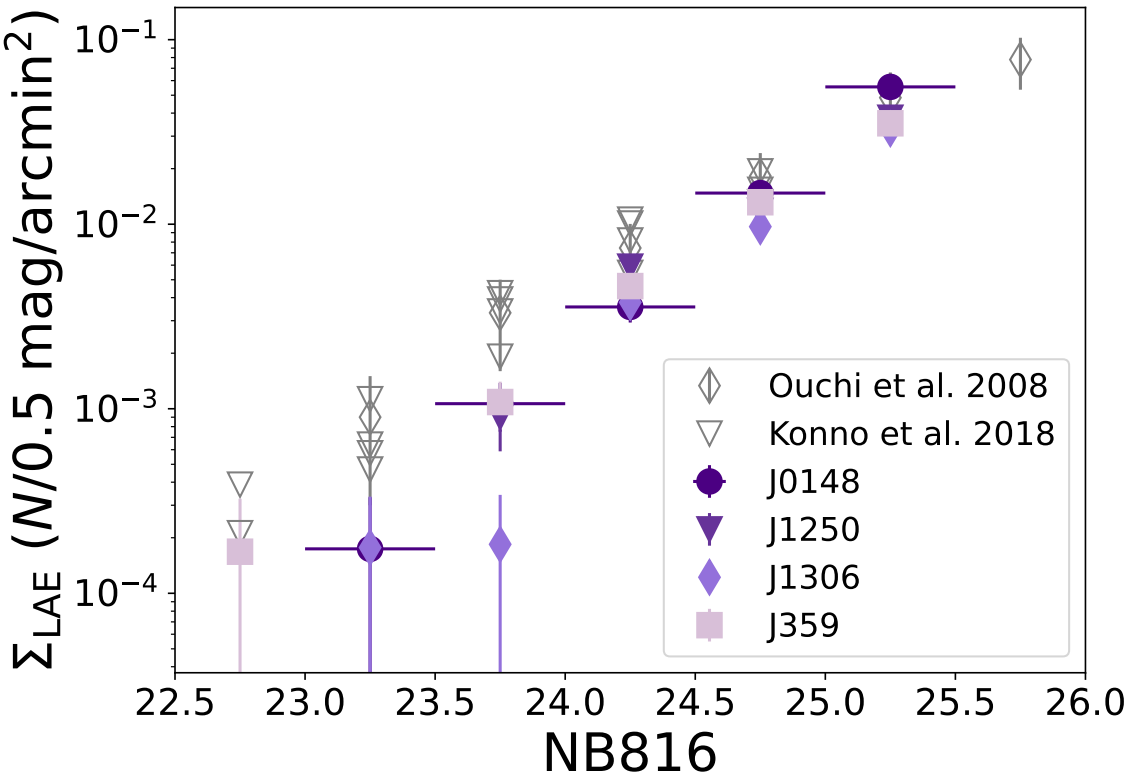

Figure 3.5 Completeness-corrected surface density of LAE candidates in the J0148, J1250, J1306, and J359 fields (filled markers) as a function of their $NB816$ magnitude (see Section 3.4.3 for details on the completeness correction.). The error bars on the completeness-corrected measurements are 68% Poisson intervals. We also show measurements from Konno et al. (2017) (open gray triangles, includes four HSC fields plotted separately) and Ouchi et al. (2008) (open gray diamonds) for comparison.

(2021) due to the use of aperture fluxes, although the spatial distribution of the sources is qualitatively similar. We compare the two selections in more detail in Appendix H. We show the surface density of the LAE catalogs in each field as a function of their $NB816$ magnitude in Figure 3.5. The open circles indicate raw surface density measurements, and the filled circles indicate completeness-corrected measurements. Also included are measurements from Konno et al. (2017) and Ouchi et al. (2008).

Table 3.3 LAE number density as a function of radius

	R (Mpc)	N_{LAEs}	N^a_{corr}	Σ LAE (Mpc h^{-1})^2
J0148	$5(0-10)$	0	0	0.0 (0.0 − 0.0)
	$15(10-20)$	12	17	0.018 (0.013 − 0.022)
	$25(20-30)$	33	50	0.032 (0.028 − 0.036)
	$35(30-40)$	44	61	0.028 (0.024 − 0.031)
	$45(40-50)$	51	76	0.027 (0.024 − 0.03)
	$55(50-60)$	56	86	0.025 (0.022 − 0.027)
	$65(60-70)$	74	126	0.031 (0.028 − 0.034)
	$72(70-74.5)$	28	61	0.03 (0.026 − 0.034)
J1250	$5(0-10)$	2	3	0.01 (0.005 − 0.016)
	$15(10-20)$	9	12	0.013 (0.009 − 0.017)
	$25(20-30)$	21	29	0.019 (0.015 − 0.022)
	$35(30-40)$	32	44	0.02 (0.017 − 0.023)
	$45(40-50)$	37	52	0.018 (0.016 − 0.021)
	$55(50-60)$	61	87	0.025 (0.022 − 0.028)
	$65(60-70)$	63	94	0.023 (0.021 − 0.025)
	$72(70-74.5)$	22	37	0.018 (0.015 − 0.021)
J1306	$5(0-10)$	2	3	0.01 (0.005 − 0.016)
	$15(10-20)$	16	24	0.025 (0.02 − 0.031)
	$25(20-30)$	28	40	0.026 (0.022 − 0.029)
	$35(30-40)$	35	50	0.023 (0.02 − 0.026)
	$45(40-50)$	27	40	0.014 (0.012 − 0.016)
	$55(50-60)$	39	59	0.017 (0.015 − 0.019)
	$65(60-70)$	30	50	0.012 (0.01 − 0.014)
	$72(70-74.5)$	15	31	0.015 (0.013 − 0.018)
J359	$5(0-10)$	1	1	0.004 (0.002 − 0.006)
	$15(10-20)$	11	16	0.017 (0.012 − 0.021)
	$25(20-30)$	22	29	0.019 (0.015 − 0.022)
	$35(30-40)$	32	49	0.022 (0.019 − 0.025)
	$45(40-50)$	34	48	0.017 (0.015 − 0.019)
	$55(50-60)$	46	69	0.02 (0.018 − 0.023)
	$65(60-70)$	57	89	0.022 (0.02 − 0.024)
	$72(70-74.5)$	25	43	0.021 (0.018 − 0.024)

[a] Completeness corrected

Figure 3.6 shows the distribution of LAE candidates in all four fields: J0148 (top left), J1250 (top right), J1306 (bottom left), and J359 (bottom right). In each panel, the field is centered on the quasar position, which is marked with a yellow star. The concentric dotted rings indicate 10 h^{-1} Mpc intervals from the quasar position, and the solid black ring indicates the edge of the field. The LAEs are represented with a color that indicates their $NB816$ magnitude. There are several bright foreground stars in these fields that obscure small portions of the field, which are masked out in white. The grayscale shading indicates the surface density of LAEs. To calculate the surface density, we overlay a grid of $0.24'$ (0.4 h^{-1} Mpc) pixels on the field and then find the surface density in each grid cell by kernel density estimation using a Gaussian kernel with a $1.6'$ bandwidth. This smoothing scale is chosen to match the mean separation between each LAE and its nearest neighbor. The surface density is then completeness-corrected as described in Section 3.4.3 and normalized by the mean surface density of the field over $15 \leq \theta \leq 40$ arcmin. See Appendix G for maps normalized using a global mean surface density, calculated over the $15 \leq \theta \leq 40$ arcmin region of all four fields.

Figure 3.7 shows the surface density of LAEs in each field as a function of distance from the quasar position. We first measure the raw surface density by binning the LAEs into 10 h^{-1} Mpc annuli, and then further bin them by $NB816$ magnitude to apply the completeness correction shown in Figure 3.3. The raw measurements are shown in Figure 3.7 with gray, open circles, and the completeness-corrected measurements are shown with filled, black circles. The horizontal dotted line represents the mean completeness-corrected surface density of the field, which we measure over $15 \leq \theta \leq 40'$. The surface density

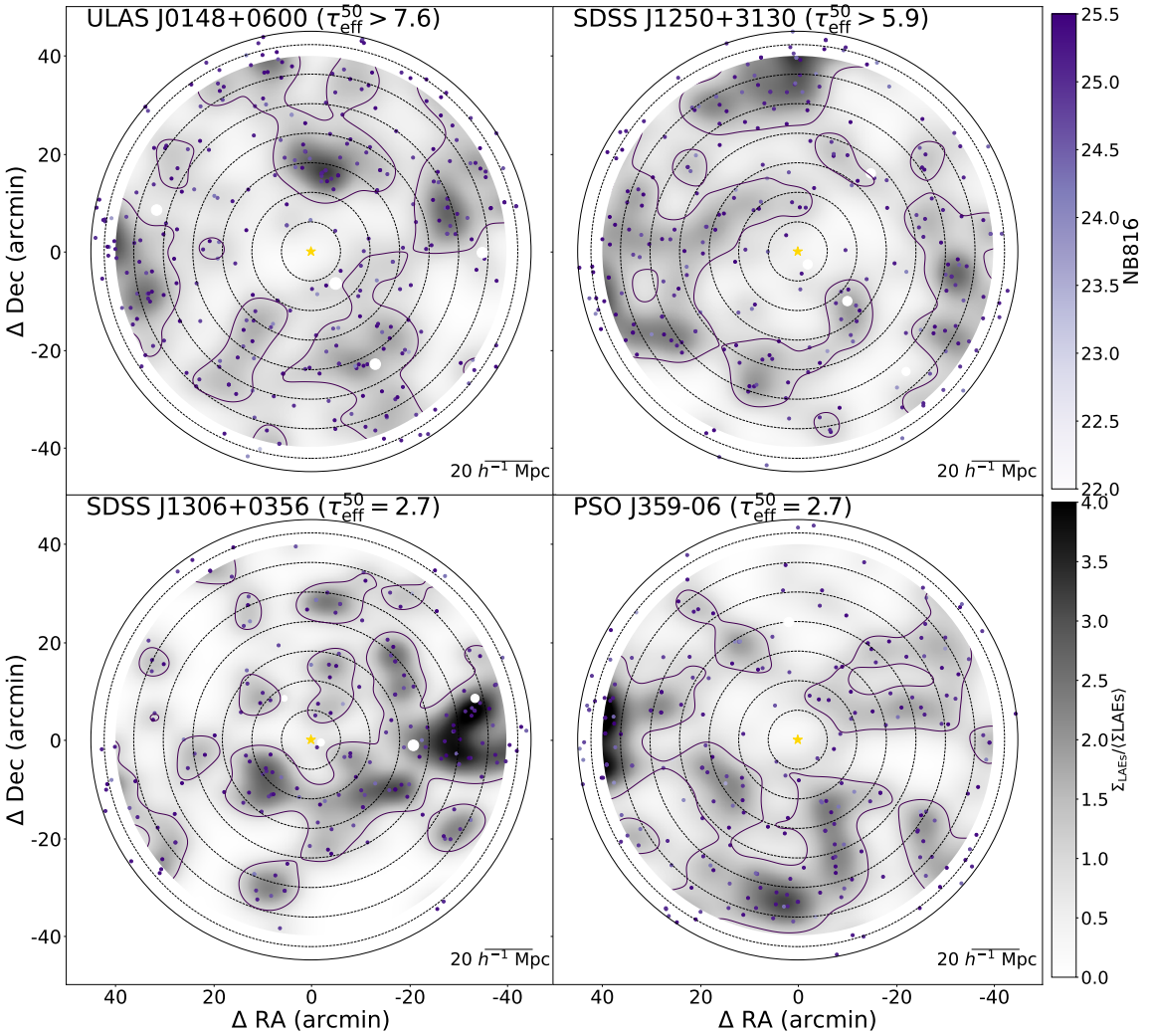

Figure 3.6 Distribution of LAE candidates in all four fields: J0148 (top left), J1250 (top right), J1306 (bottom left), and J359 (bottom right). The LAE candidates are assigned a color that indicates their $NB816$ magnitude. The grayscale shading in the background indicates the surface density of LAE candidates, which we calculate by kernel density estimation and normalized by the mean surface density of each field, measured over $15' \leq \Delta\theta \leq 40'$. This surface density is corrected for spatial variations in completeness as described in Section 3.4.3. The field is centered on the quasar position, which is marked with a gold star, and the concentric dotted rings indicate 10 h^{-1} Mpc intervals from the quasar position. The solid ring marks the edge of the field, $45'$ from the quasar position. Portions masked out of the field in white are obscured by foreground stars.

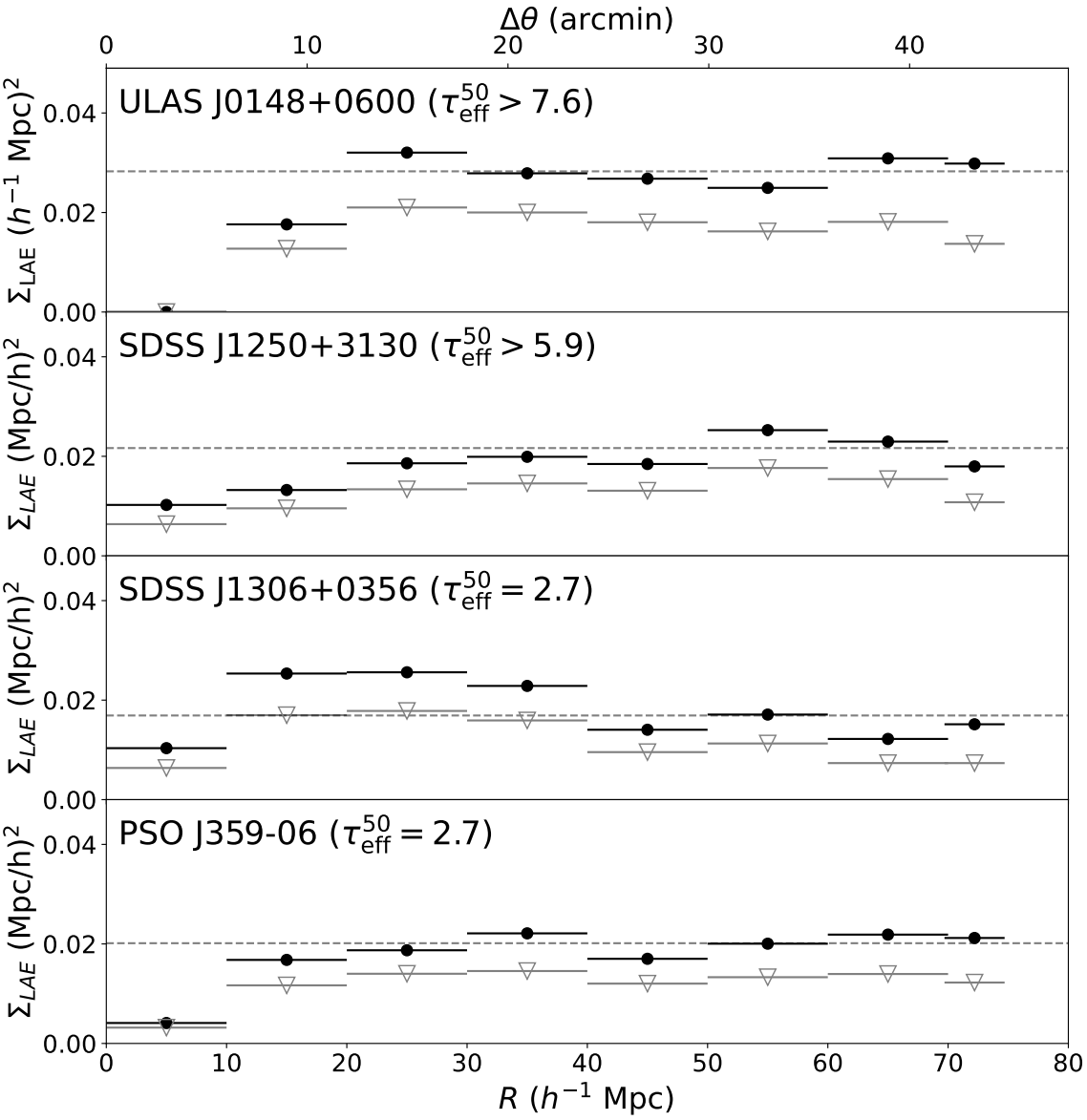

Figure 3.7 Surface density of LAE candidates in all four fields (from top to bottom: J0148, J1250, J1306, J359) as a function of their distance from the quasar position, measured in 10 h^{-1} Mpc annular bins. The unfilled gray triangles indicate raw surface density measurements, and the filled black circles indicate completeness-corrected measurements. The dotted line represents the mean completeness-corrected surface density in the field measured over $15' \leq \Delta\theta \leq 40'$. The horizontal error bars indicate the width of the annulus.

measurements in each annular bin for the four fields are summarized in Table 3.5.

We find that all four fields in the survey are underdense within $\sim 10\ h^{-1}$ Mpc of the quasar sightline; all except the J1306 field are also underdense out to $20\ h^{-1}$ Mpc. The J1306 field is mildly overdense between 10 and $20\ h^{-1}$ Mpc. This re-selection of LAEs in the J0148 and J1250 fields based on aperture photometry is consistent with our previous selections in Christenson et al. (2021) (J0148 and J1250) and Becker et al. (2018) (J0148), both in the large-scale structures reflected in the LAE distribution and in the association between highly opaque sightlines and galaxy underdensities. Additionally, we newly find an association between these two transmissive sightlines and galaxy underdensities.

3.6 Analysis

3.6.1 Comparison of Radial Distributions to Model Predictions

We can compare the results of the LAE selection in these fields directly to the predictions made by various models. In this section, we consider only the four fields surveyed in this work. Other sightlines from the literature are discussed in Section 3.6.3.

We consider the three main types of models described in the introduction: fluctuating UVB, fluctuating temperature, and ultra-late reionization. Of these three types of models, we consider six variations. Two are galaxy-driven UVB models, one from Davies et al. (2018a) and another, which also includes temperature fluctuations as would be expected at the end of reionization, from Nasir & D'Aloisio (2020). A third UVB model, from Chardin et al. (2015, 2017), is quasar-driven. The fourth is a fluctuating temperature model

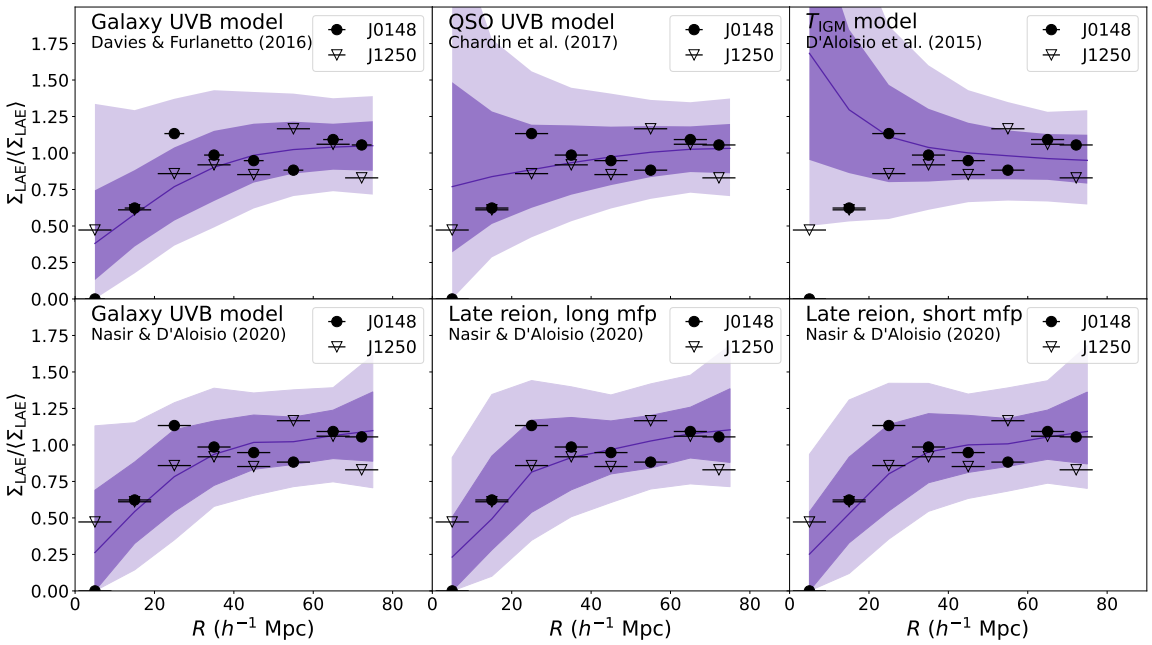

Figure 3.8 Surface density profiles for highly opaque lines of sight. Each panel compares the observed radial distribution of LAE candidates in the J0148 (filled circle) and J1250 (open triangle) fields to model predictions, where the model lines of sight have $\tau_{\rm eff}^{50} \geq 7.0$. The top row shows predictions from the galaxy UVB model based on Davies & Furlanetto (2016) (top left), the QSO UVB model based on Chardin et al. (2015, 2017) (top center), and the fluctuating temperature model from D'Aloisio et al. (2015) (top right). The bottom row shows predictions from Nasir & D'Aloisio (2020), including their galaxy UVB (early reionization) model (bottom left), late reionization model with a long mean free path (bottom center), and late reionization model with a short mean free path (bottom right). The solid lines show the median predictions for each model. The dark- and light-shaded regions show 68% and 98% ranges respectively. As in Figure 3.7, the horizontal error bars on the data points indicate the width of the bins. All surface densities are given normalized by the mean surface density in the field, measured over $15' \leq \theta \leq 40'$.

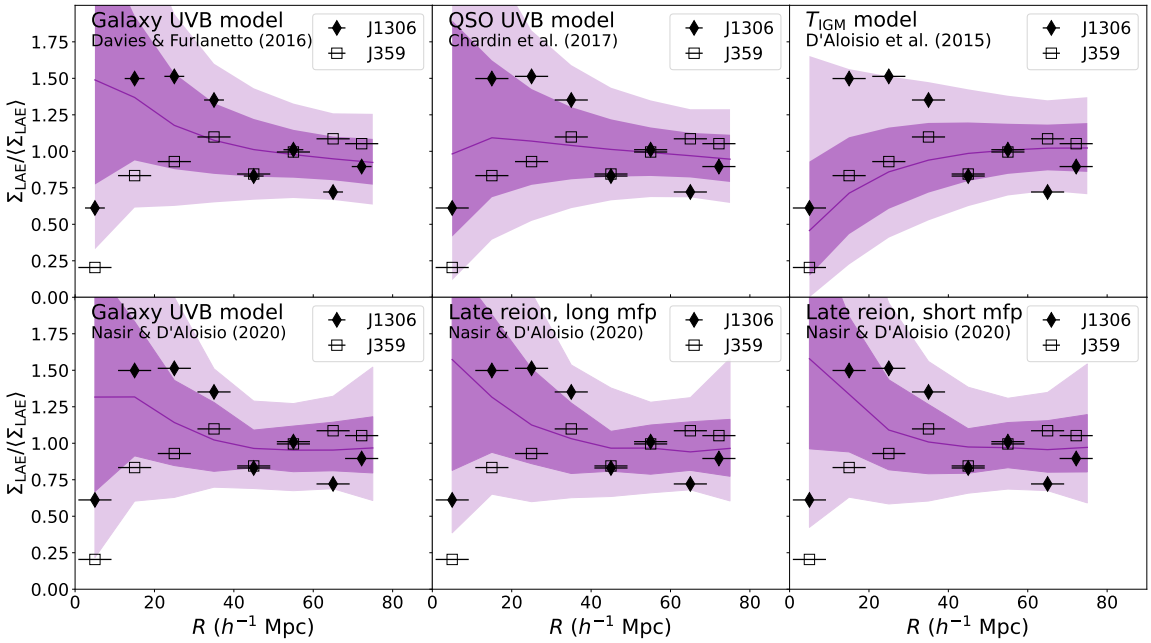

Figure 3.9 Surface density profiles for transmissive lines of sight. Each panel compares the observed radial distribution of LAE candidates in the J1306 (filled circle) and J359 (open triangle) fields to model predictions. The models are the same as in Figure 3.8, but for model lines of sight with $\tau_{\rm eff}^{50} = 2.5 \pm 0.25$. Lines, shading, and error bars are as in Figure 3.8. All surface densities are given normalized by the mean surface density in the field, measured over $15' \leq \theta \leq 40'$.

from D'Aloisio et al. (2015). Lastly, we consider two variations on an ultra-late reionization scenario from Nasir & D'Aloisio (2020). These models incorporate fluctuations in temperature and UVB as expected at the end of reionization, but allow the IGM to be $\sim 10\%$ neutral at $z = 5.5$. Of these two models, one uses a short mean free path (8 h^{-1} Mpc at z=6) and the other a long mean free path (23 h^{-1} Mpc at $z = 6$). For comparison, Becker et al. (2021) measure a mean free path of 3.57 h^{-1} Mpc at $z = 6$.

The predictions for surface density of LAEs as a function of radius are constructed from sightlines that have $\tau_{\rm eff}^{50} = 2.5 \pm 0.25$ (transmissive predictions) or $\tau_{\rm eff}^{50} \geq 7.0$ (opaque predictions). We note that the J1250 sightline has $\tau_{\rm eff}^{50} = 5.033 \pm 0.215$, which is somewhat lower than the simulated opaque sightlines used here; however, Davies et al. (2018a) find that model predictions for $\tau_{\rm eff}^{50} \geq 5.0$ are very similar (see also Figure 3.10). For each model, simulated LAE populations around these sightlines are constructed using the following basic procedure: galaxies are assigned to dark matter halos, using the measured UV luminosity of Bouwens et al. (2015) for abundance matching, and their spectra are modeled as a power-law continuum with a Lyα emission line with equivalent width set by the models of Dijkstra & Wyithe (2012). We refer the reader to Nasir & D'Aloisio (2020) and Davies et al. (2018a) for further details.

To ensure that the comparison between the modelled LAE populations and our models is as close as possible, we match the surface density of the model population to that of the observed population. First, we remove simulated LAEs from the sample in a radially- and magnitude-weighted manner using the observed completeness correction to create an incomplete catalog of simulated LAEs, comparable to the raw, uncorrected observations.

The completeness correction is scaled by a factor of ~ 0.6, so that the mean surface density of the incomplete simulated LAEs matches the uncorrected median surface density of real LAEs in our four fields. We then apply the completeness correction without the scaling factor, as done with the real LAEs, to produce a completeness-corrected simulated LAE population. From this completeness-corrected sample, we construct expected surface density profiles for highly opaque and transmissive lines of sight, which we compare to our measurements.

Figure 3.8 shows the measured surface density in the J0148 (filled circle) and J1250 (open triangle) fields as a function of radius alongside model predictions for opaque sightlines. Similarly, Figure 3.9 shows the comparison between the measured surface density in the J1306 (filled circle) and J359 (open triangle) fields as a function of radius and model predictions for transmissive sightlines. In both sets of figures, the top row shows, from left to right, predictions from the galaxy UVB model (Davies et al., 2018a), quasar UVB model (Chardin et al., 2015, 2017), and temperature model (D'Aloisio et al., 2015). The bottom row shows, from left to right, predictions from Nasir & D'Aloisio (2020) for the galaxy UVB model, the ultra-late reionization model with a long mean free path, and the ultra-late reionization model with a short mean free path. In each panel, the mean model prediction is shown with a solid line, and the shaded regions indicate the 68% and 98% ranges. All predictions and measurements measurements are normalized over the mean surface density in each field, measured over $15' \leq \theta \leq 40'$.

We find that all four sightlines are underdense within 10 h^{-1} Mpc of the quasar sightline, compared to the mean surface density of the exterior of the field. The highly opaque sightlines strongly disfavor the temperature model but are consistent with predictions from

the UVB and late reionization models, as found in Becker et al. (2018) and Christenson et al. (2021). There is some tension, however, between the transmissive sightlines and these models. The J359 sightline falls below the lower 98% threshold at $R \leq 10h^{-1}$ Mpc for all four of the galaxy UVB and late reionization models, and the J1306 model falls below the lower 68% threshold in the same ranges. This suggests that these models are unlikely to produce transmissive sightlines that are as underdense as the two we have observed. Taking all four sightlines into account, none of the models we consider here are obviously consistent with all of the data.

3.6.2 Environments of Extreme-Opacity Sightlines

A main focus of this paper is interpreting the four sightlines together, to consider what we can infer about the environments in which extreme opacity sightlines arise. The two highly opaque sightlines clearly show underdense regions within 20 h^{-1} Mpc of the quasar sightline. Similarly, the J359 sightline sits in an underdense region that is longer, but narrower, running in roughly the east-west direction. These underdense regions have a large lateral extent, spanning tens of comoving megaparsecs. The opaque troughs extend over 160 and 80 h^{-1} Mpc (J0148 and J1250 respectively), and the J359 sightline is transmissive over a 50 h^{-1} Mpc segment of the Lyα forest. We consider a region transmissive based on the absence of dark gaps ($\geq$ 30 h^{-1} Mpc in length, as defined by Zhu et al. (2021)) - or, more simply, that it is populated by transmission spikes that are measurable in extent relative to the continuum level. The lateral extent of these underdensities suggests that, were they to also extend over the full lengths of the corresponding Lyα forest features, these extreme sightlines could arise from very large structures.

The J1306 sightline arises from a region that is underdense, but adjacent to overdense regions. Approximately 45% of the area within 20 h^{-1} Mpc of the quasar sightline is estimated to be overdense (Figure 3.6), compared to 7% (J0148), 14% (J1250), and 19% (J359) for the other fields. The galaxy overdensity $\sim 30\ h^{-1}$ Mpc to the west of the J1306 sightline is particularly extensive. Given that the J1306 sightline is highly transmissive, the proximity of these potential sources of ionizing photons raises the question of whether these nearby overdense regions play a significant role in ionizing the IGM in the vicinity of the quasar sightline. The recent measurement of the mean free path at $z = 6.0$ by Becker et al. (2021) makes it possible to estimate what the mean free path should be at $z = 5.7$. Becker et al. (2021) measure $\lambda_{\rm mfp} = 9.09^{+1.62}_{-1.28}$ proper Mpc at $z = 5.1$, and $\lambda_{\rm mfp} = 0.75^{+0.65}_{-0.45}$ proper Mpc at $z = 6.0$. Linearly interpolating between these two measurements, we find that the mean free path at $z = 5.7$ should be approximately $\lambda_{\rm mfp} = 3.5$ proper Mpc, which corresponds to 16.4 h^{-1} comoving Mpc. Referring to Figure 3.6, if $\lambda_{mfp} = 16.4\ h^{-1}$ Mpc, then parts of the overdense regions in the J1306 field lie within a mean free path of the sightline. While this is a rough approximation, given that the mean free path will vary locally, it is at least plausible that these nearby overdense regions could contribute to the ionization state of the IGM in the vicinity of the quasar sightline. We also find that, for the simulated sightlines of Nasir & D'Aloisio (2020), highly transmissive, low-density sightlines are more likely to show an overdensity in adjacent radial bins in their surface density profile (similar to the J1306 field in Figure 3.7) than their higher-opacity counterparts. For example, of the sightlines in the late reionization, short mean free path model, 55% of the sightlines with $\tau_{\rm eff}^{50} \leq 3.0$ and normalized surface density ≤ 0.5 within $R \leq 10\ h^{-1}$ Mpc also had a

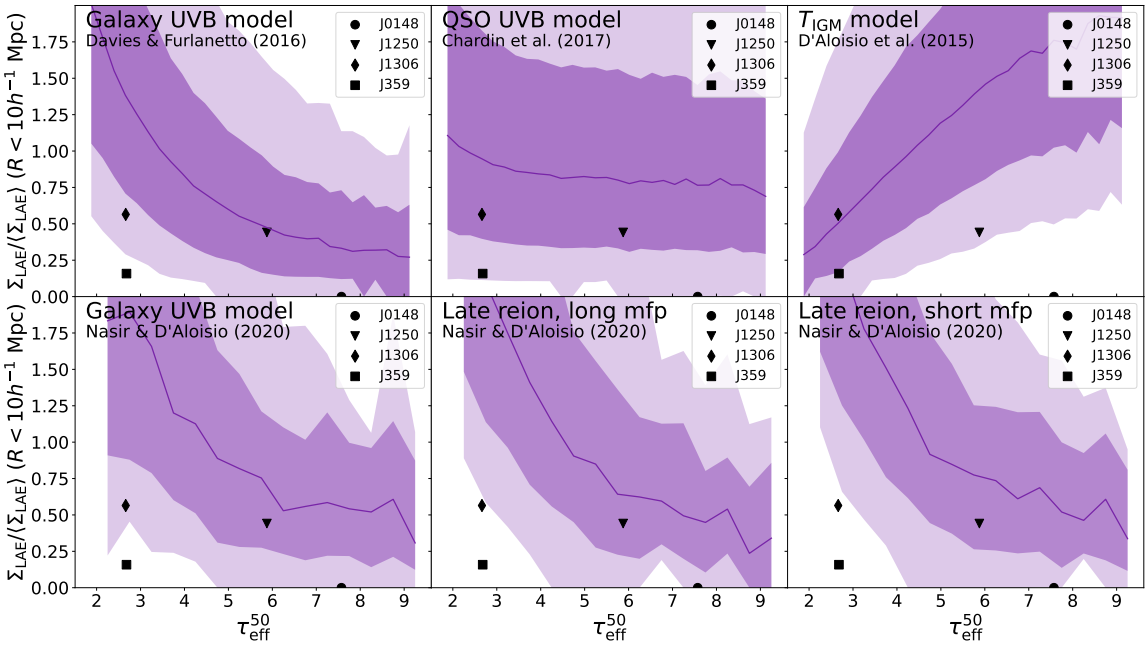

Figure 3.10 Comparison of the measured surface density of LAE candidates within 10 h^{-1} Mpc of the quasar sightline to model predictions for the relationship between opacity and LAE density. The models are the same as those in Figures 3.8 and 3.9 and predictions are made using the full set of model sightlines spanning all opacity values. All surface densities are given normalized by the mean surface density measured over $15' \leq \theta \leq 40'$ in each individual field.

normalized surface density of ≥ 1.25 over the $10 - 30$ h^{-1} Mpc region, compared to 11% of sightlines with $\tau_{\rm eff}^{50} \geq 5.0$. This trend holds for all three models of Nasir & D'Aloisio (2020), which suggests that adjacent overdensities may play a role in the high transmission of these sightlines. Thus, one possible interpretation of our observations of transmissive sightlines is that they can arise in less dense regions that are close enough to an overdensity to have an elevated ionizing background that contributes to its high transmission. This interpretation is qualitatively consistent with both the galaxy UVB and ultra-late reionization scenarios.

3.6.3 Opacity-Density Relation

Now that a number of extreme opacity QSO fields have been surveyed for LAEs, we can begin to characterize the relationship between Lyα opacity and galaxy density at $z \sim 5.7$. Figure 3.10 shows the measured surface density in the inner 10 h^{-1} Mpc of all four fields as a function of the Lyα effective opacity. Also shown are the predictions for the relationship between surface density of LAEs and Lyα opacity in each of the models. These measurements are normalized by the mean surface density in their respective fields.

The surface density measurements for transmissive sightlines put some pressure on fluctuating UVB and late reionization models, as the J359 measurement falls outside 98% range for some of the model predictions. Further, we note that all four surface density measurements lie near or below the median predictions for all models. This outcome is unlikely to occur randomly; there is only a 6.25% chance that four randomly drawn sightlines would lie below the median. The probability of reproducing our densities is as low as $< 2\%$, moreover, given that some of the measurements lie below the 68% and 98% thresholds for the different models. This emphasizes the possibility that none of the models accurately capture the relationship between opacity and density across the full $\tau_{\rm eff}$ range.

In addition to the four fields presented in this work, three additional fields have been surveyed by Ishimoto et al. (2022). Their fields have $\tau_{\rm eff}$ values measured over 50 h^{-1} Mpc of 4.17±0.25, 2.85±0.04, and 2.91±0.03, where these values are re-measured here from spectra reduced with a custom pipeline optimized for high-redshift QSOs (see Appendix F). Of these fields, the two with transmissive $\tau_{\rm eff}^{50}$ values are overdense, and the one with

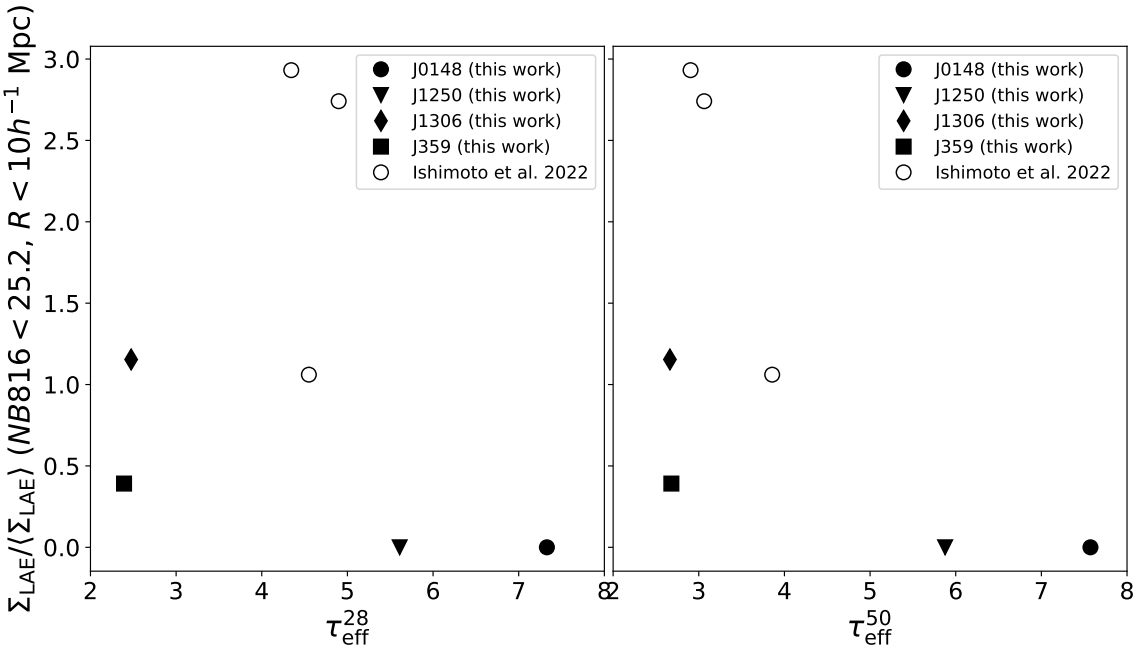

Figure 3.11 Measured surface density of LAE candidates within 10 h^{-1} Mpc of the quasar sightline as a function of $\tau_{\rm eff}^{28}$ (left) and $\tau_{\rm eff}^{50}$ (right). We include both $\tau_{\rm eff}$ windows here for comparison; for a discussion of the selection biases associated with each, see Section 3.6.3. Included are all seven fields surveyed to date, presented in this work and Ishimoto et al. (2022). For all seven fields, we match observational considerations as closely as possible, including the limiting magnitude, window of the $\tau_{\rm eff}$ measurement, and normalization. LAEs in all fields are selected down to the bright limit from Ishimoto et al. (2022) of $NB816 \leq 25.2$. Surface densities are given normalized by the mean surface density measured over $15' \leq \theta \leq 40'$ in each field.

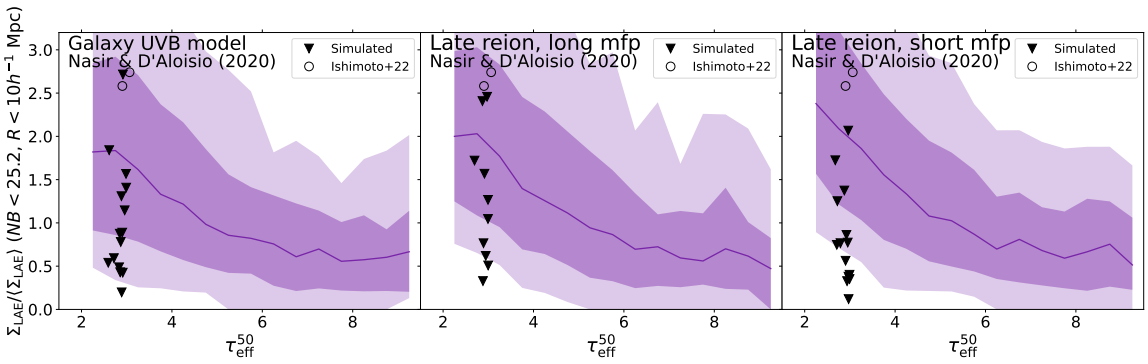

Figure 3.12 Measured surface density of LAE candidates within 10 h^{-1} Mpc of the quasar sightline as a function of $\tau_{\rm eff}^{50}$, for sightlines from Ishimoto et al. (2022) and simulated sightlines from the models of Nasir & D'Aloisio (2020). The simulated sightlines were selected to have $\tau_{\rm eff}^{28} \geq 4.0$ and $\tau_{\rm eff}^{50} \leq 3.0$, similar to the two overdense sightlines of Ishimoto et al. (2022). The model predictions are made using $\tau_{\rm eff}^{50}$ values, and all surface densities are given normalized by the mean surface density measured over $15' \leq \theta \leq 40'$ in each individual field. This figure illustrates that although these two lines of sight fall in the upper density range for their $\tau_{\rm eff}^{50}$ values, they are not consistent with simulated lines of sight from these models that were selected in the same way.

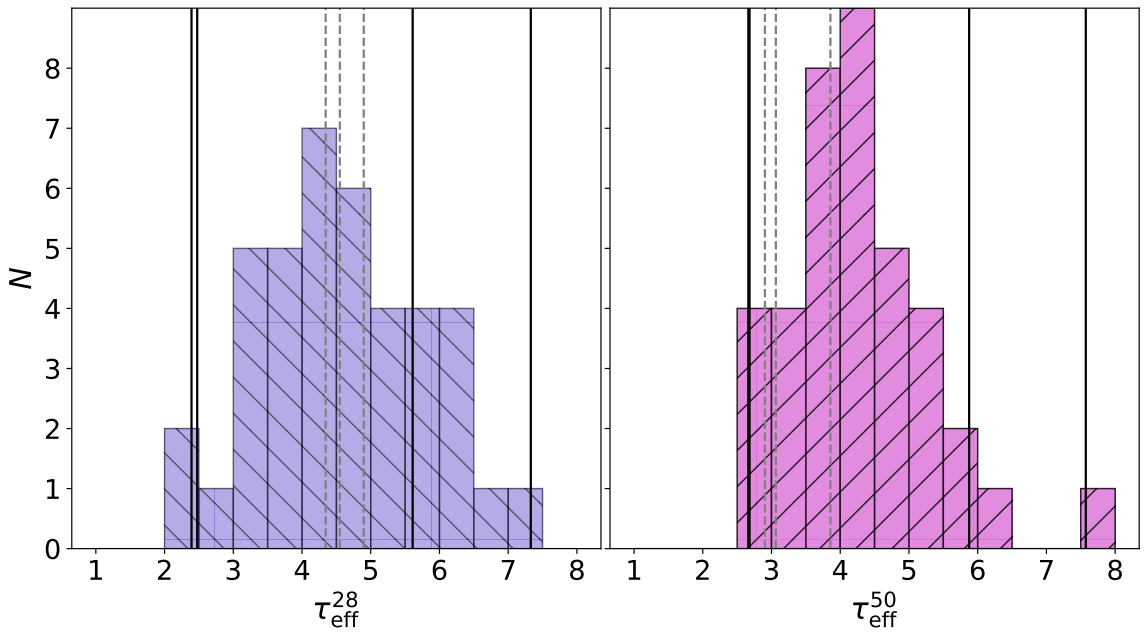

Figure 3.13 Distribution of $\tau_{\rm eff}$ measurements for the quasar sample from Zhu et al. (2021), measured both over 28 h^{-1} Mpc (left) and 50 h^{-1} Mpc (right). We show where the sightlines from this work and Ishimoto et al. (2022) fall in the distribution with solid black and dashed gray vertical lines, respectively. The sightlines from this work all fall in the wings of the global distribution, whereas the sightlines from Ishimoto et al. (2022) are more moderate.

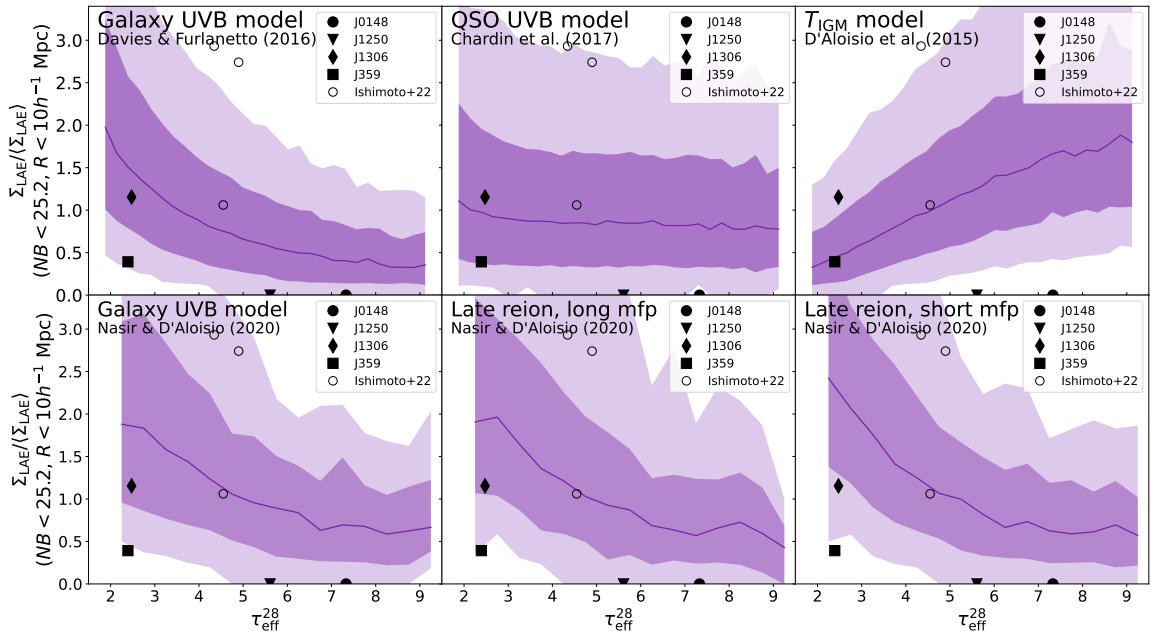

Figure 3.14 Comparison of the measured surface density of LAE candidates within 10 h^{-1} Mpc of the quasar sightline to model predictions for the relationship between opacity and LAE density. The models are the same as those used in Figures 3.8, 3.9, and 3.10. Both observations and model predictions use opacity measurements made over 28 h^{-1} Mpc and the $NB816 \leq 25.2$ magnitude limit of Ishimoto et al. (2022). All surface densities are given normalized by the mean surface density measured over $15' \leq \theta \leq 40'$ in each individual field.

moderate $\tau_{\rm eff}^{50}$ is underdense in the vicinity of the quasar sightline. The $\tau_{\rm eff}$ values for all seven fields are summarized in Table 3.3.1.

In Figure 3.11, we show the surface density in the inner 10 h^{-1} Mpc of all seven quasar sightlines as a function of their $\tau_{\rm eff}^{28}$ (left panel) and $\tau_{\rm eff}^{50}$ (right panel). We use the bright limit from Ishimoto et al. (2022) of $NB816 \leq 25.2$ for all fields. The surface density measurement in each field is normalized by the mean surface density in that field, measured over $15' \leq \theta \leq 40'$, as is done elsewhere in this work.

In principle, the seven combined fields from this work and Ishimoto et al. (2022) present an opportunity to evaluate the opacity-density relation with greater sampling of the $\tau_{\rm eff}$ distribution. At face value, low-$\tau_{\rm eff}$ lines of sight with high densities would support the fluctuating UVB and late reionization models. In practice, however, directly comparing these fields presents challenges; in addition to field-to-field variations in depth and seeing, the two sets of sightlines were selected in different manners. Our two highly opaque sightlines, J0148 and J1250, were selected based on the presence of long Lyα troughs of 110 h^{-1} and 81 h^{-1} Mpc respectively. The J1306 and J359 sightlines were selected based on their $\tau_{\rm eff}^{50}$ values, although the J1306 sightline was known to be transmissive over a longer segment of the Lyα forest (e.g., Becker et al. 2015). In contrast, Ishimoto et al. (2022) selected their fields based on Lyα forest opacities over the wavelength range of the NB816 filter, which corresponds to $\sim$28 h^{-1} Mpc. For a comparison of the $\tau_{\rm eff}$ measurements over 28 and 50 h^{-1} Mpc windows, see Table 1. Our sightlines have similar $\tau_{\rm eff}$ values over these windows. Two of the three sightlines from Ishimoto et al. (2022), however, show significant differences in their 28 or 50 h^{-1} Mpc opacities. In these cases, the forest is highly opaque over the

28 h^{-1} Mpc window but shows strong transmission just outside it, giving a lower 50 h^{-1} Mpc opacity. Because the sightlines from Ishimoto et al. (2022) were selected to be opaque over 28 h^{-1} Mpc, they may not be representative of all sightlines with low $\tau_{\rm eff}^{50}$. Figure 3.11 illustrates the strong impact that the $\tau_{\rm eff}$ measurement window has on the results.

To understand the biases associated with selecting sightlines over the $NB816$ window, we investigated similar sightlines in the fluctuating UVB and late reionization models from Nasir & D'Aloisio (2020). We selected sightlines with $\tau_{\rm eff}^{28} \geq 4.0$ and $\tau_{\rm eff}^{50} \leq 3.0$, similar to the sightlines from Ishimoto et al. (2022). Of the 4000 simulated sightlines for each model, there are $10-15$ sightlines that meet these criteria. Similar to the real sightlines, the simulated ones uniformly show a strongly absorbed dark gap over the $NB816$ filter range, and strong transmission spikes over the remainder of the 50 h^{-1} Mpc window. The densities of these sightlines sample the full range of density scatter shown in model predictions for density as a function of $\tau_{\rm eff}^{28}$. However, they are not representative of the density distribution for sightlines that are transmissive over 50 h^{-1} Mpc. Figure 3.12 shows the surface density of these simulated sightlines and the sightlines observed by Ishimoto et al. (2022) compared to model predictions made over 50 h^{-1} Mpc. Simulated sightlines that are selected to be opaque over 28 h^{-1} Mpc are biased towards being underdense for their 50 h^{-1} Mpc opacities. The two Ishimoto et al. (2022) sightlines with these opacity characteristics are denser than any of the simulated sightlines that were selected in the same manner. These sightlines are therefore also not obviously consistent with either the UVB or late reionization models.

We suggest that the $\tau_{\rm eff}^{28}$ window may be least impacted by selection effects because it reflects the selection criteria of Ishimoto et al. (2022) and because the $\tau_{\rm eff}$ measurements

for the sightlines presented in this work are fairly consistent over both windows. At the limit of $NB816 < 25.5$ used in Figure 3.11, highly opaque sightlines (on scales of 28 h^{-1} Mpc) are correlated with galaxy underdensities, while the transmissive sightlines are mildly over- or underdense. Sightlines with moderate opacity, meanwhile, show a large scatter in observed density. Overall, three of the seven sightlines surveyed are underdense within 10 h^{-1} Mpc of the quasar sightline and two are of average density. Although the overall sample tends towards lower densities, we note that most of these sightlines are not typical in terms of their $\tau_{\rm eff}$ values. Figure 3.13 shows the distribution of $\tau_{\rm eff}$ values for the quasar sample of Zhu et al. (2021) measured over both 28 (left) and 50 (right) h^{-1} Mpc windows. The opacity values for the sightlines discussed in this work are marked with vertical lines. The four sightlines presented in this work, which are mostly underdense, fall at the extreme ends of the distribution. The sightlines from Ishimoto et al. (2022), which show a range of densities, fall in the center of the global distribution and are likely to be more representative of the majority of quasar sightlines at this redshift.

Figure 3.14 shows the surface density within 10 h^{-1} Mpc of the quasar sightline as a function of $\tau_{\rm eff}^{28}$ for all sightlines from this work and Ishimoto et al. (2022), compared to predictions from the models of Nasir & D'Aloisio (2020). Both the data and models use $\tau_{\rm eff}^{28}$ opacity measurements and the $NB816 \leq 25.2$ magnitude limit of Ishimoto et al. (2022). We use $\tau_{\rm eff}^{28}$ values for this model comparison because they may be less impacted by selection effects than $\tau_{\rm eff}^{50}$ values, as discussed above.

Altogether, these observations are not clearly consistent with any of the models considered here. The association of highly opaque sightlines and galaxy underdensities is

explained well by fluctuating UVB and late reionization models, but these models do not obviously work well for the transmissive sightlines. On the other hand, the temperature model is in good agreement with the transmissive sightlines.

We can speculate on what may be happening at the low-opacity end. In a post-reionization IGM with a more homogeneous UVB, we expect that opacity will positively correlate with density. This correlation may even be enhanced by temperature fluctuations for some period following reionization, as in the fluctuating temperature model. A homogeneous UVB is not expected at $z = 5.7$; indeed, there is strong observational evidence for UVB fluctuations persisting as late as $z \sim 5.3$ (Becker et al., 2015; Bosman et al., 2018; Eilers et al., 2018; Yang et al., 2020; Bosman et al., 2021; Zhu et al., 2021). If the UVB is not as highly suppressed in underdense regions as the models considered here suggest, however, then these regions may quickly transition from being highly opaque to being transmissive once they are fully reionized, an evolution first suggested by Keating et al. (2020b).

A caveat of this work is the assumption that LAEs are a good tracer of the underlying density field, an assumption that is complicated near the end of reionization by how susceptible Lyα photons are to attenuation by neutral gas. Davies et al. (2018a) found that LAE surveys were $\sim$90% likely to distinguish between fluctuating UVB and temperature models. However, there is some observational evidence, albeit at lower redshift, that LAEs either avoid some high-density peaks (Francis & Bland-Hawthorn, 2004; Kashikawa et al., 2007; Huang et al., 2022), or tend to prefer lower-density regions (Cooke et al., 2013), possibly because higher-density regions have a stronger UVB that suppresses star formation (Kashikawa et al., 2007; Bruns et al., 2012). Kashino et al. (2020) surveyed Lyman break

galaxies (LBGs) in the J0148 field and found an underdensity in the vicinity of the quasar sightline, which indicates that the J0148 underdensity is not the result of Lyα suppression by neutral gas. However, it is unclear whether LBGs and LAEs in this field trace the same large scale structures, in part due to the broader redshift range spanned by the LBG selection ($\Delta z \sim 0.4$). It is also unclear whether a survey of LBGs in a field surrounding a transmissive sightline would similarly show the same density profile as the LAE population. A promising avenue for future work is therefore to consider other types of galaxy surveys to corroborate the results of the LAE selections. In addition to LBGs, sub-mm sureys, which probe massive, obscured galaxies, may be a useful probe of the density at these redshifts; Li et al. (2023) recently surveyed sub-mm galaxies in the J0148 field and reported an overdensity, although without redshifts it is unclear whether they are in proximity to the Lyα trough. It is also now possible to select galaxies at these redshifts based on their [OIII]$\lambda\lambda$4960,5008 emission with JWST/NIRCam, as done by the EIGER team (Kashino et al., 2022).

3.7 Summary

We present an initial characterization of the relationship between IGM Lyα opacity and galaxy density at $z = 5.7$ by surveying Lyman-α emitting galaxies in the fields surrounding quasar sightlines with extreme values of Lyα opacity. The relationship between IGM opacity and galaxy density on large ($\gtrsim 10\ h^{-1}$ Mpc) transverse scales serves as a test of reionization models that predict the observed scatter in Lyα opacity. Surveying sightlines over a wide range of Lyα opacity, particularly extreme values, is necessary to characterize this relationship. We present two new surveys of LAEs towards the $z = 6.02$ quasar SDSS

J1306+0356 and the $z = 6.17$ quasar PSO J359-06, whose sightlines show very low effective Lyα opacity over 50 h^{-1} Mpc along the line of sight ($\tau_{\rm eff}^{50} = 2.6$ and $\tau_{\rm eff}^{50} = 2.7$ for the J1306 and J359 fields respectively). We also re-select LAEs in the fields surrounding two highly opaque sightlines, towards ULAS J0148+0600 and SDSS J1250+3130, using the aperture photometry adopted for this work.

We report an underdensity of LAEs within 10 h^{-1} Mpc of both transmissive quasar sightlines. The results towards highly opaque sightlines are unchanged from previous works (Becker et al., 2018; Christenson et al., 2021); we find strong underdensities in the vicinity of both quasar sightlines. We note that the underdensities associated with Lyα troughs span greater lateral extent than those associated with transmissive sightlines ($\gtrsim 20$ h^{-1} Mpc; see Section 3.6.2). We compare the measured surface density as a function of radius to predictions made by three broad types of models in Figure 3.9: fluctuating UVB models (Davies et al., 2018a; Nasir & D'Aloisio, 2020; Chardin et al., 2015, 2017), fluctuating temperature models (D'Aloisio et al., 2015), and ultra-late reionization models (Nasir & D'Aloisio (2020), see also Kulkarni et al. (2019b); Keating et al. (2020a)). The correlation between highly opaque sightlines and galaxy underdensities strongly disfavors the temperature model, and the fluctuating UVB and late reionization models are unlikely to produce transmissive sightlines as underdense as those we observe. None of the models, on their own, cleanly predict our observations of all four sightlines.

Our measurements allow us to begin characterizing the observed LAE surface density as a function of Lyα effective opacity (see Figure 3.10). The highly transmissive sightlines are sufficiently underdense within 10 h^{-1} Mpc of the quasar sightline to be challenging

for galaxy-driven UVB and ultra-late reionization models, which favor overdense regions associated with transmissive sightlines. Further, all of our observations fall below the median model predictions for the opacity-density relation, which hints that the models may not fully capture the physical conditions leading to sightlines with extreme opacity.

A total of seven fields surrounding quasar sightlines have now been surveyed in this manner. We show the LAE surface density as a function of Lyα effective opacity of our four fields together with three from Ishimoto et al. (2022) (Figure 3.11). While the sightlines with extreme opacity are correlated to galaxy underdensities within 10 h^{-1} Mpc of the quasar sightline, the sightlines of moderate opacity range from median density to significantly overdense. The association of highly opaque sightlines with galaxy underdensities is well-predicted by fluctuating UVB and late reionization models. The association of highly transmissive sightlines with galaxy underdensities, however, is in possible tension with these models. One possible interpretation of these observations is that as reionization ends, the UVB transitions to a more homogeneous state more quickly than in the models considered here, causing the hot, recently reionized voids to rapidly become highly transmissive. This evolution in the transmission of the voids was first suggested by Keating et al. (2020b).

Further galaxy surveys, particularly towards transmissive sightlines, are needed for a more robust characterization of the relationship between opacity and density. If these further observations confirm the correlation between transmissive sightlines and galaxy underdensities, it would indicate that current reionization models do not adequately capture the ionizing sources and/or the sinks near the end of reionization.

Chapter 4

Conclusions

We have combined complementary observations of Lyα emitting galaxies (LAEs) and quasar spectra to better understand the intergalactic medium (IGM) at the end of reionization. This study is motivated by the presence of strong fluctuations in the Lyα opacity of quasar sightlines at $z < 6$, which is unexpected in an ionized IGM with a homogeneous ionizing ultraviolet background (UVB). These regions of extreme opacity therefore present an opportunity to potentially study the end stages of reionization, as the galaxy density associated with these extreme opacities can provide insight into the underlying physical conditions that drive the opacity fluctuations.

We present the results of surveys for LAEs in the fields surrounding four such extreme quasar sightlines. We find that highly opaque quasar sightlines are correlated to extensive galaxy underdensities ($\gtrsim$20 h^{-1} Mpc in radius). These results are consistent both with a scenario in which reionization is ongoing at $z = 5.7$, later than previously believed, and with a scenario where large-scale fluctuations in the UVB are driving the observed

opacity fluctuations. We also find that highly transmissive quasar sightlines are correlated with galaxy underdensities, albeit ones that tend to have a lesser lateral extent ($\sim$10 h^{-1} Mpc in radius). These observations are in some tension with model predictions; all four of our measured densities lie below the median model predictions for all of the models we consider, which has a <6.25% chance of occurring randomly. In particular, the transmissive sightlines sometimes lie below the 68% and 98% thresholds for these models.

There are two main challenges facing our results to date. The first is that we have only begun to characterize the relationship between Lyα opacity and galaxy density. With only four sightlines, it is difficult to be sure whether these observations are representative of the general opacity-density relationship. Further, most sightlines surveyed to date represent extreme Lyα opacities. These sightlines in this work were selected because the models can be most easily distinguished from each other at extreme opacities, but they aren't representative of the global opacity distribution. Observations of moderate-opacity sightlines are needed to fully characterize the opacity-density relationship.

The need for further surveys brings us to the second challenge for this project. In this work we have used LAEs to characterize galaxy density. LAEs are an appealing proxy for density because they can be surveyed over wide areas using relatively inexpensive photometry, and theoretical analysis suggested that they should be able to robustly distinguish between different models of reionization (Davies et al., 2018a). However, if LAEs do not trace the underlying density field as well as we have assumed, it could contribute to the unexpected results near transmissive sightlines. Lyman alpha emission is often produced by high rates of star formation, which typically occurs in low-mass halos. There is some

evidence at lower redshifts that LAEs don't trace some high-density regions well (Francis & Bland-Hawthorn, 2004; Kashikawa et al., 2007; Huang et al., 2022; Cooke et al., 2013). This may happen because those regions have an elevated UVB, which would delay star formation by heating the interstellar medium via photoionization and therefore suppress Lyα emission, particularly in the small halos that typically host LAEs (Kashikawa et al., 2007; Bruns et al., 2012). Ruling out the possibility that LAEs do not trace strong overdensities well at higher redshifts would strengthen our results.

Moving forward, complementary surveys of galaxies may help us to better understand the density in these regions of extreme opacity and confirm the results of LAE surveys. For example, Lyman break galaxies (LBGs) can also be selected over wide areas using photometry, although more data is required than for LAE selection. LBGs are often associated with more massive halos hosting galaxies that have already formed a large stellar population, and are therefore bright enough to be detected based on their continuum emission. The dropout technique used to select LBGs covers a broader redshift range than the narrowband filters used to select LAEs. Accurately determining photometric redshifts is challenging, so it is more difficult to know whether they are truly correlated with interesting IGM Lyα features. Sub-mm galaxies, which trace high-mass, obscured galaxies, are another option, but similarly suffer from difficulty placing the sources in redshift space. Lastly, the advent of JWST makes it possible to select galaxies based on their OIII emission lines, which will provide precise spectroscopic redshifts. The downside of this approach is that it is relatively expensive and difficult to carry out over the larger regions we use in this work, but it is nevertheless a promising avenue to constrain the density field in the vicinity of

quasar sightlines.

Despite these challenges, the observations that we have made to date are intriguing. The high-opacity sightlines are consistent with both fluctuating UVB and late reionization models. On the other hand, the observed behavior in the low-opacity regime is unexpected in the fluctuating UVB and late reionization models. Even if these two transmissive sightlines turn out to be atypical, they suggest that the models may not yet accurately reproduce the environments of transmissive sightlines. This tension presents an opportunity to better understand the physics of the IGM, and we can offer some speculation about what conditions might lead to transmissive sightlines. In a post-reionization IGM, where the UVB is homogeneous, we expect that opacity and density will be correlated; this relationship is well-documented at lower redshifts. However, a homogeneous UVB is not expected at redshifts near the end of reionization. Evidence suggests that UVB fluctuations persist as late as z=5.3 (Becker et al., 2015; Bosman et al., 2018; Eilers et al., 2018; Yang et al., 2020; Bosman et al., 2021; Zhu et al., 2021). The late reionization models that we consider in this work therefore also include fluctuations in the UVB. We speculate that, if the UVB is less suppressed in underdense regions than the models suggest, underdense regions may transition rapidly from being opaque to transmissive as they are reionized, as first suggested by Keating et al. (2020b). Such an evolution in the opacity of underdense regions may explain the observed correlation between galaxy underdensities and transmissive sightlines. If future observations confirm the results of this work, it will provide valuable insight into the physical state of the IGM at these redshifts, including which conditions are not captured well in current reionization models.

Looking forward, we stand to learn a great deal about the sources of reionization in the relatively near future with a variety of upcoming tools. *JWST* is expected to advance our understanding of star formation at high redshift. 21-cm observations, which trace neutral hydrogen in the reionization epoch, are forecasted to place strong constraints on the topology of reionization, the nature of ionizing sources, and the midpoint of reionization. The correlation between the sources of reionization and their environments, however, is still a fairly new area of research, and this work is one of only a few that have attempted to directly connect source and IGM properties to date. In the future, a more detailed understanding of the relationship between source and environment properties will provide new insight into the physics of the IGM and therefore how reionization proceeds and ends.

Bibliography

Abazajian, K., Adelman-McCarthy, J. K., Agüeros, M. A., et al. 2004, The Astronomical Journal, 128, 502 2.4.1

Astropy Collaboration, Robitaille, T. P., Tollerud, E. J., et al. 2013, Astronomy and Astrophysics, 558, A33

Bañados, E., Venemans, B. P., Mazzucchelli, C., et al. 2018, Nature Astronomy, 553, 473 2.2, 3.2

Becker, G. D., Bolton, J. S., Madau, P., et al. 2015, Monthly Notices of the Royal Astronomical Society, 447, 3402 (document), 2.2, 2.1, 2.3, 3.2, 3.3.1, 3.6.3, 4, A

Becker, G. D., D'Aloisio, A., Christenson, H. M., et al. 2021, Monthly Notices of the Royal Astronomical Society, 508, 1853 3.6.1, 3.6.2

Becker, G. D., Davies, F. B., Furlanetto, S. R., et al. 2018, The Astrophysical Journal, 863, 92 (document), 2.2, 2.3, 2.4.1, 2.4.2, 2.5, 2.5, 2.6.1, 2.7, 3.2, 3.3.2, 3.4.1, 3.5, 3.6.1, 3.7, A, B.1, B.1, B.2, B.4, B.2, C, C, C.1, C, C.1, C.2, E

Becker, G. D., Pettini, M., Rafelski, M., et al. 2019, The Astrophysical Journal, 883, 163 (document), 3.1, 3.3.1, F, F.1

Bertin, E., & Arnouts, S. 1996, Astronomy and Astrophysicss, 117, 393 2.3, 3.3.2

Boera, E., Becker, G. D., Bolton, J. S., & Nasir, F. 2019, The Astrophysical Journal, 872, 101 3.2

Bosch, J., Armstrong, R., Bickerton, S., et al. 2018, Publications of the Astronomical Society of Japan, 70, S5 2.4.1

Bosman, S. E. I., Fan, X., Jiang, L., et al. 2018, Monthly Notices of the Royal Astronomical Society, 479, 1055 2.2, 3.2, 3.6.3, 4

Bosman, S. E. I., Davies, F. B., Becker, G. D., et al. 2021, arXiv e-prints, arXiv:2108.03699

2.2, 3.2, 3.6.3, 4

Bouwens, R. J., Illingworth, G. D., Oesch, P. A., et al. 2015, The Astrophysical Journal, 803, 34 2.6.1, 3.6.1

Bruns, L. R., Wyithe, J. S. B., Bland-Hawthorn, J., & Dijkstra, M. 2012, Monthly Notices of the Royal Astronomical Society, 421, 2543 3.6.3, 4

Chambers, K. C., Magnier, E. A., Metcalfe, N., et al. 2016, arXiv e-prints, arXiv:1612.05560 2.3, 3.3.2

Chardin, J., Haehnelt, M. G., Aubert, D., & Puchwein, E. 2015, Monthly Notices of the Royal Astronomical Society, 453, 2943 (document), 2.2, 2.6.1, 2.6, 2.7, 3.2, 3.6.1, 3.8, 3.7

Chardin, J., Puchwein, E., & Haehnelt, M. G. 2017, Monthly Notices of the Royal Astronomical Society, 465, 3429 (document), 2.2, 2.6.1, 2.6, 2.7, 3.2, 3.6.1, 3.8, 3.7

Choudhury, T. R., Paranjape, A., & Bosman, S. E. I. 2021, Monthly Notices of the Royal Astronomical Society, 501, 5782 2.2, 2.7

Christenson, H. M., Becker, G. D., Furlanetto, S. R., et al. 2021, The Astrophysical Journal, 923, 87 (document), 3.2, 3.3.2, 3.4.1, 3.4.2, 3.5, 3.5, 3.6.1, 3.7, E, H, H.1

Cooke, J., Omori, Y., & Ryan-Weber, E. V. 2013, Monthly Notices of the Royal Astronomical Society, 433, 2122 3.6.3, 4

D'Aloisio, A., McQuinn, M., Davies, F. B., & Furlanetto, S. R. 2018, Monthly Notices of the Royal Astronomical Society, 473, 560 2.2, 2.7

D'Aloisio, A., McQuinn, M., & Trac, H. 2015, The Astrophysical Journal Letters, 813, L38 (document), 2.2, 2.6, 2.6.1, 2.7, 3.2, 3.8, 3.6.1, 3.7

D'Aloisio, A., Upton Sanderbeck, P. R., McQuinn, M., Trac, H., & Shapiro, P. R. 2017, Monthly Notices of the Royal Astronomical Society, 468, 4691 2.2, 3.2

Davies, F. B., Becker, G. D., & Furlanetto, S. R. 2018a, The Astrophysical Journal, 860, 155 2.2, 2.6.1, 2.7, 3.6.1, 3.6.3, 3.7, 4

Davies, F. B., & Furlanetto, S. R. 2016, Monthly Notices of the Royal Astronomical Society, 460, 1328 (document), 2.2, 2.6.1, 2.6, 2.7, 3.2, 3.8

Davies, F. B., Hennawi, J. F., Bañados, E., et al. 2018b, The Astrophysical Journal, 864, 142 2.2, 3.2

Díaz, C. G., Koyama, Y., Ryan-Weber, E. V., et al. 2014, Monthly Notices of the Royal Astronomical Society, 442, 946 2.4.2

Dijkstra, M., & Wyithe, J. S. B. 2012, Monthly Notices of the Royal Astronomical Society, 419, 3181 2.6.1, 3.6.1

Eilers, A.-C., Davies, F. B., & Hennawi, J. F. 2018, The Astrophysical Journal, 864, 53 2.2, 3.2, 3.3.1, 3.6.3, 4

Faber, S. M., Phillips, A. C., Kibrick, R. I., et al. 2003, 4841, 1657 B.1

Faisst, A. L., Chary, R. R., Fajardo-Acosta, S., et al. 2022, The Astrophysical Journal, 929, 66 3.2

Fan, X., Strauss, M. A., Becker, R. H., et al. 2006, The Astronomical Journal, 132, 117 2.2, 3.2

Francis, P. J., & Bland-Hawthorn, J. 2004, Monthly Notices of the Royal Astronomical Society, 353, 301 3.6.3, 4

Gaikwad, P., Rauch, M., Haehnelt, M. G., et al. 2020, Monthly Notices of the Royal Astronomical Society, 494, 5091 3.2

Gangolli, N., D'Aloisio, A., Nasir, F., & Zheng, Z. 2021, Monthly Notices of the Royal Astronomical Society, 501, 5294 2.5

Garaldi, E., Compostella, M., & Porciani, C. 2019, Monthly Notices of the Royal Astronomical Society, 483, 5301 2.2, 3.2

Greig, B., Mesinger, A., & Bañados, E. 2019, Monthly Notices of the Royal Astronomical Society, 484, 5094 2.2, 3.2

Greig, B., Mesinger, A., Haiman, Z., & Simcoe, R. A. 2017, Monthly Notices of the Royal Astronomical Society, 466, 4239 2.2, 3.2

Huang, Y., Lee, K.-S., Cucciati, O., et al. 2022, The Astrophysical Journal, 941, 134 3.6.3, 4

Hunter, J. D. 2007, Computing in Science & Engineering, 9, 90

Ishimoto, R., Kashikawa, N., Kashino, D., et al. 2022, Monthly Notices of the Royal Astronomical Society, 515, 5914 (document), 3.2, 3.1, 3.6.3, 3.11, 3.12, 3.13, 3.14, 3.7, F, F.1, F.1

Ivezić, v., Tyson, J. A., Acosta, E., et al. 2008, arXiv:0805.2366v4 2.3, 3.3.2

Jung, I., Finkelstein, S. L., Dickinson, M., et al. 2020, The Astrophysical Journal, 904, 144 2.2, 3.2

Jurić, M., Kantor, J., Lim, K., et al. 2015, ArXiv e-prints, arXiv:1512.07914 2.3, 3.3.2

Kakiichi, K., Ellis, R. S., Laporte, N., et al. 2018, Monthly Notices of the Royal Astronomical Society, 479, 43

Kashikawa, N., Kitayama, T., Doi, M., et al. 2007, The Astrophysical Journal, 663, 765 3.6.3, 4

Kashino, D., Lilly, S., Matthee, J., et al. 2022, EIGER I. a large sample of [OIII]-emitting galaxies at $5.3 < z < 6.9$ and direct evidence for local reionization by galaxies, doi:10.48550/arXiv.2211.08254 3.6.3

Kashino, D., Lilly, S. J., Shibuya, T., Ouchi, M., & Kashikawa, N. 2020, The Astrophysical Journal, 888, 6 2.2, 3.2, 3.6.3

Keating, L. C., Kulkarni, G., Haehnelt, M. G., Chardin, J., & Aubert, D. 2020a, Monthly Notices of the Royal Astronomical Society, 497, 906 2.2, 2.7, 3.2, 3.7

Keating, L. C., Weinberger, L. H., Kulkarni, G., et al. 2020b, Monthly Notices of the Royal Astronomical Society, 491, 1736 2.2, 2.6.1, 2.7, 3.2, 3.6.3, 3.7, 4

Kelson, D. D. 2003, Publications of the Astronomical Society of the Pacific, 115, 688 B.1

Khostovan, A. A., Sobral, D., Mobasher, B., et al. 2019, Monthly Notices of the Royal Astronomical Society, 489, 555 2.5

Konno, A., Ouchi, M., Shibuya, T., et al. 2017, Publications of the Astronomical Society of Japan, 70, s16 (document), 2.4.2, 3.5

Kulkarni, G., Keating, L. C., Haehnelt, M. G., et al. 2019a, Monthly Notices of the Royal Astronomical Society, 485, L24 2.2, 2.7

Kulkarni, G., Worseck, G., & Hennawi, J. F. 2019b, Monthly Notices of the Royal Astronomical Society, 488, 1035 2.6.1, 3.2, 3.7

Li, Q., Wang, R., Fan, X., et al. 2023, arXiv e-prints, arXiv:2304.04719 3.6.3

Lidz, A., Oh, S. P., & Furlanetto, S. R. 2006, The Astrophysical Journal Letters, 639, L47

2.2, 3.2

López, S., D'Odorico, V., Ellison, S. L., et al. 2016, Astronomy and Astrophysics, 594, A91 F

Mason, C. A., Treu, T., Dijkstra, M., et al. 2018, The Astrophysical Journal, 856, 2 2.2, 3.2

McGreer, I. D., Fan, X., Jiang, L., & Cai, Z. 2018, The Astronomical Journal, 155, 131 2.2, 2.6.1, 3.2

McGreer, I. D., Mesinger, A., & D'Odorico, V. 2015, Monthly Notices of the Royal Astronomical Society, 447, 499 2.2

McGreer, I. D., Mesinger, A., & Fan, X. 2011, Monthly Notices of the Royal Astronomical Society, 415, 3237 2.2

Meyer, R. A., Kakiichi, K., Bosman, S. E. I., et al. 2020, Monthly Notices of the Royal Astronomical Society, 494, 1560

Morales, A., Mason, C., Bruton, S., et al. 2021, arXiv e-prints, arXiv:2101.01205 2.2, 3.2

Mortlock, D. J., Warren, S. J., Venemans, B. P., et al. 2011, Nature Astronomy, 474, 616 2.2, 3.2

Nasir, F., & D'Aloisio, A. 2020, Monthly Notices of the Royal Astronomical Society, 494, 3080 (document), 2.2, 2.6.1, 2.6, 2.7, 3.2, 3.6.1, 3.8, 3.6.2, 3.12, 3.6.3, 3.7

Ono, Y., Ouchi, M., Harikane, Y., et al. 2018, Publications of the Astronomical Society of Japan, 70, S10

Ouchi, M., Shimasaku, K., Akiyama, M., et al. 2008, The Astrophysical Journals, 176, 301 (document), 2.4.2, 3.4.2, 3.5

Ouchi, M., Harikane, Y., Shibuya, T., et al. 2018, Publications of the Astronomical Society of Japan, 70, S13 2.4.2, 2.5

Parsa, S., Dunlop, J. S., & McLure, R. J. 2018, Monthly Notices of the Royal Astronomical Society, 474, 2904 2.6.1

Planck Collaboration, Adam, R., Aghanim, N., et al. 2016, Astronomy and Astrophysics, 596, A108

Planck Collaboration, Aghanim, N., Akrami, Y., et al. 2020, A&A, 641, A6 2.2, 3.2

Price-Whelan, A. M., Sipőcz, B. M., Günther, H. M., et al. 2018, The Astronomical Journal, 156, 123

Prochaska, J. 2017, Astronomy and Computing, 19, 27 (document), F, F.1

Qin, Y., Mesinger, A., Bosman, S. E. I., & Viel, M. 2021, arXiv e-prints, arXiv:2101.09033 2.2, 2.7

Robertson, B. E., Ellis, R. S., Furlanetto, S. R., & Dunlop, J. S. 2015, The Astrophysical Journal Letters, 802, L19

Sheinis, A. I., Bolte, M., Epps, H. W., et al. 2002, Publications of the Astronomical Society of the Pacific, 114, 851

Shibuya, T., Ouchi, M., Harikane, Y., et al. 2017, Publications of the Astronomical Society of Japan, 70, doi:10.1093/pasj/psx107, s15

Shibuya, T., Ouchi, M., Konno, A., et al. 2018a, Publications of the Astronomical Society of Japan, 70, S14 2.4.2

—. 2018b, Publications of the Astronomical Society of Japan, 70, S14

Stark, D. P., Ellis, R. S., Chiu, K., Ouchi, M., & Bunker, A. 2010, Monthly Notices of the Royal Astronomical Society, 408, 1628 2.5

Trac, H., Cen, R., & Mansfield, P. 2015, The Astrophysical Journal, 813, 54 2.5

Tramonte, D., Rubiño-Martín, J. A., Betancort-Rijo, J., & Dalla Vecchia, C. 2017, Monthly Notices of the Royal Astronomical Society, 467, 3424 2.5

Trapp, A. C., & Furlanetto, S. R. 2020, Monthly Notices of the Royal Astronomical Society, 499, 2401 2.5

van der Walt, S., Colbert, S. C., & Varoquaux, G. 2011, Computing in Science Engineering, 13, 22

Vernet, J., Dekker, H., D'Odorico, S., et al. 2011, Astronomy and Astrophysics, 536, A105

Virtanen, P., Gommers, R., Oliphant, T. E., et al. 2020, Nature Methods, 17, 261

Wang, F., Davies, F. B., Yang, J., et al. 2020, The Astrophysical Journal, 896, 23 2.2, 3.2

Wise, J. H. 2019, arXiv e-prints, arXiv:1907.06653 2.2, 3.2

Yang, J., Wang, F., Fan, X., et al. 2020, The Astrophysical Journal, 904, 26 2.2, 3.2, 3.6.3, 4

Zhu, Y., Becker, G. D., Bosman, S. E. I., et al. 2021, arXiv:2109.06295 (document), 2.1, 2.3, 3.2, 3.3.1, 3.6.2, 3.13, 3.6.3, 4, A, F, F.1

Zhu, Y., Becker, G. D., Bosman, S. E. I., et al. 2022, The Astrophysical Journal, 932, 76 (document), 3.2, F, F.1

Appendix A

Lyα Opacity of Quasar Sightlines

As done by Becker et al. (2018), we use our imaging data to estimate $\tau_{\rm eff}$ along both quasar lines of sight using the PSF photometry described in chapter 2.4.1. The purpose of these measurements is to check whether our data are consistent with existing spectroscopic limits for these sightlines, and whether it's possible to improve on the existing limits given the depth of our data. For each quasar, we first measure the $NB816$ and $i2$ fluxes. We then convolve each object's spectrum with the $i2$ transmission curve, and scale the spectrum so that its transmission-weighted mean flux over the $i2$ band matches what was measured in the imaging We use the scaled spectrum to estimate the unabsorbed continuum flux at the narrowband wavelength, and then from the continuum estimate and the photometric narrow-band flux we calculate the effective opacity as $\tau_{\rm eff} = -\ln(\mathrm{F}_\lambda^{\rm NB816}/\mathrm{F}_\lambda^{\rm cont})$. These measurements represent an effective opacity over the $NB816$ wavelength region, which is overlapped by but considerably shorter than the spectroscopically measured regions of both troughs.

In the J0148 sightline, we measure $F_\lambda^{NB816} = (2.0 \pm 1.8) \times 10^{-20}$ erg s^{-1} cm^{-2} Å^{-1} and $F_\lambda^{i2} = (3.2 \pm 0.5) \times 10^{-18}$ erg s^{-1} cm^{-2} Å^{-1}, and estimate that the unabsorbed continuum is $F_\lambda^{\rm cont} = 1.5 \times 10^{17}$ erg s^{-1} cm^{-2} Å^{-1}. We therefore measure $\tau_{\rm eff} = 6.63^{+2.5}_{-0.65}(1\sigma)$, or a 2σ lower limit of $\tau_{\rm eff} \geq 5.59$, which is consistent with the 2σ lower limit measured by Becker et al. (2015) of $\tau_{\rm eff} \geq 7.2$ measured over a 50 h^{-1} Mpc chapter centered at z=5.726.

The J1250 quasar is not detected in our $NB816$ data. As a rough estimate, we adopt the 2σ upper limit, $F_\lambda^{NB816} \leq 4.0 \times 10^{-20}$ erg s^{-1} cm^{-2} Å^{-1}. We also measure $F_\lambda^{i2} = (7.3 \pm 0.2) \times 10^{-19}$ erg s^{-1} cm^{-2} Å^{-1}, and estimate that the unabsorbed continuum is $F_\lambda^{\rm cont} = 1.0 \times 10^{17}$ erg s^{-1} cm^{-2} Å^{-1}. We therefore measure $\tau_{\rm eff} \geq 5.52^{+0.69}_{-0.41}(1\sigma)$, or a 2σ lower limit of $\tau_{\rm eff} \geq 4.83$. This measurement is consistent with that of Zhu et al. (2021), who find that $\tau_{\rm eff} = 5.7 \pm 0.4$ measured over 81 h^{-1} Mpc centered at z=5.760.

Appendix B

Spectroscopic Followup of J0148 LAEs with Keck/DEIMOS

B.1 Observations

In addition to the imaging data discussed in Section 2.3, we obtained spectra of 46 LAE candidates in the J0148 field taken with the DEIMOS spectrograph (Faber et al., 2003) on the Keck II telescope in November 2018. Targets were selected from the catalog of LAE candidates published in Becker et al. (2018), as spectroscopic followup was carried out prior to the creation of the catalog presented in this work. We prioritized objects in the underdense region at the center of the field of view, a second low-density region at the west edge of the field, and a high-density region. In total we used 5 masks, which we designed using DSIMULATOR (Figure B.1). The observations, which are summarized in

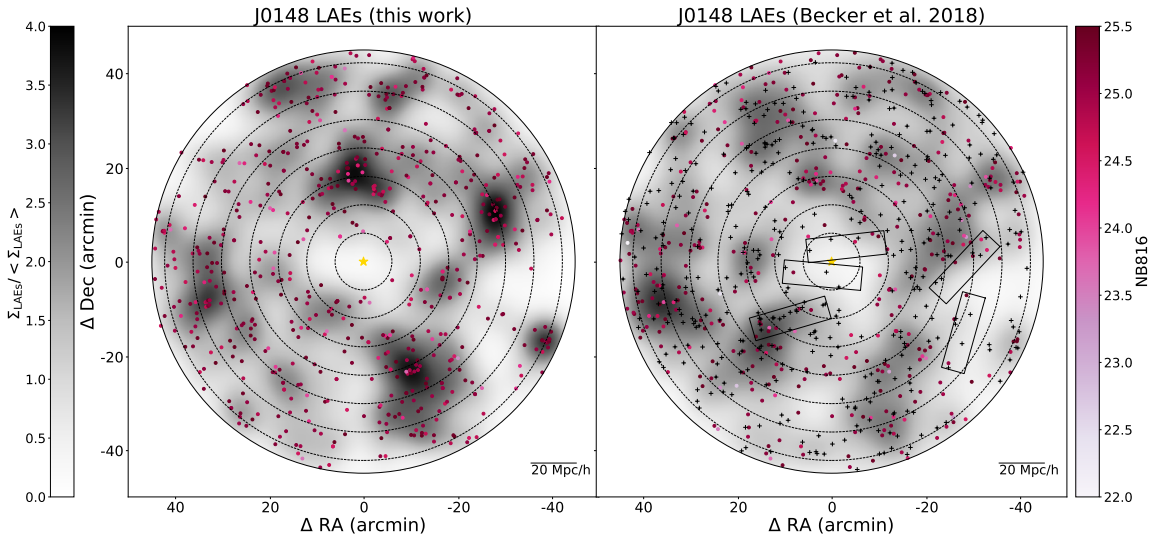

Figure B.1 Distribution of LAE candidates in the J0148 field as selected in this work (left) and by Becker et al. (2018) (right). Each field is shown centered on the quasar (gold star). LAE candidates with NB816<25.5 are shown with a color that indicates their narrowband magnitude in their respective catalog. In the right panel, LAEs selected in Becker et al. (2018) with $NB816 > 25.5$ (fainter than our selection limit) are shown with black crosses. The surface density at each position is calculated by kernel density estimation using a Gaussian kernel, and is normalized by the mean surface density measured across the entire field. Concentric, dotted circles are shown in increments of 10 Mpc h^{-1} projected distance from the quasar. The black rectangles in the right panel indicate the pointings of DEIMOS slitmasks used for spectroscopic followup. The solid circle marks the edge of the field of view, $45'$ from the quasar.

Table B.1 Summary of Keck/DEIMOS observations

Date	Mask[a]	Description	t_{exp} (h)	Seeing[b] ($''$)
11/28/18	1	Central	2	0.74
11/28/18	2	Central	2	0.73
11/29/18	3	High Density	2	0.83
11/29/18	4	High Density	2	0.65
11/28-11/29	5	Low Density	1.2	0.78

[a] The first priority for mask placement was to maximize the number of LAE candidates observed within 20 h^{-1} Mpc of the quasar. Masks were also placed to cover other high- and low-density regions of the field.

[b] Median seeing measured from Gaussian fits to the profiles of stars on each mask.

Table B.1, were made in multi-slit mode using the OG550 filter and the 600-line grating. Each individual target was placed in a $1''$ slit, and all slits were tilted five degrees relative to the position angle of the mask in order to better sample the sky lines for sky subtraction.

We reduced the raw spectra with a custom IDL pipeline that includes optimal sky subtraction (Kelson, 2003). Individual exposures were then combined onto a two-dimensional grid rectified with nearest neighbor resampling, in which each frame's individual pixels are assigned to the pixel in the combined frame that it most closely matches in position and wavelength. Rectifying the spectra in this way ensures that pixels in the combined frame remains uncorrelated. Finally, we corrected the spectra for atmospheric absorption, and flux calibrated using standard stars.

B.2 Results

Emission lines were identified by visual inspection of the 2D spectra. To be spectroscopically confirmed, a LAE candidate was required to have a single emission line in the Lyα region, and no emission lines elsewhere in the trace. For each spectroscopically confirmed LAE, we determine the spectroscopic redshift from the flux-weighted mean wavelength of the emission line, which is calculated over a 20 Å window centered on the visually estimated line center. This window was chosen to be wide enough to cover any of the emission lines in our sample, but not so wide as to include unwanted skyline noise. We also measure the Lyα flux by integrating the spectrum over a wavelength region that includes the entire emission line; this region is customized for each object, but is typically ~ 15 Å. Table B.2 summarizes

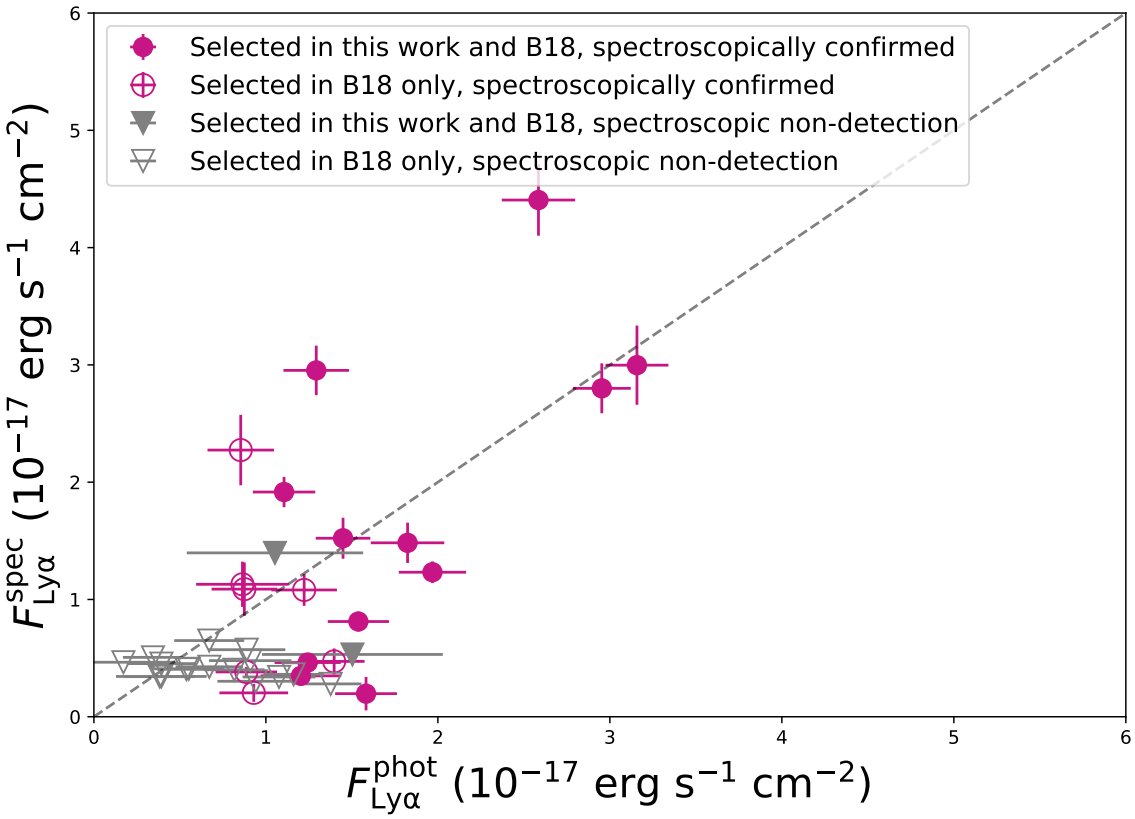

Figure B.2 Photometric and spectroscopic fluxes for all credible LAE candidates. The following objects are considered credible: all spectroscopically confirmed objects, spectroscopic non-detections that were selected photometrically in this work, and non-detections that were selected only by Becker et al. (2018) that also passed a secondary visual inspection to remove clearly spurious sources. Spectroscopically confirmed LAEs are shown with circles, and spectroscopic non-detections are shown with triangles. LAEs that meet the photometric criteria outlined in 2.4.2 are shown with filled markers; LAEs that fail one or more photometric criteria are shown with empty markers. For spectroscopic non-detections, the reported flux is a 1σ upper limit.

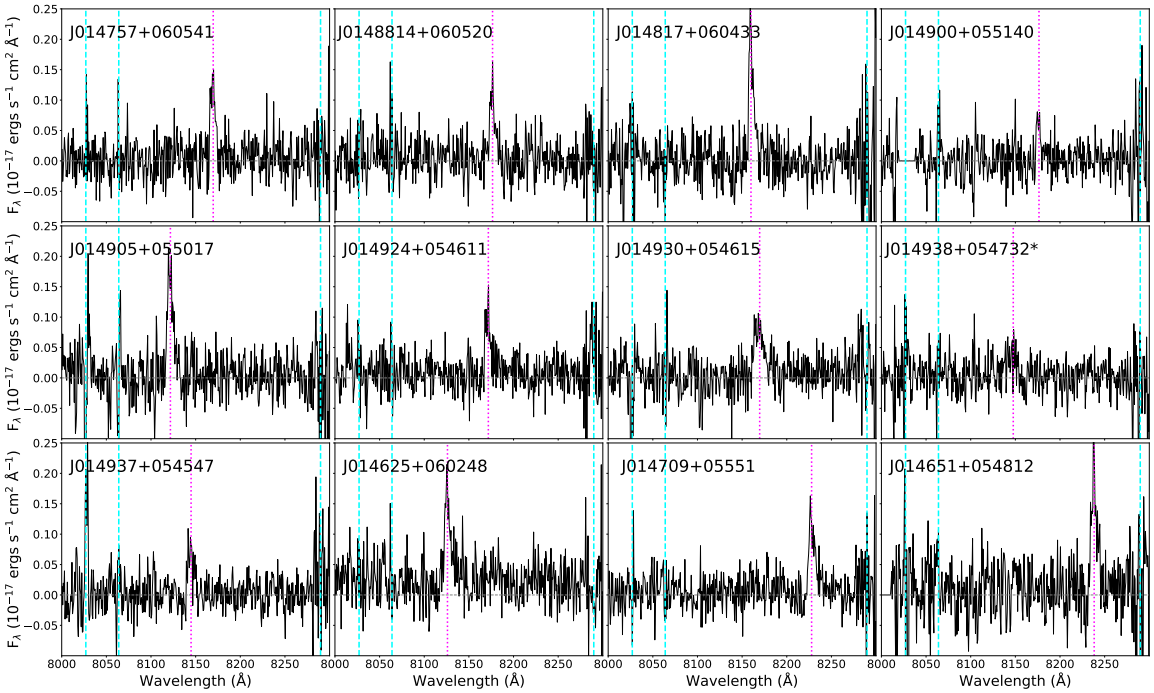

Figure B.3 Spectra for each of the spectroscopically confirmed LAEs that meet the photometric criteria outlined in 2.4.2. The dashed cyan lines indicate skyline residuals, while the dotted pink line indicates the flux-weighted mean wavelength of the emission line, which is used to calculate the spectroscopic redshift. J0149938+054732 (marked with an asterisk) is a marginal detection with 1.4σ confidence.

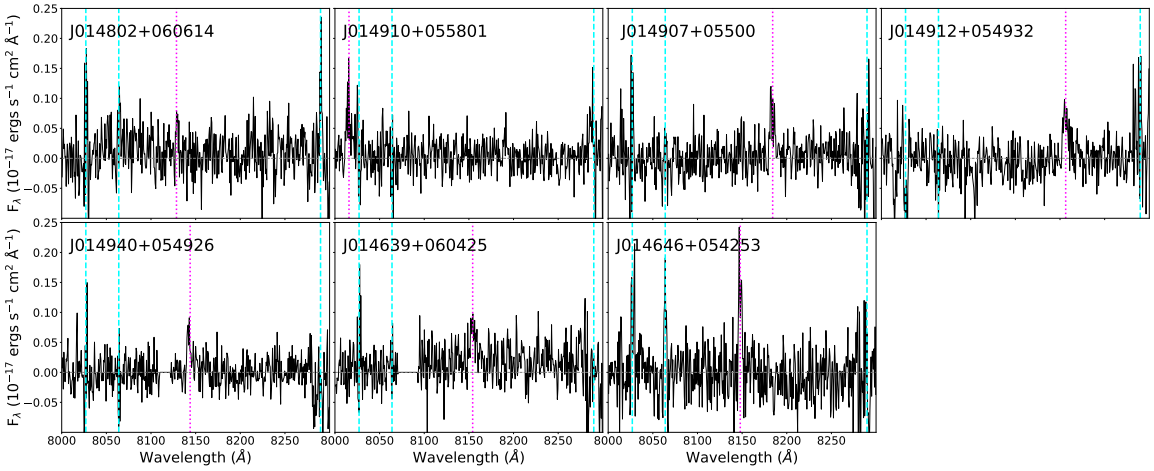

Figure B.4 Spectra for each of the spectroscopically confirmed LAEs that were selected in Becker et al. (2018) but were not selected by the photometric criteria outlined in 2.4.2. The dashed cyan lines indicate skyline residuals and the dotted pink line indicates the flux-weighted mean wavelength of the emission line, which is used to calculate the spectroscopic redshift.

Table B.2 Summary of spectroscopically confirmed LAEs in the J0148 field

ID	z_{spec}	m^a_{NB816}	$F^b_{phot} \cdot 10^{17}$	$F^b_{spec} \cdot 10^{17}$	Selected?[c]
J014757+060541	5.72	25.12	1.54 ± 0.18	0.81 ± 0.08	Y
J014802+060614	5.69	25.67	0.93 ± 0.2	0.2 ± 0.08	N
J0148814+060520	5.73	25.19	1.45 ± 0.16	1.52 ± 0.17	Y
J014817+060433	5.71	24.42	2.95 ± 0.17	2.8 ± 0.21	Y
J014910+055801	5.59	25.23	1.4 ± 0.18	0.47 ± 0.11	N
J014900+055140	5.73	25.39	1.2 ± 0.23	0.35 ± 0.07	Y
J014905+055017	5.68	24.56	2.58 ± 0.21	4.41 ± 0.3	Y
J014907+05500	5.73	25.75	0.86 ± 0.27	1.13 ± 0.19	N
J014912+054932	5.75	25.37	1.22 ± 0.19	1.08 ± 0.14	N
J014924+054611	5.72	24.94	1.82 ± 0.21	1.48 ± 0.17	Y
J014930+054615	5.72	24.34	3.16 ± 0.18	3.0 ± 0.34	Y
J014940+054926	5.70	25.72	0.89 ± 0.18	0.38 ± 0.04	N
J014938+054732[d]	5.70	25.09	1.58 ± 0.18	0.2 ± 0.14	Y
J014937+054547	5.70	25.36	1.24 ± 0.19	0.46 ± 0.05	Y
J014625+060248	5.69	24.86	1.97 ± 0.2	1.23 ± 0.09	Y
J014639+060425	5.71	25.76	0.85 ± 0.19	2.27 ± 0.3	N
J014709+05551	5.77	25.48	1.11 ± 0.18	1.92 ± 0.13	Y
J014651+054812	5.78	25.31	1.29 ± 0.19	2.95 ± 0.21	Y
J014646+054253	5.70	25.74	0.87 ± 0.19	1.09 ± 0.23	N

[a] Photometric measurement

[b] Measured in ergs s^{-1} cm^{-2} $Å^{-1}$

[c] Indicates whether this object met the updated selection criteria described in Section 2.4.

[d] Marginal detection

the properties of all spectroscopically confirmed LAEs. We compare the photometric and spectroscopic Lyα fluxes for all credible LAEs in Figure B.2, which includes spectroscopically confirmed objects, spectroscopic non-detections that were selected photometrically in this work, and non-detections that were selected only by Becker et al. (2018) that also passed a secondary visual inspection to remove clearly spurious sources. Figure B.2 demonstrates a reasonable agreement between the photometric and spectroscopic measurements, including for the spectroscopic non-detections, which tend to be the faintest objects in the sample.

Among the 46 LAE candidates from Becker et al. (2018) targeted for spectroscopic follow-up, 14 were also selected as LAEs in this work using the updated PSF photometry and the new LAE selection criteria. Of those 14, 11 were spectroscopically confirmed at $\geq 4\sigma$ confidence, and one was marginally detected at 1.4σ. Figure B.3 shows 1D spectra for these PSF-selected LAEs. The dashed cyan lines indicate skyline residuals, and the dotted pink line line indicates the flux-weighted mean wavelength of the emission line.

The remaining 32 objects targeted for spectroscopic followup were selected as LAEs only by Becker et al. (2018). Of these, seven are spectroscopically confirmed LAEs, and their 1D spectra are shown in Figure B.4. These seven fell just outside our new selection criteria using the updated PSF photometry; four had narrowband $4.5 < S/N < 5$, and one had $S/N = 3.2$. The remaining two are detected in the $r2$ band at 2.3σ, which is slightly higher than our $r2$ cuts allow. The other 25 objects failed our updated selection criteria by wider margins. Their spectroscopic non-detections are attributed to the issues with CModel fluxes described in Section 2.4.1, with the exception of one object, which was a low-redshift contaminant displaying a clear [OIII] emission line.

In summary, we find a high spectroscopic confirmation rate (11 plus one marginal detection out of 14) among candidates selected using our updated photometry and selection criteria. The two non-detected objects of the photometrically selected group were generally fainter than their detected counterparts, with a 1σ upper limit on their flux being consistent with the photometric measurement, and showed no sign of being low-redshift contaminants. We note that all of the objects followed up spectroscopically were also selected as LAEs by Becker et al. (2018), so these 14 candidates do not represent an unbiased random sample from the new photometric catalog. Nevertheless, the high confirmation rate among the PSF-selected candidates gives us confidence that the photometric selection methods described in Section 2.4.2 should yield a high-fidelity sample of LAEs.

Appendix C

Comparison to Becker et al. (2018) LAE catalog

Here we compare the LAE catalog presented in this work, using updated photometry and selection criteria as described in Sections 2.4.2 and 2.4.1, to that published in Becker et al. (2018).

In this work, we identify 641 LAE candidates in the J0148 field, compared to 806 LAEs presented in Becker et al. (2018). Of the objects selected by Becker et al. (2018), 398 had $NB816 < 25.5$ as required in this work, and 236 of those objects ($\sim$60%) are selected using the selection criteria and photometric measurements outlined in Section 2.4. We estimate that 15-20% of the objects selected by Becker et al. (2018) with $NB816 < 25.5$ were affected by the systematic CModel flux effects described in Section 2.4. We show examples of objects wrongly rejected and accepted due to these issues in Figure C.1. Each

Table C.1 Comparison of LAE selections in Becker et al. (2018) and this work

	This Work	Becker et al. (2018)
Objects selected with $NB816 \leq 26.0$	784[a]	806
Objects selected with $NB816 \leq 25.5$	641	398[b]
	Both Works	
Catalog overlap with $NB816 \leq 26.0$[c]	366	
Catalog overlap with $NB816 \leq 25.5$[d]	236	
Catalog overlap with published $NB816$ limits[e]	321	

[a] This work uses a brighter magnitude limit than Becker et al. (2018) ($NB816 \leq 25.5$). The number of objects selected with the fainter limit is included only for comparison.
[b] Likewise, Becker et al. (2018) use $NB816 \leq 26.0$. The subset of this catalog that satisfies the brighter magnitude limit is included here for comparison.
[c] The number of LAEs appearing in both catalogs that meet the fainter magnitude requirement. $NB816 \leq 26.0$ (as in Becker et al. 2018)
[d] The number of LAEs appearing in both catalogs that meet the brighter magnitude requirement, $NB816 \leq 25.5$ (as in this work)
[e] The number of LAEs appearing in both catalogs as is, using $NB816 \leq 25.5$ for this work and $NB816 \leq 26.0$ for Becker et al. (2018) (as published)

cutout image is $10''$ on each side and centered on the object position. The wrongly rejected object was rejected based on artificially high broadband fluxes, while the wrongly accepted object had inflated $NB816$ flux. The remaining 20-25% of the Becker et al. (2018) objects with $NB816 < 25.5$ missing from our sample are within 1σ errors of meeting our selection criteria. Given that our catalog is $\sim 50\%$ complete at the faintest magnitudes, it is not unexpected that some objects will not be selected due to photometric scattering.

Table C summarizes the number of LAEs selected in both catalogs. Because the two catalogs use different narrowband magnitude limits, $NB816 \leq 25.5$ in this work and $NB816 \leq 26.0$ in Becker et al. (2018), we provide the number of objects selected in each catalog using both limits. We emphasize that this work only makes use of $NB816 \leq 25.5$ objects for our analysis; the fainter magnitude limit is provided only for comparison. Table C also summarizes the number of LAEs that are common to both catalogs using both

magnitude limits, as well as the number of objects common to the catalogs as is (using $NB816 \leq 25.5$ for the objects selected in this work, and $NB816 \leq 26.0$ for Becker et al. (2018), as published).

Figure B.1 shows the distribution of LAE candidates in the J0148 field, as presented in this work (left) and in Becker et al. (2018) (center). Each LAE is color-coded according to the $NB816$ magnitude in its respective catalog. This work has a shallower narrowband magnitude limit than Becker et al. (2018); we have therefore shown LAEs that fall in the $25.5 \leq NB816 \leq 26.0$ bin from the Becker et al. (2018) catalog with black crosses, as they are fainter than our selection criteria allow. The quasar (yellow star) is centered in each panel, and the dotted concentric circles show increments of 10 h^{-1} Mpc. The solid outer circle marks the edge of the field of view, $45'$ from the quasar. LAE candidates are shown plotted over a surface density map, which we create by kernel density estimation over a regular grid of $0.24'$ pixels using a Gaussian kernel of bandwidth $1.6'$. The surface density map is normalized by the mean surface density of the field. While the exact membership is varied between the two catalogs, both show similar large-scale structures.

Figure C.2 shows the surface density as a function of radial distance from the quasar in the J0148 field, as measured here (circles) and by Becker et al. (2018) (triangles). The surface densities are measured in 10 h^{-1} Mpc annuli for all except the outermost bin, which is 4.5 h^{-1} Mpc, and normalized by the mean surface density, which is measured over $15' \leq \theta \leq 40'$. We note that, in addition to the changes to fluxing and LAE selection criteria, the completeness corrections used in this work (see Section 2.5) are different than those used by Becker et al. (2018). However, in most radial bins the surface density measurements are

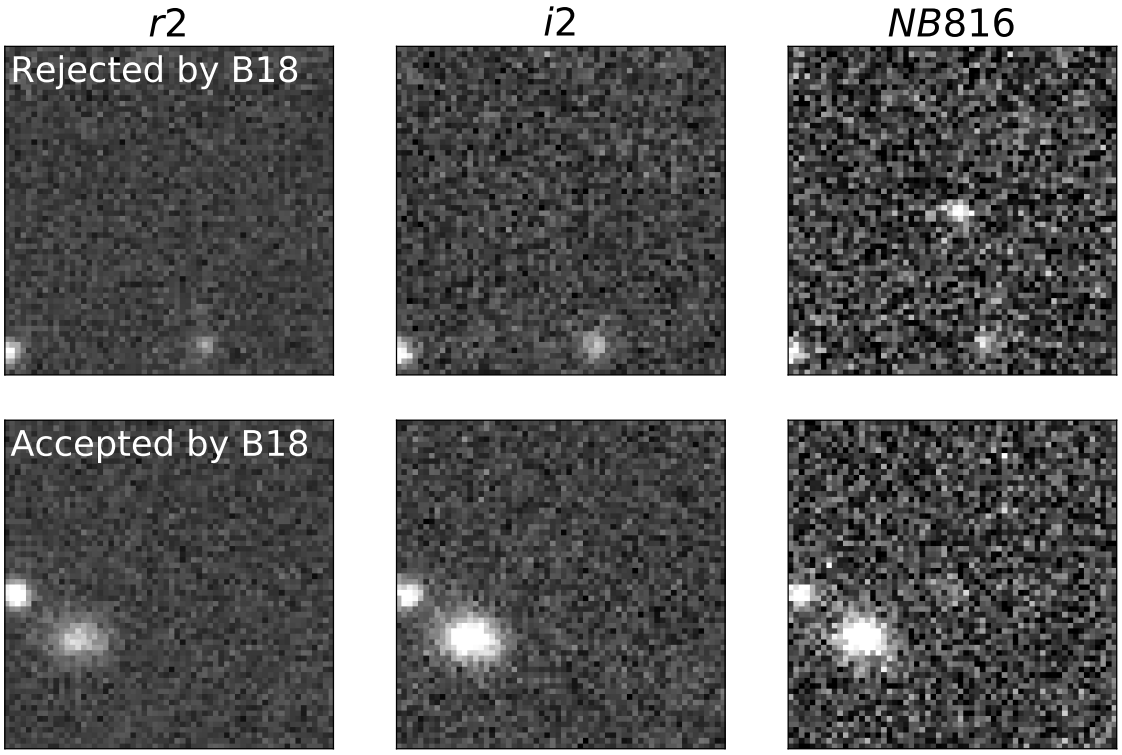

Figure C.1 Examples of objects rejected (top row) and accepted (bottom row) as LAE candidates by Becker et al. (2018) based on spurious CModel photometry. Each cutout is $10''$ on each side and centered on the object position. The rejected object is detected in the CModel photometry at 10σ in the narrowband, 18σ in $i2$, and 26σ in $r2$ - a clear case of artificially high broadband photometry. This object is selected as an LAE in this work using the photometry and selection criteria outlined in Section 2.4. The accepted object is undetected in the broadbands, but is detected using the CModel photometry at 7.5σ in the narrowband, compared to 3.0σ using our PSF photometry.

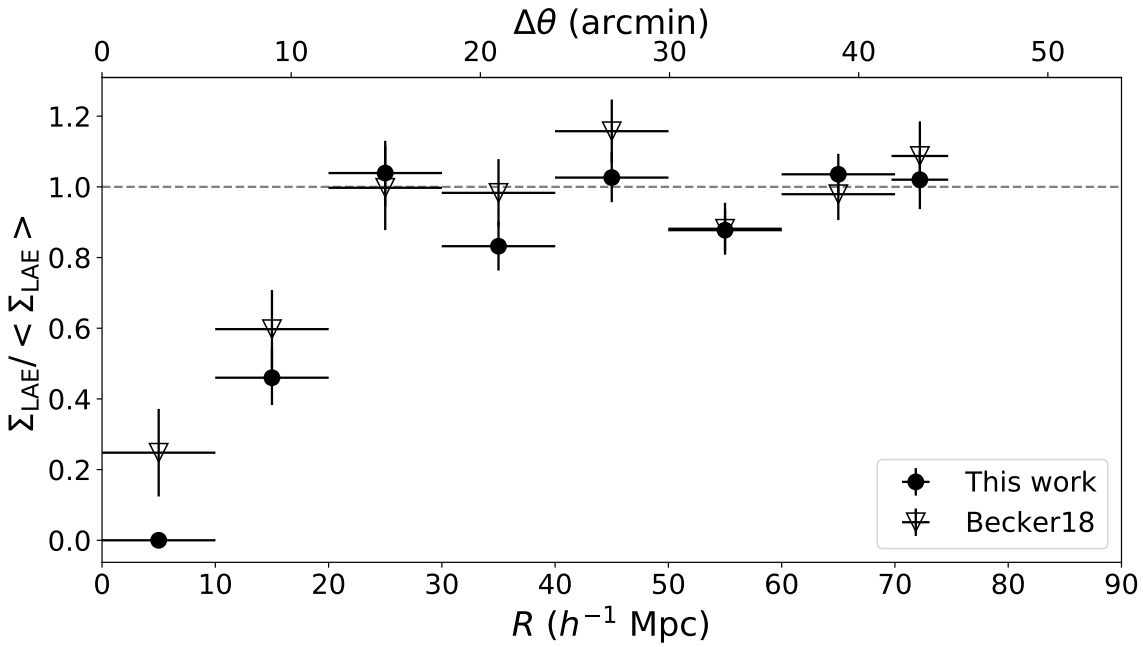

Figure C.2 Surface density of completeness-corrected LAEs in the J0148 field, as selected in this work (filled circles) and by Becker et al. (2018) (open triangles). The surface density is measured in annuli of width 10 h^{-1} Mpc for all except the outermost bin, which has a width of 4.5 h^{-1} Mpc. All surface densities are normalized by the mean value in the respective work, calculated over $15' \leq \theta \leq 40'$. Horizontal error bars show the width of the annuli, and vertical error bars are 68% Poisson intervals.

consistent within the 1σ errors.

To summarize, the results in the J0148 field are largely unchanged between this work and Becker et al. (2018). Approximately 50% of the LAEs selected in this work are also selected by Becker et al. (2018), and, outside of the photometry issues described in Section 2.4.1, the variations are as expected given that each catalog is $\sim$ 50 % complete in its faintest magnitude bin. The two catalogs trace similar large-scale structures (see Figure B.1), most notably both displaying the $\sim 20\ h^{-1}$ Mpc void in the center of the field, along the quasar line of sight.

Appendix D

Completeness Corrections

Figure D.1 shows the completeness measured in both fields as a function of distance from the quasar and $NB816$ magnitude. We determine the completeness by injecting a catalog of artificial LAE candidates across each field and then applying the LAE selection criteria described in Section 2.4. We bin the artificial LAEs by magnitude and distance from the quasar. The completeness is then computed as the fraction of artificial LAEs detected in each bin. The observations are binned in the same way and corrected by the reciprocal of the completeness in each bin.

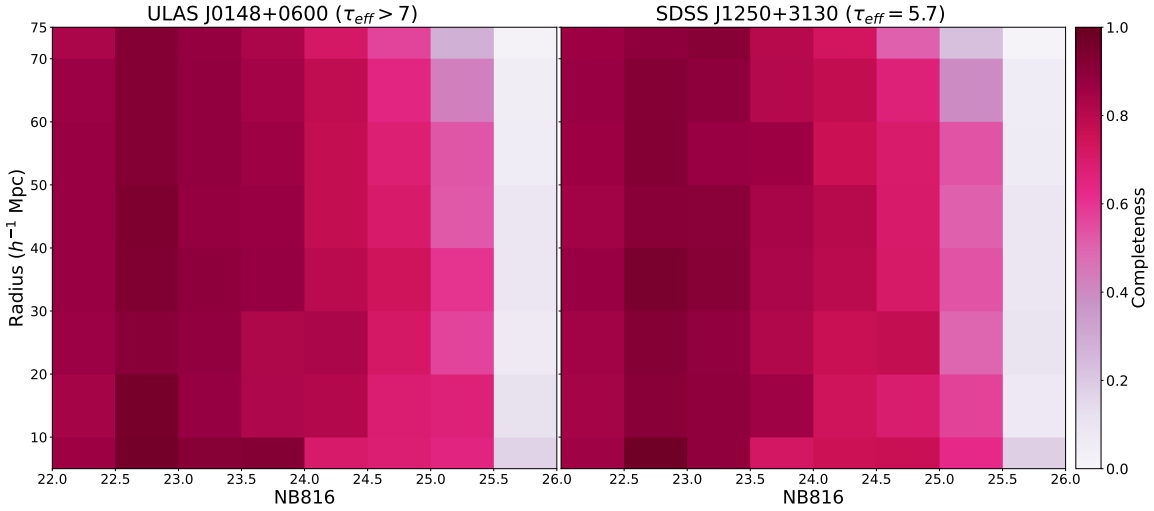

Figure D.1 Completeness measured the J0148 field (left) and J1250 field (right) as a function of $NB816$ magnitude and distance to the quasar. The completeness is based on the detection rate of artificial LAEs injected in each field, and is given by fraction of artificial LAEs detected in each radius and magnitude bin.

Appendix E

Lyα Opacity of Quasar Sightlines

Following Becker et al. (2018); Christenson et al. (2021), we use our imaging data to estimate the Lyα effective opacity for the highly transmissive J1306 and J359 sightlines. Measurements made from the imaging data are comparable to spectroscopic measurements made over 28 h^{-1} Mpc centered on the $NB816$ filter wavelengths, and represents an effective opacity measurement made over the width of the $NB816$ filter. The general procedure is as follows: for each quasar, we begin by measuring the $NB816$ and HSC-$i2$ fluxes from the imaging data following Section 3.4.1. We then convolve each quasar spectrum with the $i2$ transmission curve and scale them so that the transmission-weighted mean flux matches the $i2$ flux measured from the imaging data. We then estimate the unabsorbed continuum flux expected at the Lyα wavelength from PCA fits for the blue-side continuum of each quasar spectrum. Combining these measurements, we calculate the effective opacity as $\tau_{\rm eff} = -\ln(\mathrm{F}_\lambda^{\rm NB816}/\mathrm{F}_\lambda^{\rm cont})$.

For the J1306 sightline, we measure $F_\lambda^{NB816} = (11.2 \pm 0.2) \times 10^{-19}$ erg s^{-1} cm^{-2}

Å^{-1} and $F_\lambda^{i2} = (28.3 \pm 0.2) \times 10^{-19}$ erg s^{-1} cm^{-2} Å^{-1}, and estimate that the unabsorbed continuum is $F_\lambda^{\rm cont} \simeq 1.6 \times 10^{17}$ erg s^{-1} cm^{-2} Å^{-1}. We therefore measure $\tau_{\rm eff} = 2.64 \pm 0.02$. For comparison, we measure $\tau_{\rm eff}^{28} = 2.475 \pm 0.010$ from the X-Shooter spectrum. The uncertainty in $\tau_{\rm eff}$ is based on the propagated uncertainty in F_λ^{NB816} and does not account for uncertainty in the estimated continuum.

For the J359 sightline, we measure $F_\lambda^{NB816} = (9.7 \pm 0.2) \times 10^{-19}$ erg s^{-1} cm^{-2} Å^{-1} and $F_\lambda^{i2} = (7.8 \pm 0.1) \times 10^{-19}$ erg s^{-1} cm^{-2} Å^{-1}, and estimate that the unabsorbed continuum is $F_\lambda^{\rm cont} = 0.8 \times 10^{17}$ erg s^{-1} cm^{-2} Å^{-1}. We therefore measure $\tau_{\rm eff} = 2.26 \pm 0.02$. From the spectra, we measure $\tau_{\rm eff}^{28} = 2.338 \pm 0.01$ over the filter width. For both sightlines, if we assume a 20% uncertainty in the continuum, the uncertainty in our measurements from the imaging becomes ± 0.09.

Appendix F

Lyα Opacity Measurements for Ishimoto et al. (2022) Lines of Sight

In this work we use updated $\tau_{\rm eff}$ values for the three lines of sight included in Ishimoto et al. (2022). Ishimoto et al. (2022) used Keck ESI spectra from the publicly available `igmspec` database (Prochaska, 2017). In contrast, we use versions of these data reduced using a custom pipeline that has been highly optimized for high-redshift QSO spectra (for a description of the pipeline, see López et al. (2016), Becker et al. (2019), and Zhu et al. (2021)). The custom reductions for all three were first presented in Becker et al. (2019), while J1137 and J1602 were also presented in Zhu et al. (2021); Zhu et al. (2022). Our measurements of $\tau_{\rm eff}$ over the two wavelength regions indicated in Figure F.1, corresponding to 28 and 50 h^{-1} Mpc, are given in Table F, along with values from Ishimoto et al. (2022).

Table F.1 Effective opacity measurements for QSO sightlines Ishimoto et al. (2022)

QSO	$\tau_{\rm eff}^{50,a}$	$\tau_{\rm eff}^{50,b}$	$\tau_{\rm eff}^{28,c}$	$\tau_{\rm eff}^{28,d}$
SDSS J1137+3549	2.904 ± 0.042	3.07 ± 0.03	4.344 ± 0.227	5.58 ± 0.62
SDSS J1602+4228	3.063 ± 0.038	3.23 ± 0.05	4.898 ± 0.308	6.05 ± 0.91
SDSS J1630+4012	3.857 ± 0.184	5.47 ± 0.86	4.550 ± 0.477	$>5.06^{e}$

[a] Effective opacity used in this work, measured over a 50 h^{-1} Mpc window centered at 8177 Å

[b] Effective opacity from Ishimoto et al. (2022), measured over a 50 h^{-1} Mpc window centered at 8177 Å

[c] Effective opacity used in this work, measured over a 28 h^{-1} Mpc window centered at 8177 Å

[d] Effective opacity from Ishimoto et al. (2022), measured over a 30 h^{-1} Mpc window centered at 8177 Å

[e] Lower limit

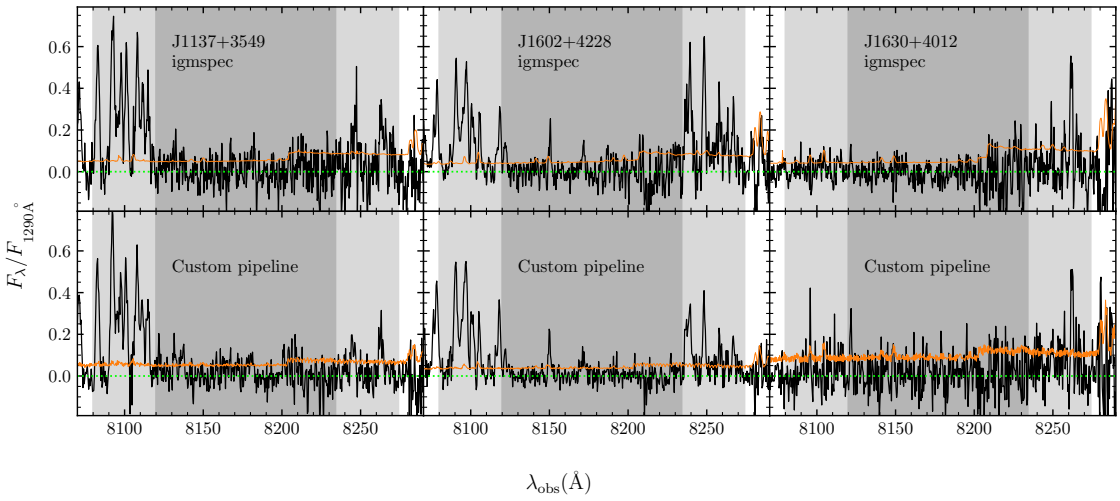

Figure F.1 Partial spectra of quasars J1137+3549, J1602+4228, and J1630+4012 (left to right). The top panels show the spectra for these objects used by Ishimoto et al. (2022), which were selected from the `igmspec` database (Prochaska, 2017). The bottom panels show reductions using a pipeline customized for high-redshift QSOs (e.g., Becker et al. (2019); Zhu et al. (2021); Zhu et al. (2022)). The solid orange lines indicate the flux error and the green dotted line marks a flux of zero. The darker gray shaded rectangles indicate the FWHM of the NB816 filter, which corresponds to 28 h^{-1} Mpc and the lighter shaded regions indicate the 50 h^{-1} Mpc interval over which effective opacity measurements are made. The opacity measurements made from these spectra, both in this work and in Ishimoto et al. (2022), are summarized in Table F.

We find somewhat lower values of $\tau_{\rm eff}^{28}$ for J1137 and J1602, and a lower $\tau_{\rm eff}^{50}$ for J1630. For J1137, our reduction reveals transmission peaks near 8134 and 8180 Å. Taking the transmission from these peaks alone gives $\tau_{\rm eff}^{28} = 4.887 \pm 0.391$, which should be an upper limit on the effective opacity over the entire window as we are assuming that all other pixels have zero transmission. This value is consistent with our measurement in Table F. In the case of J1602, the higher $\tau_{\rm eff}^{28}$ value in Ishimoto et al. (2022) is explained by the presence of a spurious negative feature near 8212 Å, which is not as strong in our reduction. Similarly, the `igmspec` reduction of J1630 appears to show a slight negative bias over 8160–8220 Å, which helps to explain the difference in the $\tau_{\rm eff}^{50}$ values.

Appendix G

Globally Normalized LAE maps

In Section 3.5, we present maps of the LAE candidates in the J0148, J1250, J1306, and J359 fields. Those maps are normalized by the mean surface density in each field, calculated over $15' \leq \Delta\theta \leq 40'$. Normalizing the maps in this way allows us to self-consistently compare the vicinity of the quasar sightline to the rest of the field and determine whether the center of the field is over- or underdense relative to its surroundings. This type of normalization is also useful for making comparisons between fields, as it mitigates differences in depth, seeing, and other observational considerations, and it is the normalization used for all figures in the main body of the text.

However, we can also use the four fields we have observed to date to estimate a global mean surface density and compare the four fields on an absolute scale. This global normalization is limited by the small number of fields observed to date, but is useful for considering how the environments of these four sightlines compare to each other. Figure G.1 shows the LAE maps from Section 3.5. As previously, the fields are centered on the quasar

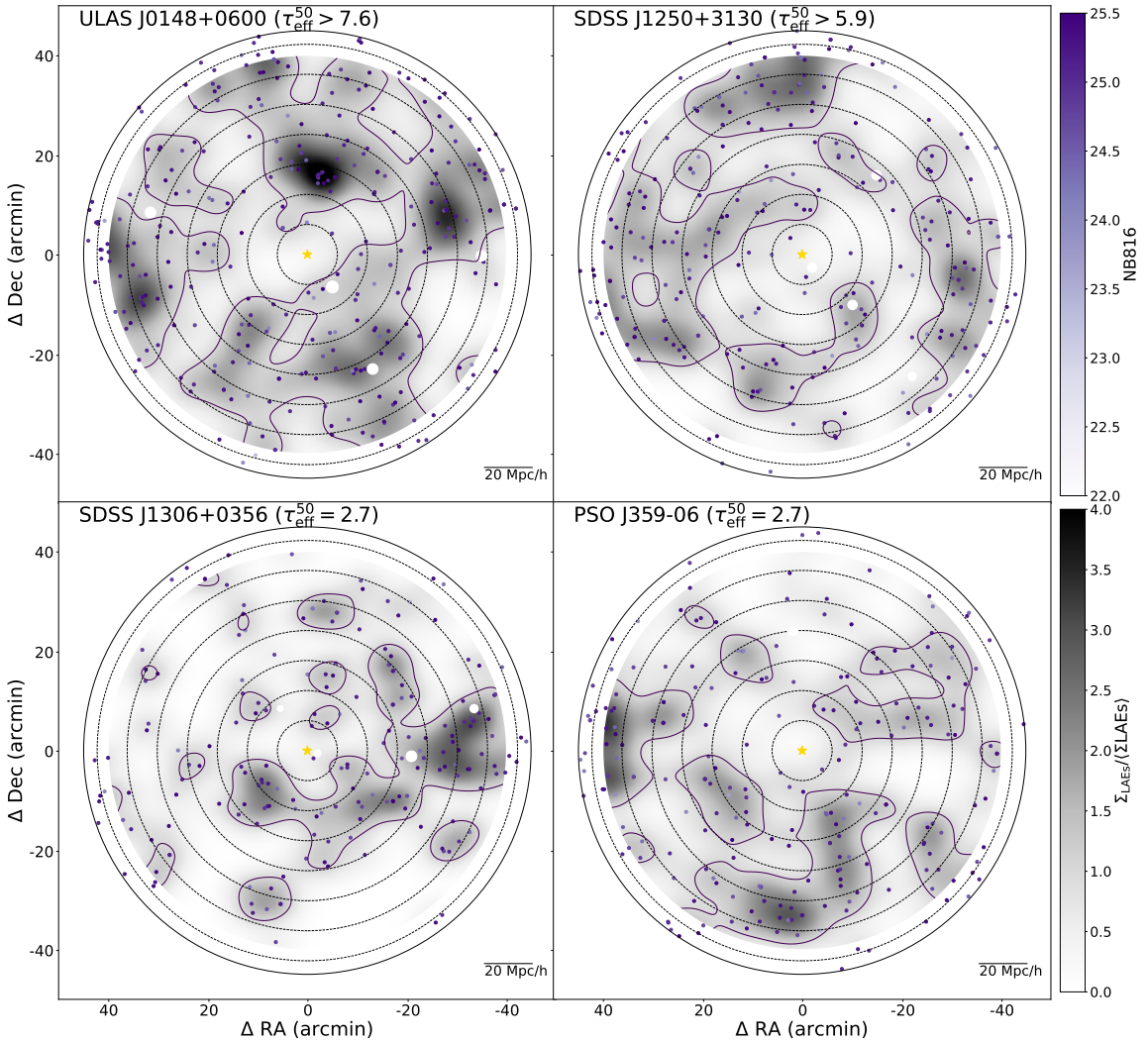

Figure G.1 Distribution of LAE candidates in all four fields: J0148 (top left), J1250 (top right), J1306 (bottom left), and J359 (bottom right). The LAE candidates are assigned a color that indicates their $NB816$ magnitude. The grayscale shading in the background indicates the surface density of LAE candidates, which we calculate by kernel density estimation and normalized by the global mean surface density of all four fields, measured over $15' \leq \Delta\theta \leq 40'$. This surface density is corrected for spatial variations in completeness as described in Section 3.4.3. The field is centered on the quasar position, which is marked with a gold star, and the concentric dotted rings indicate 10 h^{-1} Mpc intervals from the quasar position. The solid ring marks the edge of the field, $45'$ from the quasar position. Portions masked out of the field in white are obscured by foreground stars.

position (yellow star), foreground stars are masked out in white, and the concentric dotted rings indicate 10 h^{-1} Mpc intervals. The purple shading indicates the $NB816$ magnitude of the LAEs, and the grayscale shading indicates the surface density of LAEs (see Section 3.5 for details of the calculation). The surface density is completeness corrected (see Section 3.4.3) and normalized by the global mean surface density, which we measure over the $15' \leq \theta \leq 40'$region of all four fields.

On an absolute scale, all four sightlines are underdense within 10 h^{-1} Mpc of the quasar, consistent with the maps that are normalized individually (see Figure 3.6). However, we note that the J0148 field, while underdense in the vicinity of the quasar sightline, seems to reside in a higher density region overall than the other three fields.

Appendix H

Comparison to Christenson et al. (2021) Selections

Here we compare the selections of LAEs made in the J0148 and J1250 fields in this work to those published in Christenson et al. (2021). In this work, we select 298 LAEs in the J0148 field and 247 in the J1250 field, compared to 641 in the J0148 field and 428 in the J1250 field in Christenson et al. (2021). We show the surface density as a function of $NB816$ magnitude for both selections in Figure H.1, and refer the reader to Figures 3.6, 3.7, and 2.4 for a comparison of the LAE maps and radial surface density distributions. There are two primary differences between these catalogs. First, as discussed in Section 3.4.1, is the use of aperture fluxes as the primary photometric measurement in this work. Aperture fluxes are expected to have lower signal-to-noise compared to PSF fluxes and hence produce fewer detections. Second, we have made a more careful measurement of the seeing in this work, making use of bright stars selected to be bright, but not saturated, and the seeing tends to

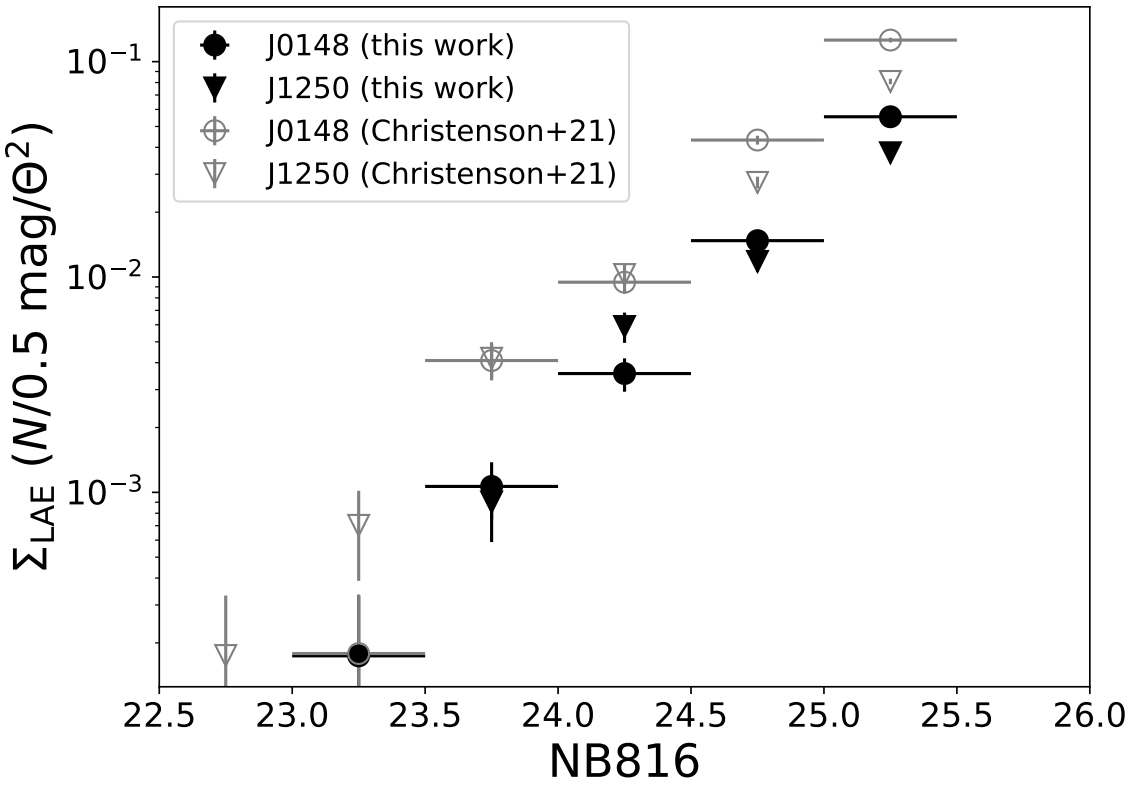

Figure H.1 Completeness-corrected surface density of LAE candidates in the J0148 and J1250 fields in this work (filled markers) and Christenson et al. (2021) (open markers).

be slightly better than previously estimated. The PSF fluxes from Christenson et al. (2021), which are fit to a broader profile than the true extent of the sources, therefore tend to be higher than the aperture fluxes. For these two reasons, the measured surface density is not consistent between the two selections. We note that brightest objects consistently appear in both catalogs but tend to fall in fainter magnitude bins in this work, which is the reason for the poor agreement in the brighter magnitude bins. Despite these differences, the key results of Christenson et al. (2021) are unchanged in this work; both highly opaque sightlines display clear underdensities within 20 h^{-1} Mpc of the quasar sightline, and the large-scale structure of the field is consistent between the two selections.